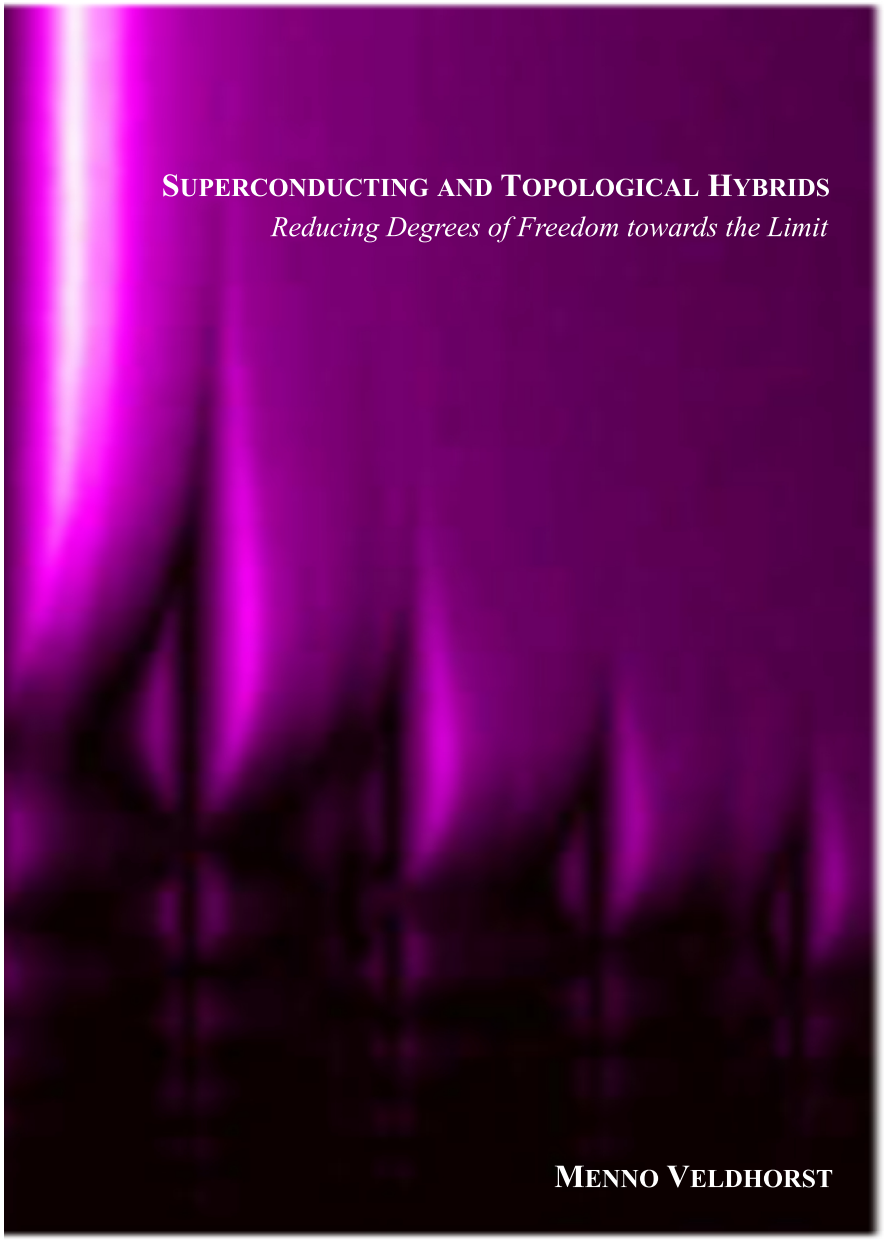
SUPERCONDUCTING AND TOPOLOGICAL HYBRIDS
Reducing Degrees of Freedom towards the Limit
MENNO VELDHORST

Superconducting and Topological Hybrids

Reducing Degrees of Freedom towards the Limit

Menno Veldhorst

Ph.D. committee

Chairman	
prof. dr. G. van der Steenhoven	University of Twente
Secretary	
prof. dr. G. van der Steenhoven	University of Twente
Supervisors	
prof. dr. ir. A. Brinkman	University of Twente
prof. dr. ir. J.W.M. Hilgenkamp	University of Twente
Members	
prof. dr. C.W.J. Beenakker	Leiden University
prof. dr. ir. J.C. Maan	Radboud University Nijmegen
prof. dr. ing. D.H.A. Blank	University of Twente
prof. dr. ir. W.G. van der Wiel	University of Twente
dr. A.A. Golubov	University of Twente

Cover
'Bessel-peacock' dependence of Shapiro steps resulting from microwave irradiation on a superconducting Josephson junction with a topological surface state interlayer.

The research described in this thesis was performed in the Faculty of Science and Technology and the MESA$^+$ Institute for Nanotechnology at the University of Twente, in collaboration with the High Field Magnet Laboratory in Nijmegen.
The work was financially supported by a VIDI grant from the Netherlands Organization for Scientific Research (NWO).
Superconducting and topological hybrids,
Reducing degrees of freedom towards the limit
Ph.D. Thesis, University of Twente
Printed by Printpartners Ipskamp
ISBN 978-90-365-3412-3

SUPERCONDUCTING AND TOPOLOGICAL HYBRIDS,
REDUCING DEGREES OF FREEDOM TOWARDS THE LIMIT

PROEFSCHRIFT

ter verkrijging van
de graad van doctor aan de Universiteit Twente,
op gezag van de rector magnificus,
prof. dr. H. Brinksma
volgens besluit van het College voor Promoties
in het openbaar te verdedigen
op woensdag 19 september 2012 om 14:45 uur

door

Menno Veldhorst

geboren op 3 november 1984
te Harderwijk

Dit proefschrift is goedgekeurd door de promotoren:

prof. dr. ir. A. Brinkman
prof. dr. ir. J.W.M. Hilgenkamp

Contents

Chapter 1 Introduction

Abstract

Systems composed of superconductors coupled to other materials in various geometries have prospects to become building blocks in quantum computation and teleportation. Mesoscopic superconducting devices can potentially be used to prepare a Bell state and can be used to create spatially separated entangled particles. Majorana fermions can appear as emergent particles by the interaction of a superconductor with a topological insulator. This long sought particle is not only fundamentally interesting but might serve as a source for decoherence-immune qubits. This thesis is devoted to the theoretical search for optimal systems and geometries hosting these exotic properties, as well as the experimental realization of these devices.

1.1 Introduction

The study of condensed phases of matter has increased our scientific knowledge enormously and has led to countless applications. Electronic and spintronic devices have become part of our daily lives. These systems are constructed out of materials with different electronic properties. Metals are characterized by good electrical conductivity, insulating materials have no conductivity and semiconductors are somewhere in between. Besides exploiting the electronic charge properties, the electron spin is used in spintronic devices. Magnetic materials such as ferromagnets have a finite magnetization due to preferred orientations of the electron spin, which can be used to store information.

What will happen if we combine these different materials? Interfaces of these conventional materials have already led to the invention of the transistor [1], which forms the basis of almost all electronic devices. Another example is the giant-magnetoresistance (GMR) sensor [2]. This device is fabricated out of magnetic and non-magnetic materials, and is used to read out magnetically stored bits in a computer harddisk.

Materials with more exceptional properties exist as well. Superconductors are materials that have no electrical resistance at all. Topological insulators have both exotic electronic and spintronic properties. The bulk of the material is electrically insulating, while the edge is conducting. The spin of the electrons at the edge

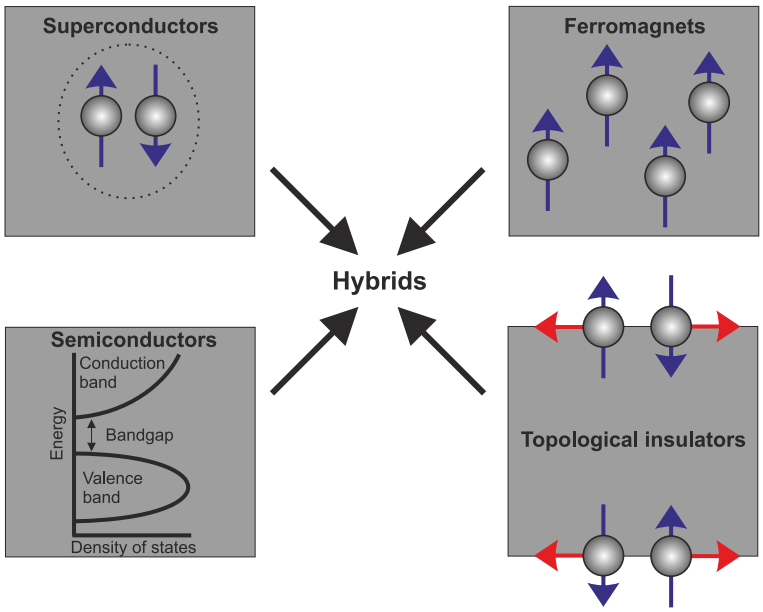

Figure 1.1: Hybrid systems. Condensed matter physics has led to the discovery of many electronic phases. This thesis is devoted to the coupling of different materials, with the emphasis on the interface of superconductors with topological insulators.

is coupled to the direction in which the electrons move. As conventional hybrids have already lead to very important phenomena, what to expect when interfacing exotic materials (Fig. 1.1)?

1.2 Reducing degrees of freedom

Before moving towards interfaces, we will discuss the materials that are used in this thesis. We will consider a free electron and then ask how to reduce its degrees of freedom. This question is of particular relevance in condensed matter physics and will guide us from metals to superconductors to topological insulators.

A classical method to reduce the degrees of freedom is to search which symmetry must be broken, and seek for materials fulfilling this property [3]. Classifying materials according to their broken symmetry is therefore very practical. Noether's theorem states that every continuous symmetry of a system has a corresponding conserved quantity [4]. If we start with a free electron in vacuum, the system has many symmetries. One of the most important is that the starting time does not change an experiment, associated with the conservation of energy. When the electron is put in a crystalline solid, a key concept in solid state physics, translation and rotation invariance are broken. As a consequence of the broken symmetry the crystal becomes rigid. The periodic structure of the lattice determines the

electronic band structure resulting in electronic metallic, semiconducting and insulating systems.

If the electron spin interactions of the material are such that all electrons align their spin in the same direction, spin-rotational symmetry is broken. Ferromagnets have a preferred electron spin orientation, and the total ensemble acquires a finite magnetization. When the electron-electron attraction is positive, mediated for example by phonons, the system can condense to the superconducting state. Gauge symmetry is broken in the superconducting state, the system has macroscopic phase coherence. Although the system is invariant under gauge transformations, the relative phase has important consequences. The superconducting phase difference in a loop is quantized, resulting in fluxoid quantization. The conserved quantity corresponding to the broken symmetry is the charge. Excitations in a superconductor have a charge depending on energy, and become chargeless when the energy equals the superconducting gap. Exciton condensation is another form of gauge symmetry breaking, caused by Coulomb interaction between electrons and holes.

Another concept that can be exploited to classify materials is the topological order of a system [6], which has become important with the discovery of the integer quantum Hall effect [5]. The quantum Hall effect appears when a two dimensional electron gas is subjected to a large magnetic field. The magnetic field leads to discretization of the density of states in Landau levels. The Landau levels are ideally true spikes in the density of states, but can be smeared out by scattering processes. When the Fermi energy is in between two Landau levels, the bulk is insulating as any other insulator. However, skipping orbits lead to a Hall conductivity given by $\sigma_{xy} = Ne^2/h$, with N an integer number counting the amount of filled Landau levels [5]. This value has been measured with extremely high precision serving as the basis for the resistance standard. The quantization of the Hall conductivity is not directly related to a broken symmetry, but rather to topology [7].

Topology is intimately related to the Berry curvature, the building up of a geometrical phase [8]. An example of a geometrical phase is the Aharonov-Bohm phase. The Berry phase is the resulting phase upon rotating an electronic wave function. In a closed loop, the Berry flux must be quantized and is characterized by the Chern number n [9]. The Chern number n is in the class $\mathbb{Z}$, the class of integer numbers. In the absence of a magnetic field, the Berry flux is zero resulting in a Chern number n=0. The system is then topologically trivial. However, in magnetic fields a quantized nonzero Berry phase can be build up, driving the system into a topological state, with a nonzero Chern number. In the quantum Hall system, the total Chern number n equals the Landau level filling factor N, and determines the quantum Hall conductance. These systems have broken time reversal symmetry. Rotating the direction of time switches the direction of the current flowing through the edge of the system. Opposite current directions are at the opposite edge of the system, so that time reversal symmetry is not satisfied. Instead of topologically trivial systems, the properties of the edge states are now determined by the bulk. This is also the reason why quantization in these systems has such high accuracy.

A local perturbation at the edge does not change the bulk, and the total Chern number remains. Consequently, the edge states keep their properties, the system is topologically protected.

Systems that preserve time reversal symmetry, and are topologically distinct from a trivial insulator are found in the class of topological insulators (a review is provided by Hasan and Kane[9]). Strong spin orbit coupling in these materials plays the role of the magnetic field in the quantum Hall state. The spin orbit coupling causes the formation of Landau levels in two-dimensional topological insulators. Since opposite spins feel an opposite 'effective magnetic field' from the spin orbit coupling, opposite spin states travel in opposite directions at the edge. The two-dimensional topological insulator is called the quantum spin Hall insulator. When the perpendicular spin component S_z is conserved, it is possible to define Chern numbers for the spin up and down states. The total Chern number $n = 0$, since the spin dependent Chern numbers $n_\uparrow = -n_\downarrow$ are opposite in sign. Topological insulators fall in a topologically distinct class from the quantum Hall state. This class is determined by a $\mathbb{Z}_2$ invariant, an integer number modulo 2, and is $v = \frac{1}{2}(n_\uparrow - n_\downarrow)\mathrm{mod}2$. When the perpendicular spin is not conserved, $n_\uparrow$ and $n_\downarrow$ lose their meaning, although v retains its identity, and attains a more complex expression[9]. While there is no three-dimensional analog to the quantum Hall state, three-dimensional topological insulators exist[10–12]. There are three $\mathbb{Z}_2$ invariants, v_1, v_2, and v_3, that can be associated with stacking of two-dimensional layers in the three dimensions. There is another $\mathbb{Z}_2$ invariant, v_0, which is associated with the full three-dimensional structure. When $v_0 = 0$ the system is a weak topological insulator, since the topological invariants v_1,v_2, and v_3 do not lead to protection against disorder. When $v_0 = 1$ the system is a strong topological insulator and an odd number of Dirac points are enclosed by the Fermi circle. The system has an insulating bulk and two-dimensional surface states where the electron spin is coupled to the momentum.

1.3 Superconducting and topological hybrids

Now that we have described a variety of materials with unique properties that have led to numerous applications, we come back to the question what happens if we combine these materials. In 1926 Albert Einstein already posed: "A question of particular interest is whether the interface between two superconductors becomes superconducting as well" [13]. The answer to the question was awarded with a Nobel prize for Brian Josephson by his prediction in 1962 of the Josephson effects[14], verified experimentally one year later by Anderson and Rowell[15]. In the previous section we have shown that materials have a reduced degree of freedom. Interfacing combines the properties of the different materials and further reduces the degrees of freedom leading to remarkable phenomena. In this thesis we investigate the coupling between materials, in particular the coupling of superconductivity to topological insulators.

1.3.1 Opportunities in hybrid systems

After 50 years of Josephson superconductivity, coupling superconductors to other materials and in various geometries is still actively studied. This has led to the realization of highly accurate magnetometers (superconducting quantum interferometers)[16], superconducting single-electron transistors[17], rapid single flux quantum digital electronics[18] and superconducting qubits for quantum computers[19,20]. The interaction of superconductivity with magnetism, in for example superconductor-ferromagnet hybrids, has many important fundamental questions (a review is given in[25]).

With the recently discovered topological insulators, the question arises how topologically non-trivial materials couple to superconductors. What is the influence of strong spin orbit coupling on superconductivity? What is the interface transparency? Is it possible to induce superconductivity in the topological surface states? It is predicted that if a superconducting proximity effect can be realized in a topological insulator, this can lead to the observation of a long sought particle: the elusive Majorana fermion[21]. The proposals to prove the existence of this emergent particle rely on complex devices[9,22,23]. However, dc SQUIDS can already signify the presence of Majorana fermions[24]. Is it possible to realize dc SQUIDs with topological insulators and are there tunable experimental parameters that can optimize the Majorana character?

Another question related to the coupling of superconductors with magnetism is: what is the mechanism behind the inverse superconducting spin switch effect? Half metallic ferromagnet-superconductor FSF trilayers have a hysteretic resistance dependence on the magnetic field. What is the origin of this effect? Possible explanations include spin-imbalance, crossed Andreev reflection, and the formation of triplets pairs.

The developments in nanotechnology enabled to study superconducting systems in complex geometries at the nanoscale. It is possible to create spatially separated entangled electrons by contacting closely separated electrodes to a superconductor. This process called crossed Andreev reflection is closely related to Majorana fermions, both may be used to generate qubits but the Majorana character can also be tested via crossed Andreev reflection[26]. How to optimize crossed Andreev reflection in order to make it useful for quantum computation?

Furthermore, we address the question whether it is possible to substitute superconductors with bilayer exciton condensates in superconducting devices to overcome major hurdles present in these systems. Exciton condensation bears many similarities with superconducting condensation. It is therefore interesting to compare superconducting devices with their exciton analogs. Can we realize spatially separated entangled electrons and Majorana fermions using bilayer exciton condensates?

1.3.2 Theoretical background

Superconductivity forms the basis of this thesis. We start describing superconducting condensation, followed by the coupling of superconductors to other, exotic, materials. Interestingly, interface physics allows the fabrication of new phases with unique properties by combining materials which do not have these properties independently.

Superconducting and bilayer exciton condensation

The BCS theory[28], developed by Bardeen, Cooper and Schrieffer, describing superconductivity has proven to be a successful theory. This mean field theory can be obtained by starting with a Hamiltonian consisting of a kinetic term $\hat{H}_0$ and a pairing term $\hat{H}_{int}$

$$\hat{H} = \hat{H}_0 + \hat{H}_{int} = \hat{H}_0 + g \int d^3 \psi_\uparrow^\dagger(\mathbf{r}) \psi_\downarrow^\dagger(\mathbf{r}) \psi_\downarrow(\mathbf{r}) \psi_\uparrow(\mathbf{r}), \quad g < 0. \tag{1.1}$$

After mean field approximation (a more subtle derivation is given by Swidzinsky[29]), the Hamiltonian can be rewritten to

$$\hat{H}_{MF} = \hat{H}_0 - \int d^3 \left[\psi_\uparrow^\dagger(\mathbf{r}) \psi_\downarrow^\dagger(\mathbf{r}) \Delta(\mathbf{r}) + \Delta(\mathbf{r})^* \psi_\downarrow(\mathbf{r}) \psi_\uparrow(\mathbf{r}) \right]. \tag{1.2}$$

Here, the condensation energy $\Delta(\mathbf{r}) = |g| \langle \psi_\downarrow(\mathbf{r}) \psi_\uparrow(\mathbf{r}) \rangle$. The Hamiltonian can be rewritten in an elegant matrix form after introducing new creation and annihilation operators $\alpha_\uparrow = u^* \psi_\uparrow - v^* \psi_\downarrow^\dagger$ and $\alpha_\downarrow^\dagger = u \psi_\downarrow^\dagger + v \psi_\uparrow$. Here, $u^2 = 1 - v^2 = \frac{1}{2}(1 + \frac{\sqrt{E^2 - \Delta^2}}{E})$ are the Bogoliubov coherence factors, obtained from the Bogoliubov-de Gennes matrix

$$\begin{pmatrix} \hat{H}_0(\mathbf{r}) & \Delta(\mathbf{r}) \\ \Delta^*(\mathbf{r}) & -\hat{H}_0(\mathbf{r}) \end{pmatrix} \begin{pmatrix} u \\ v \end{pmatrix} = E \begin{pmatrix} u \\ v \end{pmatrix}. \tag{1.3}$$

The pairing interaction causes a coupling between electrons and holes (empty states), resulting in a quasiparticle charge that is no longer an integer multiple of e, but rather is energy dependent, $Q = e(|u|^2 - |v|^2)$. A quasiparticle right at the Fermi energy is therefore chargeless. The associated dispersion relation together with the quasiparticle charge is shown in Fig. 1.2. The superconducting order parameter Δ can have various forms depending on the pairing term. Low T_C superconductors (e.g. Nb and Al) have s-wave symmetry and are uniform in k-space, while the high T_C superconducting cuprates have a d-wave symmetry with nodes in k-space[30,31]. The recently discovered pnictides are believed to possess multiple orderparameters, $s_\pm$-symmetry[32]. There is strong effort to discover superconductors with p-wave symmetry, which will have triplet rather than singlet Cooper pairs, since the order parameter is antisymmetric and the total wave function has to satisfy fermionic commutation relations. Unfortunately, p-wave superconductors are hard to find in nature. A possible candidate is Sr_2RuO_4[33,34]. Interface physics might come to the rescue, as effective p-wave superconductivity can arise

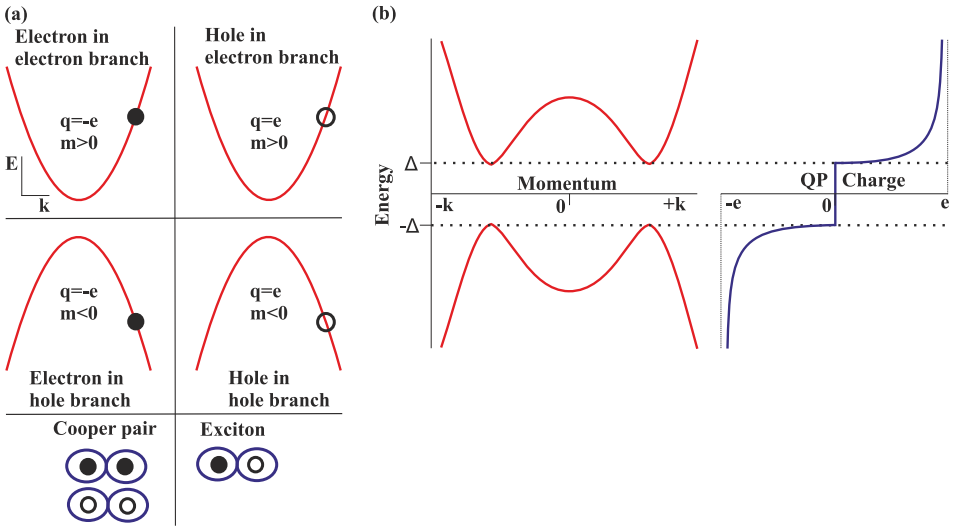

Figure 1.2: Energy dispersion of semiconductors and condensates. (a) Particles and antiparticles in solid state physics. The upper left displays an electron with positive effective mass and negative charge. In the upper right, an empty state in the same band structure is a hole with positive charge. In the lower left an electron with negative mass, an electron in a hole like branch, and in the lower right a missing electron with negative mass, a hole in a hole like branch is shown. Cooper pairs in superconductors are formed by coupling of two particles with the same charge. Oppositely, excitons are formed by two particles with opposite charge. **(b)** Dispersion relation and quasiparticle charge after superconducting or *pn*-bilayer exciton condensation (a Fermi energy $\mu = 3\Delta$ is considered). The quasiparticle charge is zero for excitation energies below Δ; the charge is absorbed by the condensate. A quasiparticle right at the Fermi energy level can become a single zero energy mode by lifting spin degrees of freedom. This zero mode is then a Majorana fermion.

by combining superconductors with other phases, and a possible example is the superconductor - topological insulator interface discussed later on in this section.

Another form of condensation with deep fundamental similarities to superconducting condensation is exciton condensation[35]. Coulomb interaction, M, between two parallel closely spaced layers can induce exciton condensation. When the two layers have opposite effective masses (a *pn*-bilayer), electrons (filled states) and holes (empty states) have an attractive Coulomb interaction. Figure 1.2 clarifies the difference between electrons and holes in electron-like and hole-like branches. Applying mean field approximation to the Coulomb interaction we end up with Bogoliubov-de Gennes equations similar to superconducting condensation, equation 1.3. The Coulomb interaction M plays the role of the superconducting orderparameter Δ, and the Bogoliubov coherence factors describe now the coupling between particles with same charge, but opposite mass.

Local and nonlocal Andreev reflection

An electron coming from a normal metal, impinging on a superconductor, can not directly enter a superconductor when its excitation energy is smaller than the superconducting gap. Instead, there is a region close to the interface where the electron becomes coherent with another electron, and together they join the superconducting condensate. Considering initially only the electron with an energy E above the Fermi energy E_F, afterwards a hole is left behind traveling in the opposite direction with energy $E_F - E$. This is called Andreev reflection[36]. Assuming translational invariance across the interface and perpendicular incidence, the hole travels a coherent path in the opposite direction of the incoming electron over a length $\xi = \frac{\hbar v_F}{2E}$ (in the Andreev approximation for a quadratic dispersion and exact for a linear dispersion), with v_F the Fermi velocity. If the direction of the incoming electron is not perpendicular but makes an angle normal to the interface, the direction is different to normal electron scattering since the hole is retroreflected. The difference in angle between the retroreflected hole and the incident electron is determined by Snell's law and the momentum difference between the electron and the hole. This is usually very small since $\Delta \ll E_F$ in typical structures. If however, $\Delta \geq E_F$ the angle becomes significant and the Andreev reflection can even turn from retro to specular, a limit that might be reached by using e.g. graphene electrodes[37].

The Andreev reflected particle has opposite spin with respect to the incoming particle, since the superconductor consists of singlet Cooper pairs. Therefore, standard Andreev reflection is not possible when the electrode is a halfmetal with 100% spin polarization. Triplet correlations can occur and can be stimulated by inserting additional layers. Including ferromagnetic layers to have a nonuniform magnetization direction results in s-wave triplet pairing which is odd in frequency[38,39]. Even frequency p-wave pairing can arise by the presence of spin-orbit coupling at the interface[40,41].

The entanglement properties of the particles concerning Andreev reflection can be exploited for quantum computation and teleportation. The particles are entangled in spin (due to spin-singlet Cooper pairs), in energy (the total energy is $2E_F$, but the individual particles can have energy different from E_F), and are entangled in momentum (translation invariance across the interface). Exploiting these entangled states can be done by performing correlation measurements on an interface, but it is also possible to spatially separate the particles. When another electrode is attached on a length scale comparable to ξ, the Andreev reflected hole can enter the other electrode. This process is called crossed Andreev reflection or nonlocal Andreev reflection[42]. Finding the optimal system to optimize the crossed Andreev reflection signal with respect to normal Andreev reflection and elastic cotunneling between the electrodes is one of the main challenges in this field. Andreev reflection on bilayer exciton condensates is also possible, and in that case the reflection is always nonlocal, without introducing a second electrode.

Superconductor - topological insulator structures

Coupling a superconductor to a topological insulator is a very interesting combination of superconductivity and strong spin orbit coupling. One of the most interesting applications would be the realization of Majorana fermions[21]. A topological insulator has a linear dispersion with the spin locked to the momentum $\hat{H}_{TI} = \sum_k \Psi_k^\dagger[\hbar v_D(k_x\sigma_x + k_y\sigma_y)\tau_z - \mu]\Psi_k$. Here, the chemical potential is μ, v_D is the Dirac velocity of the linear dispersion and $\boldsymbol{\sigma} = (\sigma_x, \sigma_y)$ are the Pauli spin matrices. Actual topological insulators might have a different spin-momentum locking, due to e.g. Rashba-like terms, but this is only important to consider when the topological insulator is coupled to systems with different spin-momentum locking. The superconducting proximity effect introduces a pairing term $\hat{H}_\Delta = \sum_k[\Delta c_{k,\uparrow}^\dagger c_{-k,\downarrow}^\dagger + h.c.]$. After a clever substitution of basis the orderparameter becomes spinless p-wave[21]. The basis is chosen such that it rotates with momentum: $c_{k,\pm} = \frac{1}{\sqrt{2}}(c_{k\uparrow} \pm e^{-i\phi_k}c_{k\downarrow})$ with $\phi_k = \tan^{-1}(k_x/k_y)$ corresponding to the spin rotation which is locked to the momentum. The large energy differences between the different chiralities (corresponding to the states above and below the Dirac point) result in vanishing cross terms. Consequently, the proximity can be effectively written as $\hat{H}_\Delta = \sum_k[\Delta(k)c_{k,+}^\dagger c_{-k,+}^\dagger + \Delta^*(k)c_{k,-}^\dagger c_{-k,-}^\dagger + h.c.]$, with $\Delta(k) = \Delta e^{i\phi_k}$. The order parameter rotates with momentum and the correlations are triplet. In this case, a quasiparticle at zero energy corresponds to its own antiparticle $\gamma_k = \gamma_{-k}^\dagger$. This particle is the long sought Majorana fermion[21].

The potential of observing this particle and to use it for quantum computation boosted the search for alternative systems that can host the Majorana fermion. Inclusion of ferromagnetism attracted a lot of attention. A ferromagnet can be exploited to open a magnetic gap in the topological surface states to realize and manipulate Majorana fermions[21,22]. When a half-metallic ferromagnet is coupled to a superconductor, singlet Andreev reflection is forbidden, but under the right conditions, triplets can occur that support Majorana fermions[40,41]. An alternative route is using superconductor-nanowire systems. The combination of both spin-orbit coupling and a Zeeman field mimic the topological surface states in the nanowire, and a superconducting proximity effect results then in the appearance of Majorana fermions[43,44]. The first characteristic of a Majorana fermion, a zero energy conductance peak, has recently been observed in these superconductor-nanowire systems[45]. These results indicate the potential of Majorana fermions in condensed matter physics. The next step is to exploit the exotic current phase relationship in superconductor - topological insulator - superconductor structures. For the realization it will be necessary to fabricate Josephson junctions and SQUIDs.

1.4 Outlook

1.4.1 Towards the limit

This thesis is devoted to the study of interfaces between conventional and unconventional materials, with the emphasis on interfaces with superconductors. Superconductors have a reduced degree of freedom due to electron-hole coupling. At the interface with a half-metallic ferromagnet, there is a further reduction by the removal of spin degeneracy. Interfacing with semiconductors reduces the allowed energy levels. Finally, coupling superconductors to topological insulators is reducing degrees of freedom towards the limit. When there is no degeneracy left, a single zero energy mode appears: the Majorana fermion.

1.4.2 Outline of the thesis

In **Chapter 2**, heterostructures of the high-Tc superconductor $YBa_2Cu_3O_{7-\delta}$ (YBCO) and the half-metallic ferromagnet $La_{0.67}Sr_{0.33}MnO_3$ (LSMO) are studied. The structures are fabricated on STO(305) substrates. Tilted epitaxial growth is used to take account of the anisotropy in YBCO and incorporate in-plane components. The devices were fabricated in an FSF arrangement, where a so-called inverse superconducting spin switch occurs. This effect is found to originate from magnetic stray fields of the ferromagnet influencing the superconductor.

Chapter 3 exploits the intrinsic superposition of electrons constituting singlet Cooper pairs in a superconductor. When two metallic electrodes are attached to a superconductor and closely separated, the Cooper pair might be split over the different leads. This novel process is called crossed Andreev reflection and is an interesting candidate for quantum computation. In this chapter a theoretical proposal is put forward to overcome unwanted processes usually present in these systems. The idea is to reduce degrees of freedom by attaching instead of metallic, two semiconducting leads with bandgaps tuned to the right locations. It is shown theoretically that currents with 100% pure nonlocal spin entangled particles are possible in these devices.

Motivated by the equivalence between exciton and superconductor condensates we study in **Chapter 4** interfaces with bilayer exciton condensates with the interest of superconducting junctions in mind. Andreev reflection on bilayer exciton condensates is always nonlocal and can therefore be used for the creation of spatially separated entangled particles. Vanishing direct tunneling and topological protections ensures high Andreev reflection probability. The spin momentum locking ensures singlet formation and opens alternatives to read out the entangled states. Zero modes appear with fractional charge in topological exciton condensate - topological insulator - topological exciton condensate junctions. These zero modes can be turned into unpaired Majorana states by either lifting layer degeneracy by a magnetic field, or by coupling the top and bottom layer of the bilayer exciton condensate with a topological insulator. These emergent Majorana

fermions have different character than the Majorana fermions in superconducting systems.

In **Chapter 5** we experimentally study superconductor-topological insulator junctions. Exotic phenomena are expected to occur in the interaction with singlet Cooper pairs and the unusual spin texture of topological insulators. Perhaps the most interesting phenomenon is that these structures might host Majorana fermions. A first step in the realization of this new particle is the unequivocal demonstration of a supercurrent in a topologically non-trivial phase. Superconductor (Nb) - topological insulator (Bi_2Te_3) - superconductor junctions are fabricated. Clear Josephson effects are observed. From high magnetic field measurements it is concluded that the supercurrent is carried by the topologically non-trivial state of the top surface, despite a large bulk shunt present in the normal state. Interestingly, these Josephson junctions are in the ballistic limit.

One of the peculiar effects of the Majorana fermion is that it can cause a $\sin(\phi/2)$ current phase relationship in Josephson junctions. In **Chapter 6** we numerically study these topologically non-trivial dc SQUIDs. By virtue of the Majorana fermion, single electron appears causing doubled fluxoid quantization in superconducting rings. It is found that although quantum phase slips can relax the system towards standard quantization, the $\sin(\phi/2)$ component still influences the critical current modulation. It is also observed that the SQUID parameter β_L can be used to tune the amplitude of the different frequencies.

In the search for Majorana devices and doubled fluxoid quantization, dc SQUIDs composed of superconductor - topological insulator - superconductor junctions are fabricated. **Chapter 7** describes the fabrication and the successful critical current modulation of these devices. Standard fluxoid quantization is observed in equilibrium measurements.

Bibliography

[1] J. Bardeen and W.H. Brattain, Phys. Rev. **74**, 230 (1948).

[2] P. Grünberg, R. Schreiber, Y. Pang, M.B. Brodsky, and H. Sowers, Phys. Rev. Lett. **57**, 2442 (1986).

[3] Y. Nambu, Nobel lecture (2008).

[4] E. Noether, Math-phys. Klasse **1918**, 235 (1918) [Transport Theory Statist. Phys. **1**, 183 (1971)].

[5] K. von Klitzing, G. Dorda, and M. Pepper, Phys. Rev. Lett. **45**, 494 (1980).

[6] D.J. Thouless, M. Kohmoto, M.P. Nightingale, and M. den Nijs, Phys. Rev. Lett. **49**, 405 (1982).

[7] S. Ryu, A. Schnyder, A. Furusaki, and A. Ludwig, New J. Phys. **12**, 065010 (2010).

[8] M.V. Berry, Proc. R. Soc. Lond. A **392**, 45 (1984).

[9] M.Z. Hasan and C.L. Kane, Rev. Mod. Phys. **82**, 3045 (2010).

[10] L. Fu, C.L. Kane, and E.J. Mele, Phys. Rev. Lett. **98**, 106803 (2007).

[11] J.E. Moore and L. Balents, Phys. Rev. B **75**, 121306(R) 2007.

[12] R. Roy, Phys. Rev. B **79**, 195322 (2009)

[13] A. Einstein, Kuratoriumssitzung der Physikalisch-Technischen Reichsanstalt (1926).

[14] B.D. Josephson, Phys. Lett. **1**, 251 (1962).

[15] P.W. Anderson and J.M. Rowell, Phys. Rev. Lett. **10**, 230-232 (1963).

[16] R.C. Jaklevic, J. Lambe, A.H. Silver, and J.E. Mercereau, Phys. Rev. Lett. **12**, 159 (1964).

[17] T.A. Fulton, P.L. Gammel, D.J. Bishop, L.N. Dunkleberger, and G.J. Dolan, Phys. Rev. Lett. **63**, 1307 (1989).

[18] K.K. Likharev, O.A. Mukhanov, and V.K. Semenov, SQUID '85, 1103 (1985).

[19] Y. Nakamura, Y.A. Pashkin, and J.S. Tsai, Nature **398**, 786 (1999).

[20] J.E. Mooij, T.P. Orlando, L. Levitov, L. Tian, C.H. van der Wal, and S. Lloyd, Science **285**, 1036 (1999).

[21] L. Fu and C.L. Kane, Phys. Rev. Lett. **100**, 096407 (2008).

[22] A.R. Akhmerov, J. Nilsson, and C.W.J. Beenakker, Phys. Rev. Lett. **102**, 216404 (2009).

[23] C.W.J. Beenakker, ArXiv:1112.1950v2 (2012).

[24] L. Fu and C.L. Kane, Phys. Rev. B **79**, 161408(R) (2009).

[25] A.I. Buzdin, Rev. Mod. Phys. **77**, 935 (2005).

[26] J. Nilsson, A.R. Akhmerov, and C.W.J. Beenakker, Phys. Rev. Lett. **101**, 120403 (2008).

[27] J.G. Bednorz and K.A. Müller, Zeitschrift für Physik B **64**, 189 (1986).

[28] J. Bardeen, L.N. Cooper, and J.R. Schrieffer, Phys. Rev. **108**, 1175 (1957).

[29] A.V. Swidzinsky, Spatially inhomogenous problems in the theory of superconductivity, Nauka: Moscow (1982).

[30] C.C. Tsuei and J.R. Kirtley, Rev. Mod. Phys. **72**, 969 (2000).

[31] J.R. Kirtley, C.C. Tsuei, Ariando, C.J.M. Verwijs, S. Harkema, and H. Hilgenkamp, Nature Phys. **2**, 190 (2006).

[32] I.I. Mazin, Nature **464**, 183 (2010).

[33] K. Ishida, H. Mukuda, Y. Kitaoka, K. Asayama, Z.Q. Mao, Y. Mori, and Y. Maeno, Nature **396**, 658 (1998).

[34] F. Kidwingira, J.D. Strand, D.J. van Harlingen, and Y. Maeno, Science **314**, 1271 (2006).

[35] Z.F. Ezawa, A. Iwazaki, Phys. Rev. B **47**, 12 (1993).

[36] A.F. Andreev, Zh. Eksp. Teor. Fiz. **46**, 1823 (1964) [Sov. Phys. JETP **19**, 1228 (1964)].

[37] C.W.J. Beenakker, Phys. Rev. Lett. **97**, 067007 (2006).

[38] M. Eschrig, J. Kopu, J.C. Cuevas, and G. Schn, Phys. Rev. Lett. **90**, 137003 (2003).

[39] M.S. Anwar, M. Veldhorst, A. Brinkman, and J. Aarts, Appl. Phys. Lett. **100**, 052602 (2012).

[40] M. Duckheim and P.W. Brouwer, Phys. Rev. B **83**, 054513 (2011).

[41] S.B. Chung, H.J. Zhang, X.L. Qi, S.C. Zhang, Phys. Rev. B **84**, 060510 (2011).

[42] J.M. Byers and M.E. Flatté, Phys. Rev. Lett. **74**, 306 (1995).

[43] J.D. Sau, R.M. Lutchyn, S. Tewari, and S. Das Sarma, Phys. Rev. Lett. **104**, 040502 (2010).

[44] J. Alicea, Phys. Rev. B **81**, 125318 (2010).

[45] V. Mourik, K. Zuo, S.M. Frolov, S.R. Plissard, E.P.A.M. Bakkers, and L.P. Kouwenhoven, Science **336**, 1003 (2012).

Chapter 2 Magnetization-induced resistance-switching effects in $La_{0.67}Sr_{0.33}MnO_3/YBa_2Cu_3O_{7-\delta}$ bi- and trilayers

Abstract

We have studied the influence of the magnetization on the superconducting transition temperature (T_c) in bi- and trilayers consisting of the half-metallic ferromagnet $La_{0.67}Sr_{0.33}MnO_3$ and the high-temperature superconductor $YBa_2Cu_3O_{7-\delta}$ (YBCO). We have made use of tilted epitaxial growth in order to achieve contacts between the two materials that are partly in the crystallographic *ab* plane of the YBCO. As a result of uniaxial magnetic anisotropy in the tilted structures, we observe sharp magnetization-switching behavior. At temperatures close to T_c, the magnetization-switching induces resistance jumps in trilayers, resulting in a magnetization dependence of T_c. In bilayers, this switching effect can be observed as well, provided that the interface to the ferromagnetic layer is considerably rough. Our results indicate that the switching behavior arises from magnetic stray fields from the ferromagnetic layers that penetrate into the superconductor. A simple model describes the observed behavior well. We find no evidence that the switching behavior is caused by a so-called superconducting spin switch, nor by accumulation of spin-polarized electrons. Observation of magnetic coupling of the ferromagnetic layers, through the superconductor, supports the idea of field-induced resistance switching.

2.1 Introduction

The interplay between superconductivity and ferromagnetism is a rapidly developing field in condensed-matter physics. In hybrid heterostructures, where the two different orders meet at the interface, interesting physics arises. One of the promising structures is the so-called superconducting spin switch,[1,2] which consists of two ferromagnetic (F) metallic layers, sandwiching a superconductor (S). An early theoretical proposal for a spin switch, involving ferromagnetic insulators, was made by De Gennes.[3] Here, the average exchange field induced in the superconductor depends on the relative orientation of the ferromagnetic layers. As a result, the superconducting transition temperature T_c depends on this orientation.

Recently, such geometries were investigated for the case of metallic weak ferromagnets and it was predicted that, under the right circumstances, superconductivity can be switched on and off by applying a small external field.[1,2] This switching was suggested to result from interference between the superconducting wave functions transmitted through the S/F interface and reflected at the F surface. An alternative scenario for spin switching is in terms of crossed Andreev reflection:[4] when the ferromagnetic layers are magnetized in the antiparallel (AP) direction, Cooper pair formation due to crossed Andreev reflection is enhanced, compared to the parallel (P) configuration. This effect is the largest for strongly spin-polarized magnets, when crossed Andreev reflection occurs *only* in the case of antiparallel magnetization.

Although full switching of superconductivity has never been observed, a resistance drop has been found in F/S/F systems with weak ferromagnets when switching the magnetization from the P to the AP state.[5,6] In systems with strong ferromagnets, the opposite effect was observed by Rusanov *et al.*,[7] which was attributed to an increased number of quasiparticles in the superconductor as a result of the enhanced reflection of the spin-polarized quasiparticles. However, Moraru *et al.*[8,9] found the standard spin-switch effect in a comparable system. The contradictory results might be related to the employment of the exchange bias mechanisms in some of these works.[10] Recently, T_c shifts in F/I/S/I/F (in which "I" denotes an insulator) multilayer systems were observed that could not be fully explained by the spin-switch effect, but were partly attributed to spin imbalance in the superconductor, induced by the ferromagnet.[11] However, it was pointed out by Steiner and Ziemann[12] that stray fields due to specific magnetic domain configurations can lead to changes in T_c. Stamopoulos *et al.*[13,14] reported stray-field-based magnetoresistance in $Ni_{80}Fe_{20}/Nb/Ni_{80}Fe_{20}$ trilayers, which emerges from a magnetostatic coupling of the ferromagnetic layers. The importance of stray fields was further established by Carapella *et al.*,[15] who found that a glassy vortex phase induced by magnetic stray fields explains the switching behavior in their Co/Nb/Co trilayers. Thus, magnetic stray field effects are a potential problem for the interpretation of data obtained on structures with ferromagnets in close proximity to superconductors.

Studies on F/S hybrid systems have not been limited to conventional superconductors and ferromagnets. Combinations of the oxide materials $La_{0.67}Sr_{0.33}MnO_3$ (LSMO) and $La_{1-x}Ca_xMnO_3$ (LCMO) with $YBa_2Cu_3O_{7-\delta}$ (YBCO) have been used because of the high spin-polarization of LSMO (Ref. 16) and the good lattice match, allowing the growth of epitaxial structures. In these systems, large magnetoresistance and an inverse spin-switch effect were found and attributed to the transmission of spin-polarized carriers into the superconductor.[17,18] Vortex effects were ruled out as a cause for the observed phenomena, since no effects were seen in bilayers. Anisotropic magnetoresistance effects were excluded on the basis of the absence of a dependence of the magnetoresistance peak on the relative orientation of current and magnetic field.[19] However, the role of spin injection in LCMO/YBCO structures is not entirely clear. Gim *et al.*[20] found no conclu-

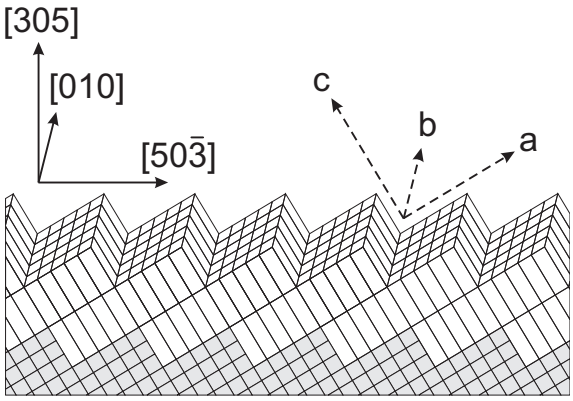

Figure 2.1: Schematic picture of YBCO grown on STO (305). Indicated are the in-plane and out-of-plane crystallographic orientations and the YBCO a, b, and c directions. The c axis makes an angle of 31° with respect to the sample surface.

sive evidence of suppression of superconductivity from their quasiparticle injection experiments using LCMO/LSMO and YBCO. A similar conclusion was reached recently by Deng *et al.*[21] from mutual inductance measurements on YBCO/LCMO bilayers, which were optimized for the experiment by growing YBCO with the c axis in the plane of the film. These kind of experiments are performed under equilibrium conditions in the bilayers and might be more comparable to the current-in-plane (CIP) measurements in Ref. 17 than quasiparticle injection experiments. In the mutual induction experiments, suppression of superconductivity was found near the coercive field of the LCMO layer, which was attributed to magnetic field effects.

It has been known from other systems as well that the effects of field can be important. For example, they can give rise to domain-wall-guided superconductivity[22] and flux-flow-induced giant-magnetoresistance (GMR) effects.[23] The volume magnetization of LSMO, $\mu_0 M$, can reach 0.8 T and it therefore is reasonable to expect a strong influence of stray fields. In a recent publication, Mandal *et al.*[24] pointed out a distinct contribution of the dipolar field to the magnetoresistance in F/S/F trilayers with $Y_{0.6}Pr_{0.4}Ba_2Cu_3O_7$ used for the superconductor. However the relative contribution to the magnetoresistance of the depairing due to accumulation of spin-polarized electrons remains unclear. Furthermore, the higher resistance seen in the state of AP magnetization is not understood.

So far, c-axis-oriented YBCO/LSMO superlattices, such as those grown on $SrTiO_3$ (STO) (001) substrates, have been widely exploited. A disadvantage of these structures is the weak coupling between the superconductor and the ferromagnet, due to the strongly anisotropic nature of superconductivity in YBCO. In order to achieve coupling that is (partly) in the ab plane, we will exploit coherently tilted epitaxial growth[25] of YBCO on STO (305) substrates. On these substrates,

YBCO grows with the c axis making a 31° angle with respect to the sample surface, as indicated in Fig. 2.1. A second advantage of using the (305)-oriented structures is that remarkably sharp magnetization-switching behavior can be realized, caused by the induced uniaxial magnetic anisotropy, with the easy axis along the [010] direction. This enables us to prepare a well-defined state of P or AP magnetization in trilayers.

In this Chapter, we show that the trilayer resistance shows a sharp drop when the magnetization is switched from the AP to the P state within the superconducting transition. However, we find that the observed switching behavior is incompatible with the superconducting spin-switch model and models based on spin imbalance. We find a natural explanation in terms of stray fields from the LSMO layers that penetrate the superconductor. Our measurements show clearly that the switching behavior can be understood completely from changes in the effective field when one of the ferromagnetic layers switches. We will show that we can even obtain switching behavior in bilayers, as expected within our model, by exploiting the controllable surface roughness of the ferromagnetic layers.

2.2 Experimental details

2.2.1 Film growth and characterization

All thin films were grown on STO substrates. The STO (001) substrates were chemically treated[26] and annealed for at least 2 h at 950 °C in an oxygen flow to produce atomically flat TiO_2-terminated surfaces. For the (305)-oriented substrates a single termination does not exist, but the surfaces were atomically flat and substrate steps were observed, due to a small miscut with respect to the (305) plane. The thin-film heterostructures were grown with pulsed laser deposition using a laser fluence of 1.5 J cm^{-2} for both YBCO and LSMO. Film thicknesses were in the ranges of 50–150 nm for LSMO and 20–100 nm for YBCO. The deposition temperature and oxygen pressure were, respectively, 780 °C and 0.25 mbar for YBCO and 800 °C and 0.16 mbar for LSMO. For LSMO, the quality of epitaxial growth depends on the flux rate of the ablated material. We used the substrate-target distance to optimize the epitaxy of the LSMO layers. After deposition, the thin films were annealed for 10 min at 600 °C in oxygen close to atmospheric pressure and subsequently cooled down at a rate of 4 °C min^{-1}.

X-ray-diffraction (XRD) measurements confirmed the epitaxial growth of the multilayers on both types of substrates (Fig. 2.2). YBCO showed a slightly distorted unit cell on STO (305): the angle between the crystallographic a and c axes was 90.7(4)°, resulting in a monoclinic unit cell. However, a single film on STO (305) showed an almost nominal value for T_c of 90 K.

LSMO grows smoothly on STO (305) substrates. Atomic force microscope (AFM) measurements on a 150 nm film showed a root-mean-square (rms) roughness of 2 nm and a peak-to-peak (pp) roughness of 5 nm. YBCO was much rougher

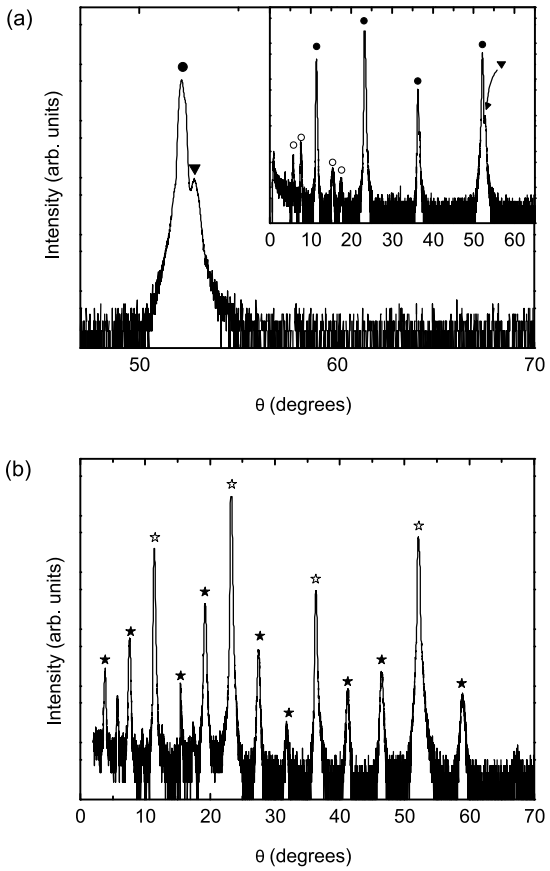

Figure 2.2: θ-2θ scan of LSMO and YBCO/LSMO grown on STO (305). **(a)** θ-2θ scan of LSMO grown on STO (305). Triangles denote LSMO peaks, which largely overlap with the STO peaks, indicated by closed circles. Peaks indicated by open circles are due to higher harmonics in the beam. **(b)** θ-2θ scan for a YBCO/LSMO bilayer. Filled stars correspond to YBCO peaks; open stars indicate overlapping STO, LSMO, and YBCO peaks.

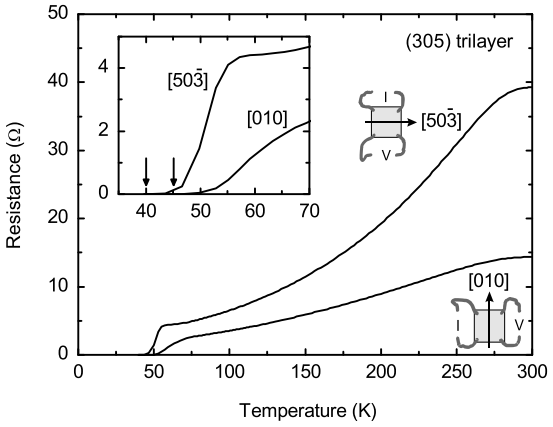

Figure 2.3: Temperature dependence of the resistance. Temperature-dependence of the resistance for a (305)-oriented F/S/F trilayer for two different directions of the applied current, as indicated. The layer thicknesses for the bottom F, S, and top F layer are 50, 30, and 150 nm, respectively. The inset shows the behavior around T_c; vertical arrows indicate T_c.

with a pp roughness of 30 nm (5 nm rms) for a 100 nm film. The AFM images are shown as insets in Fig. 2.5. We attribute this large roughness to differences in growth rate between the YBCO *ab* and *c* directions. Second, nucleation effects are expected, since the YBCO lattice vector in the crystallographic *c*-direction is three times as large as that of STO. As a result, an integer number of YBCO unit cells will not always fit between two nucleation sites. We therefore expect a large number of antiphase boundaries in these films. When LSMO was grown on top of YBCO, the average roughness did not further increase. For bilayers, this implies that we can choose to grow a smooth LSMO/YBCO interface, by putting the LSMO underneath the YBCO layer, or a rough interface, by putting LSMO on top of YBCO, making roughness a controllable parameter in unraveling the spin-switch mechanism.

2.2.2 Transport and magnetization properties

Temperature-dependent resistance (RT) measurements on trilayers clearly showed a parallel contribution of both LSMO and YBCO. In Fig. 2.3, RT-curves are shown that are measured for two different directions of the current in a four-point configuration with electrical connections to the corners of the trilayer. This configuration was used in all measurements. In the [010] direction the resistance has a YBCO-like linear temperature dependence. The resistance measured in the [50$\bar{3}$] direction is larger and has the bell shape that is typical for LSMO, indicating

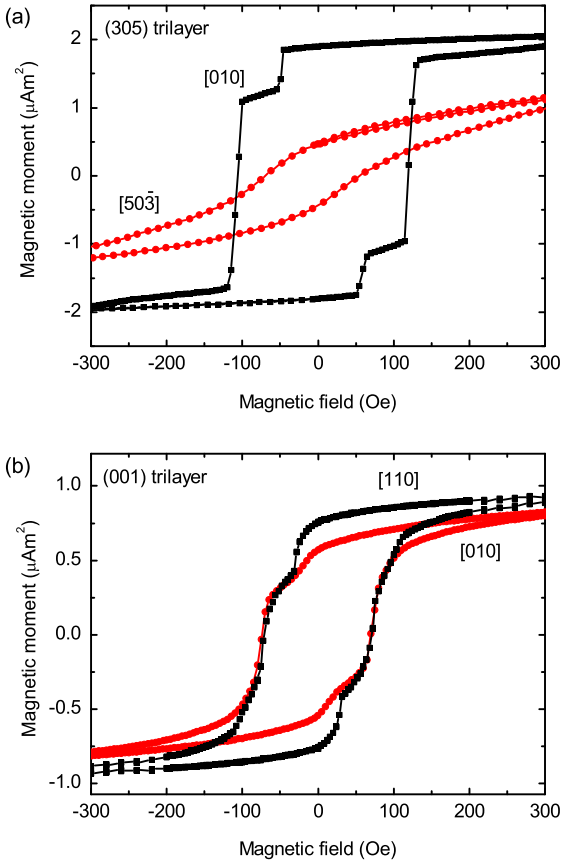

Figure 2.4: Trilayer magnetization hysteresis. Magnetization measurements on **(a)** (305)-oriented and **(b)** (001)-oriented F/S/F trilayers. The bottom and top F layers are 50 and 150 nm, respectively; the S layer is 30 nm. Measurements are taken at temperatures slightly above T_c of the superconductor. The magnetic field directions are indicated in the figure. The (305)-oriented trilayers show uniaxial magnetic anisotropy. The magnetization loop for the (001)-oriented trilayers shows somewhat sharper features when measured along the [110] direction than along the [010] direction, in accordance with literature (Ref. 27).

that the YBCO resistance is higher in this direction. We attribute this to the c-axis transport component, which is present for this direction. In addition, a contribution of the antiphase boundaries can be expected predominantly in this direction. The thinnest YBCO films in bi- and trilayers exhibited a reduced T_c, probably related to strain effects. In some structures we found two values for T_c depending on the direction of measurement. Thus, a superconducting path between the current electrodes in the [010] direction could be formed at a higher temperature than in the $[50\bar{3}]$ direction. By using a zero-resistance criterion for T_c, we found 45 K (40 K in the $[50\bar{3}]$ direction), for a thickness of 30 nm, which decreased to 20 K (both directions) for 20 nm films.

Magnetization measurements were performed using a vibrating-sample magnetometer (VSM) mounted in the same system in which the transport measurements were taken. In one occasion, a superconducting quantum interference device (SQUID) magnetometer was used. Small field offsets (less than 20 Oe) observed in the VSM were absent in the SQUID magnetometer. Our thin films showed slightly reduced Curie temperatures in the range of 320–350 K. Hysteresis loops with the field oriented along the [010] direction and the $[50\bar{3}]$ direction are presented in Fig. 2.4(a) for an F/S/F trilayer with bottom and top layers of 50 and 150 nm, respectively, and a YBCO thickness of 30 nm. The contributions of the two individual LSMO layers are clearly visible and sharp magnetization switching is observed when the field is applied in the [010] easy direction. Since the magnetic anisotropy of LSMO is sensitive to strain and uniaxial strain was found to induce uniaxial magnetic anisotropy,[28] we expect uniaxial magnetic anisotropy for LSMO on STO (305) as well. Indeed, the $[50\bar{3}]$ direction is clearly not an easy axis. We tried to fit both curves using the Stoner-Wohlfarth model[29] for a single-domain ferromagnet, but could not find a satisfactory fit using a single set of parameters. The (001)-oriented trilayers are expected to show biaxial magnetic anisotropy at low temperatures.[27] Although the difference is small, the magnetization loop measured along the [110] easy direction (measured in the SQUID magnetometer) as shown in Fig. 2.4(b) shows sharper features and larger saturation magnetization than the one measured along the [010] hard direction. Although two coercive fields are observed for both directions, the switching is less sharp than for the (305)-oriented trilayer and the AP state is poorly defined. We conclude that this is due to the biaxial magnetic anisotropy.

2.3 Results and discussion

2.3.1 Resistance switching in F/S bilayers

We have grown bilayers on STO (305) both with the LSMO underneath YBCO (F/S) and with the LSMO on top (S/F). In both structures, the YBCO thickness is 30 nm and the LSMO thickness is 150 nm. Both structures show a reduced T_c of 60 K. The resistance as a function of magnetic field is measured in the su-

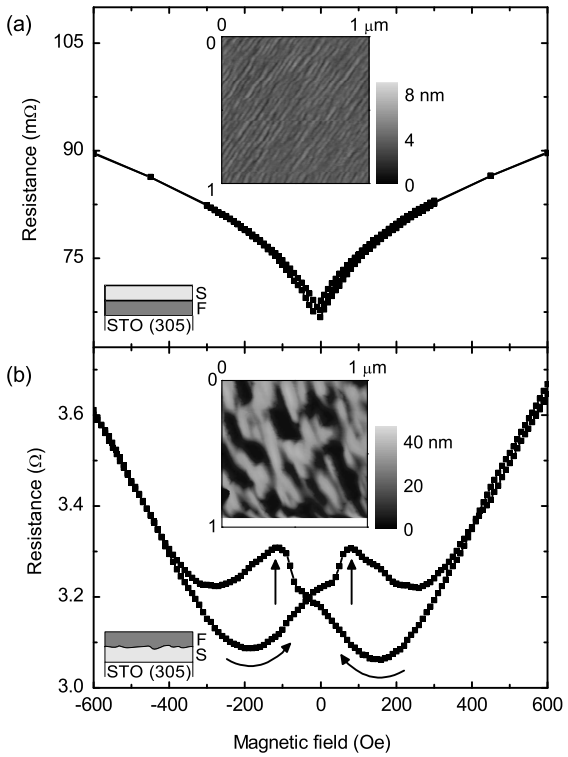

Figure 2.5: Bilayer resistance hysteresis. Resistance measurements at 61 K in the superconducting transition as a function of magnetic field on **(a)** an STO (305)/LSMO/YBCO bilayer (150/30 nm) and **(b)** an STO (305)/YBCO/LSMO bilayer (30/150 nm) measured in a current-in-plane configuration. The magnetic field is applied along the [010] easy axis. The sweep direction is indicated by arrows; the vertical arrows indicate the coercive field of the ferromagnetic layer. The inset in **(a)** shows an AFM image obtained on a 150 nm single LSMO film, which is much smoother than a 100 nm single YBCO film, as shown in (b).

perconducting transition (at 61 K) using a CIP technique. Magnetic fields are applied along the easy axis. In the STO (305)/F/S structure, which has a smooth LSMO layer, the observed hysteresis is the largest for temperatures above T_c. Even here, it is smaller than 0.2 % and is a direct result of the butterfly-shaped magnetoresistance of the LSMO layer. The magnetoresistance in the superconducting transition at 61 K is shown in Fig. 2.5(a). When the order of the layers is reversed, which yields a rougher interface, a large hysteresis in the superconducting transition appears, which is too large to arise from the LSMO magnetoresistance. A typical result is depicted in Fig. 2.5(b). Starting from large negative fields, the resistance shows a parabolic dependence on the field with a minimum around -200 Oe. Then, reaching the positive coercive field of 80 Oe, indicated by a vertical arrow, a peak structure can be observed in the magnetoresistance. Above 200 Oe, the resistance starts following the parabolic dependence again, however now displaced over the horizontal axis by a value of approximately 350 Oe. Since there is only one ferromagnetic layer we cannot analyze our results in terms of the relative orientation of ferromagnetic layers ruling out the spin-switch effect as a cause of the observed shift. Similarly, explanations using spin imbalance or increased quasiparticle densities fail for bilayers, since in these models there is no dependence on the direction of the spins. In fact, the observation of hysteresis effects in bilayers strongly points at an influence of the magnetization direction of the layer and its relative direction to the applied magnetic field. One can think of the total magnetic field, given by the contributions of the applied field and the stray fields of the ferromagnetic layer, as the main parameter determining the resistance of the bilayer. The peak structure around the coercive field is then most likely caused by stray fields at domain walls, due to the reorientation of magnetic domains. The larger S/F surface roughness of the STO (305)/S/F compared to the STO (305)/F/S bilayer might be expected to increase stray field effects.[30] The larger hysteresis observed in the STO (305)/S/F structures confirms this picture, in agreement with Ref. 13.

2.3.2 Resistance switching in F/S/F trilayers

In addition to bilayers, we observe clear switching effects in trilayers. In Fig. 2.6, the magnetization curve of a (305)-oriented F/S/F trilayer together with the field dependence of the resistance of the trilayer is presented. The layer thicknesses are 50, 30, and 150 nm for the bottom F, S, and top F layers, respectively. The T_c of the trilayer is 40 K and the measurement is performed at 44 K. When the bottom LSMO layer switches, the trilayer resistance shows a small downward deviation from the parabolic curve. A large resistance drop occurs upon switching the thicker and rougher top layer. If the resistance-switching effects resulted from switching from P to AP states, an *increase* in resistance of equal magnitude would be expected at the lowest coercive field. In addition, in the region around zero field, between the lowest positive and negative coercive fields, the system would be in the same P state and the curves measured in increasing magnetic field and

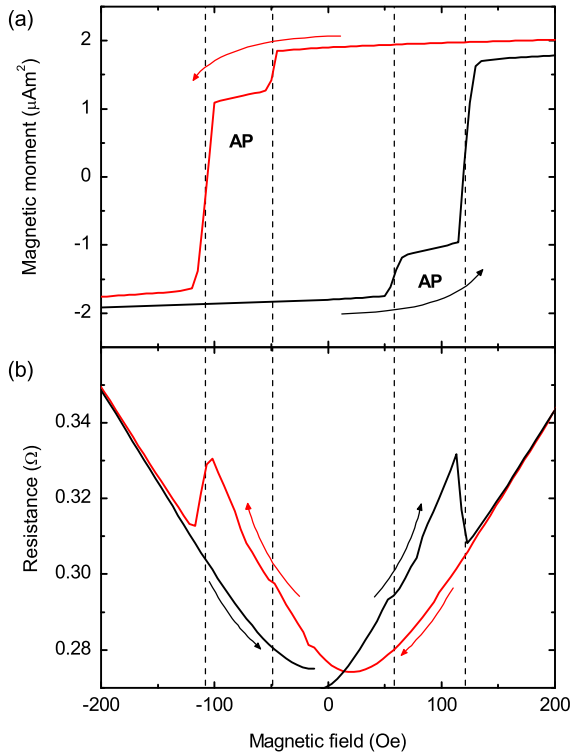

Figure 2.6: Trilayer magnetization hysteresis. **(a)** Magnetization of a (305) F/S/F trilayer (50/30/150 nm) as measured with a VSM at 40 K. The dashed lines correspond to the coercive fields of the top and bottom layer. The highest coercive field is from the thicker top layer. The field range where the magnetization direction of the two layers is AP is indicated. **(b)** Magnetization-induced resistance-switching effects at the superconducting transition (44 K). The apparent discontinuity at zero field is due to a small and smooth temperature drift in the system. Arrows denote the field sweep direction.

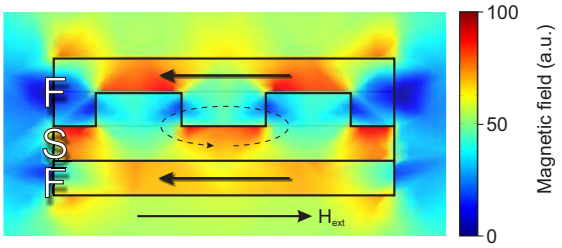

Figure 2.7: Field distribution simulation. Simulated field distribution in an F/S/F trilayer with roughness. Arrows denote the field and magnetization directions. Roughness increases the field in the superconductor. At the thinnest parts of the superconductor, the stray fields (dashed line) are locally opposite to the magnetization direction. The situation as depicted exists when the system has been saturated in a strong negative field (pointing to the left), after which the field has been set to positive, but smaller than the lowest switching field.

decreasing field would have to overlap. The observed switching behavior thus cannot be attributed to switching from P to AP states, but rather arises from the switching of the individual layers. It is interesting that we can observe a small resistance change as a result of the switching of the smooth F bottom layer, while we cannot see it in an STO (305)/F/S bilayer. Apparently, stray fields more easily penetrate the superconductor in trilayers than in bilayers. Similar behavior was recently observed in Ref. 13, where it was attributed to a magnetostatic coupling of the ferromagnetic layers.

Before discussing the data further in terms of stray fields, we would first like to discuss whether a superconducting spin-switch effect could be detectable in our system given the thickness of the superconductor being several times the coherence length of YBCO, which is about 2–3 nm in the *ab* plane. In the original picture by Tagirov,[1] the superconducting spin-switch effect depends on the parameter $(\xi_s/d_s)^2$, in which d_s is the thickness of the superconducting layer and $\xi_s = \sqrt{\hbar D_s/2\pi k_B T_c}$, D_s being the diffusion constant in the superconductor, and $\hbar$ and k_B being the Planck and the Boltzmann constants, respectively. The Ginzburg-Landau coherence length ξ_{GL} at 0 K is approximately equal to ξ_s: $\xi_s = 2\xi_{GL}(0)/\pi$.[31] Although the T_c shift due to the spin-switch effect could be numerically calculated explicitly, we can safely conclude from the small value of $(\xi_s/d_s)^2$ that it would be small. In Ref. 4, a magnetoresistance effect resulting from crossed Andreev reflection processes is predicted up to approximately ten times the coherence length. This approaches our film thicknesses, but it should be taken into account that the electrons traversing the superconductor on the *ab* planes will experience a film thickness of 60 nm due to the 31° angle of the planes with respect to the sample surface. On the other hand, if the (inverse) spin switch originates from the injection of spin-polarized electrons, the characteristic length scale is set by the spin-diffusion length in YBCO, which might well be larger than our film thickness.[18,32]

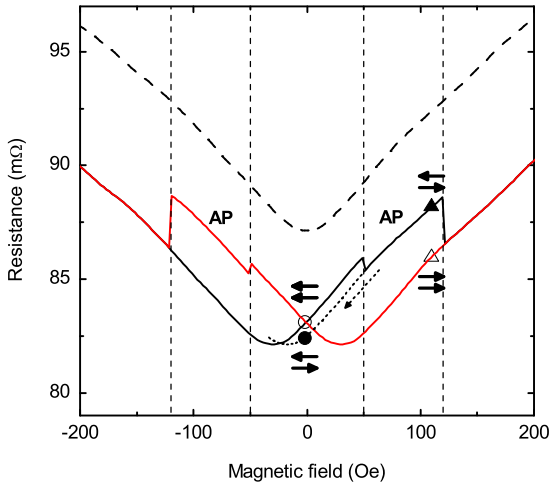

Figure 2.8: Effective field model. Reconstruction of the trilayer magnetic field dependence [solid black (grey) line for increasing (decreasing) magnetic field] starting from the field dependence of a single YBCO layer in the superconducting transition (dashed curve, arbitrary offset). The vertical dotted lines denote the coercive fields of the ferromagnetic layers. The open circle and triangle denote parallel states at different field values at which antiparallel states can be prepared as well (filled symbols). Horizontal arrows represent the magnetization state of the F layers; arrows to the right (left) indicate magnetization in the positive (negative) direction.

2.3.3 Penetrating field model

We have shown above that the resistance-switching effect in trilayers is larger when the top layer switches than when the bottom layer switches. The difference seems to be too large to arise solely from the different thicknesses of the top and bottom layer. We have already seen for the bilayers that roughness can increase the stray fields from the ferromagnetic layers. If the magnetization would be perfectly homogeneous and in plane, the field induced in the superconductor due to the magnetization of the F layers would be very small and in fact only nonzero due to the finite size of the layers. This is the reason that in bilayers switching effects are absent when the F layer is the smooth bottom layer. To substantiate the effects of roughness further, we have carried out finite element simulations on a trilayer with one rough and one smooth F layer. Indeed, a substantial field is predicted to be induced in the superconductor; see Fig. 2.7. In the simulation, we neglect screening effects in the superconductor, which in practice will be small, since the temperature is above T_c. The essential point is that in parts where the superconductor is thin (which contribute the most to the resistance), the induced field will be *opposite* to the magnetization of the layer, and can be either parallel or antiparallel to the applied field, depending on the preparation of the system.

We can therefore write for the total field B_{tot} in the superconductor

$$B_{\mathrm{tot}} = \mu_0 \left(H_{\mathrm{ext}} - \alpha_1 M_1 - \alpha_2 M_2 \right), \tag{2.1}$$

where H_{ext} is the externally applied field and $\alpha_{1,2}$ are positive constants, relating the magnetization in the layers 1 and 2 to the induced field in the superconductor. It will be clear that α is larger for the rougher layer. Now we can combine this with the field dependence of YBCO in the absence of F layers, which is given in Fig. 2.8 by the dashed line. At a large positive field, the resistance will be lower than for the bare YBCO, due to the stray fields induced by the roughness, which are antiparallel to H_{ext}. Upon lowering the field the curve goes through a minimum at positive H_{ext} because of the cancellation of external and stray fields. Further lowering yields a resistance increase because now the external and stray fields point in the same direction. At the coercive fields of the F layers 1 and 2, the curve then shifts down, because the magnetization and therefore the stray fields switch and become again antiparallel. The switching of the ferromagnetic layers leads thus to lateral shifts of the dashed curve at the coercive fields. If we take the coercive fields to be 50 and 120 Oe and use $\mu_0 \alpha_1 M_1 = 5$ Oe and $\mu_0 \alpha_2 M_2 = 25$ Oe, we get the curve represented by the solid line. This would correspond to values for $\alpha_{1,2}$ of 0.2 % and 1 %, respectively. In the light of the previously suggested superconducting spin-switch models, it is surprising that such a simple model can reproduce the observed behavior so well.

To further substantiate this result, we prepared the system to be in the states as indicated by the circles and triangles in Fig. 2.8 and looked at the temperature dependence of the resistance difference between the open and filled symbols. Thus, we investigated the pure effect of the switching of the top or bottom layer on the resistance. It is clear from Fig. 2.9 that we only see resistance differences around the superconducting transition. This is due to the fact that the magnetoresistance of YBCO above T_{c} is small, and below T_{c} large fields are required to suppress superconductivity. Note that an increase in resistance could be interpreted as a decrease in T_{c}. At zero field, the difference between the AP and P states is small, which is due to the fact that it is the smooth bottom layer that is switched between the measurements. The signal is negative, which is clear from inspection of Fig. 2.8 since we are probing the difference between the filled and open circles. When we now compare this to the effect of switching the upper layer again parallel to the bottom layer, i.e., taking the difference between the open and filled triangles, we find a much larger signal of positive sign. It is interesting to see that we can mimic this behavior in a bilayer by measuring in a finite field (below the coercive field) with the magnetization AP and P with respect to the field. In Fig. 2.9(c) we find a resistance-switching effect that has similar sign and magnitude as found in the trilayer.

We have also studied the effect of inhomogeneous magnetization in the layers either by applying a demagnetization procedure or by applying fields perpendicular to the sample. We find in both cases an increase in the resistance, which we

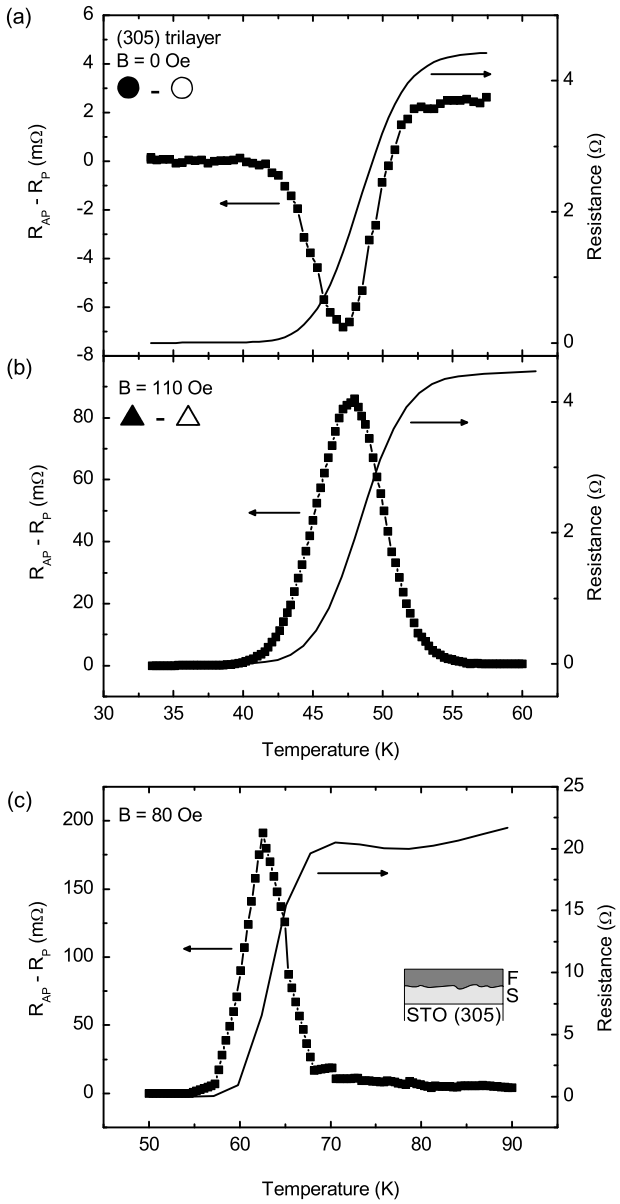

Figure 2.9: Temperature dependence of resistance hysteresis. [**(a)** and **(b)**] Resistance differences (line and symbols) between antiparallel and parallel states for a (305)-oriented F/S/F trilayer (50/30/150 nm). The symbols correspond to the symbols used in Fig. 2.8. The temperature dependence of the resistance itself is indicated by the solid line (corresponding to the scale on the right). The resistance difference between the antiparallel state and the parallel state is opposite in sign and different in size for two different field values, which is difficult to account for within the spin-switch model but has a clear origin in the stray fields from the individual ferromagnetic layers, penetrating the superconductor. **(c)** In an S/F *bilayer* (30/150 nm), at a finite field value below the coercive field, the switching of the ferromagnetic layer yields a comparable signal, supporting the idea that stray fields play an important role in these structures.

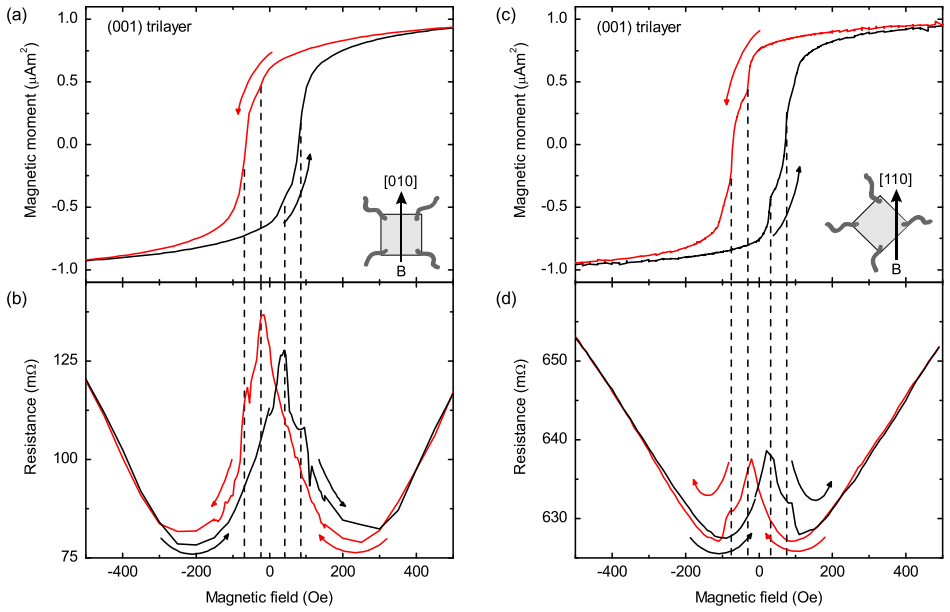

Figure 2.10: Hysteresis effects in (001) grown trilayers. Magnetization [**(a)** and **(c)**] and resistance [**(b)** and **(d)**] measurements of a (001)-oriented F/S/F trilayer (50/30/150 nm) at 61 K in the superconducting transition for different magnetic field orientations as indicated. At the coercive field values, indicated by vertical dashed lines, resistance switching is observed. When the field is applied in the [010] direction, an increase in the resistance is observed between −200 and 200 Oe. This increase arises from in-plane domain-reorientation effects which correspond to the rounding of the magnetization curve. When the field is applied in the [110] easy direction the rounding decreases, resulting in a reduced resistance increase.

attribute to the increased contribution of magnetic stray fields as was also found for F/S/F triple layers with perpendicular magnetic anisotropy by Singh *et al.*.[33]

2.3.4 Switching in (001)-oriented F/S/F trilayers

We have also fabricated a (001)-oriented F/S/F trilayer, using the same layer thicknesses as were used for the (305) trilayer. The trilayer showed a T_c of 60 K. In Sec. 2.2.2, we have seen that for the (001)-oriented structures the magnetization switching is less well defined than for the (305)-oriented structures. Still, we observe resistance-switching effects near the coercive fields, indicated by dashed lines in Fig. 2.10. Our data on (001)-oriented structures are similar to data published in the literature.[17,18] Measurements are taken at 61 K. The resistance-switching effects are superimposed on a background dip which will be discussed below in Sec. 2.3.6. When the field is applied along the [010] direction, an increase in the resistance is observed between −200 and 200 Oe, in the regime where the hysteresis loop of the magnetization starts to open. Switching is not as sharp as in the

case of the (305) trilayers, and we propose that the increase in the resistance here is due to non-homogeneous magnetization as a result of in-plane domain reorientation. Important to note is that at both switching fields the resistance appears to go down rather than up, again suggesting that for each layer the direction with respect to the applied field is more important than their relative orientations. When the field is applied along the [110] easy axis, the magnetization loop is sharper and domain-reorientation effects play less a role. The effect on the resistance is clear; the increase in resistance between −200 and 200 Oe reduces dramatically. Notice that the smoother growth of YBCO on STO (001) diminishes the difference in roughness between the top and bottom layers and the roughness of both interfaces will be comparable to the bottom interface in the (305) structures. We can thus only explain the strong resistance change from domain effects, which certainly are present, as the magnetization loop is still rounded. This probably underlies dissimilarities between the data obtained on (305)- and (001)-oriented trilayers.

Let us now compare the relative magnitude of the resistance-switching effect for the (001) structures with that for the (305) structures. We adopt the definition $\Delta R = (R_{\max} - R_{\min})/R_{\mathrm{nor}}$,[13] in which $R_{\min}$ and $R_{\max}$ are the resistance minimum and the maximum induced by the switching and R_{nor} is the resistance of the trilayer in the normal state. We find $\Delta R = 0.7$ % for the (001) trilayer when the field is applied in the [010] direction and 0.2 % when applied in the [110] direction. For the (305) trilayer the individual contributions of both layers are clearly visible and we find 0.4 % when the top layer is switched and we estimate 0.04 % for the bottom layer. We thus obtain that the magnitude of the resistance switching in the (305) structure is relatively large, given the sharp magnetization switching, which we attribute to the roughness of the corresponding interface. The much smoother bottom interface shows indeed a smaller switching effect than the (001)-oriented structures.

2.3.5 Switchable coupling of F layers

We have made another observation that indicates the importance of the magnetic field penetrating the superconductor in this particular kind of structures. In Fig. 2.11 we show magnetization loops of a (001)-oriented F/S/F trilayer both above T_c at 80 K and well below T_c at 25 K. Although, as stated above, structures with this orientation do not show single-domain magnetization-switching behavior, we can observe a step like magnetization curve well above T_c, arising from two independent coercive fields. When the temperature is lowered to below T_c, this two-step behavior disappears and the coercive fields seem to merge. This behavior is likely due to the sudden change in screening behavior of the S layer. The interplay between magnetic domain structures and vortices were studied in Refs. 34–36. It is well known that superconductivity in S/F hybrid structures can modify the magnetization state.[37–39] While it is difficult here to identify exactly the mechanism leading to the observed coupling of the ferromagnetic layers through superconductivity, it is clear from the measurement that magnetic interactions

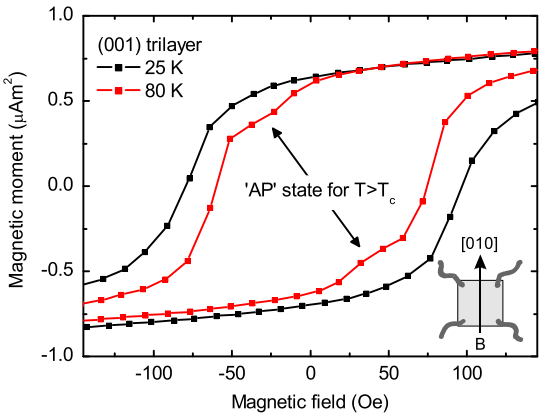

Figure 2.11: Magnetic coupling in trilayers. Upon decreasing the temperature below T_c of the superconductor in a (001) F/S/F trilayer (50/30/150 nm), we observe the loss of the "AP" state due to a change in the mutual influence of the layers. This observation provides further proof that the F layers feel each others' magnetic fields and, therefore, field effects on the superconductor cannot be neglected. AP is put between quotation marks here, since due to the biaxial magnetic anisotropy, it is questionable whether this state is truly antiparallel.

between the F layers through the superconductor take place, which stresses the importance of stray fields in these structures.

2.3.6 High-field behavior of the magnetoresistance

Finally we would like to discuss the high-field behavior of the F/S/F trilayers. In Ref. 17, peaks in the magnetoresistance, centered at zero field, were attributed to spin imbalance due to the injection of spin-polarized carriers in a fashion that resembles the GMR effect. In Fig. 2.12(a) the high-field dependence of a (305)-oriented trilayer at temperatures in the range from 34 to 51 K is displayed. We observe a dip, rather than a peak, which directly reflects the magnetic field dependence of the YBCO in the superconducting transition. Note that the switching effects that have been discussed in Secs. 2.3.1–2.3.5. take place at the bottom of the dip. In a (001)-oriented trilayer, however, we observe the crossover from a peak to a dip depending on the temperature; see Fig. 2.12(b). We propose a straightforward explanation for this crossover. Especially around T_c, small inhomogeneities in the film can lead to large resistance variations over the sample. For example, a small variation in T_c over the sample can lead to a considerable resistance variation over the sample. With the help of a simplified resistor network in Fig. 2.12c it is easy to see that when a current I_{tot} is passed through the current contacts I^+ and I^-, the voltage over the voltage contacts (V_D) will be given

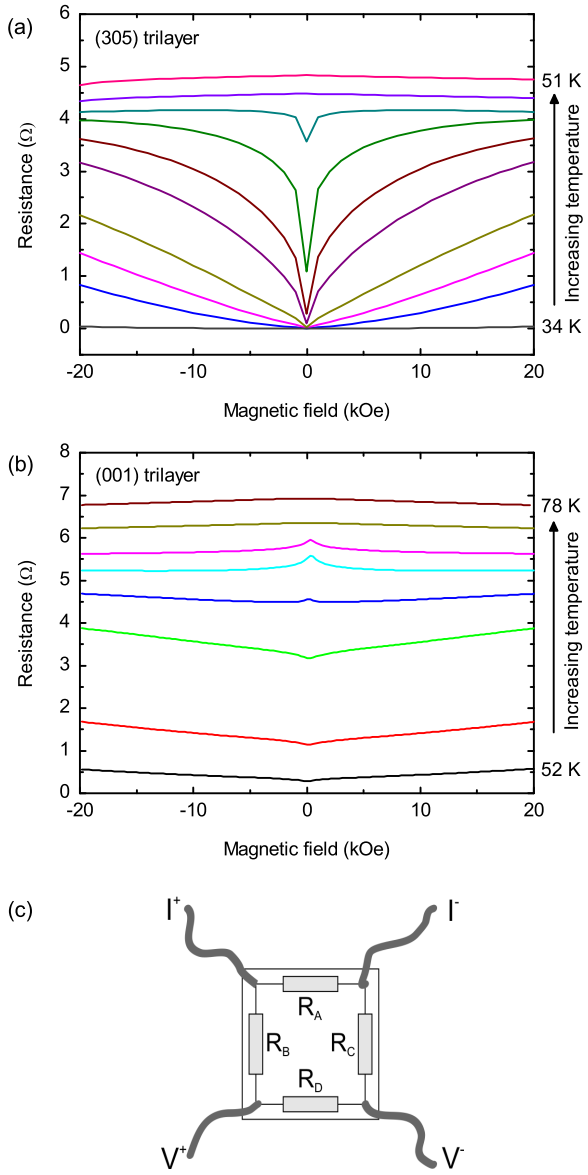

Figure 2.12: High-field magnetoresistance. High-field magnetoresistance behavior for various temperatures from just below T_c to just above T_c for **(a)** (305)- and **(b)** (001)-oriented trilayers. In both trilayers, the bottom F, S, and top F layer are 50, 30, and 150 nm, respectively. In the (305) structure we find a dip, reflecting the magnetoresistance of the YBCO in the superconducting transition. The (001) structures show a crossover from a peak to a dip centered around zero field. **(c)** Resistor network representing a simplified scheme of the sample resistance. When R_B and R_C decrease the measured resistance increases. This effect might explain the peak-to-dip crossover observed in **(b)**.

by $I_{\rm tot}R_{\rm A}R_{\rm D}/(R_{\rm A}+R_{\rm B}+R_{\rm C}+R_{\rm D})$. This means that when the resistances $R_{\rm B}$ and $R_{\rm C}$ *decrease*, the resistance we measure (i.e., $V_{\rm D}/I_{\rm tot}$) *increases*. Indeed, in (305)-oriented trilayers, where superconducting paths are achieved at higher temperatures in the [010] direction than in the $[50\bar{3}]$ direction, the superconducting transition in one direction is sometimes accompanied by a resistance increase in the other direction. In Fig. 2.3 a weak signature of this effect can be seen. In a similar way, if a superconducting path is achieved in the direction perpendicular to the one in which the measurement is performed [in Fig. 2.12(c), for example, $R_{\rm B}$], this will generate a magnetoresistance with a dip, which now appears as a peak in the actual measurement. For lower temperatures, the dip in the initial superconducting path becomes weaker, but a direct superconducting connection between the voltage contacts will appear, resulting in the recovery of a dip.

2.4 Conclusions

We have searched for the superconducting spin-switch effect in F/S/F LSMO/YBCO bi- and trilayers that were optimized for the effect by making the contact between the materials partly in YBCO's crystallographic *ab* plane. Although we find sharp magnetization-switching behavior in these structures, with a well-defined antiparallel state, we do not observe any signature of a spin-switch effect. Instead, our data provide compelling evidence that the observed resistance-switching effects are caused by magnetic stray fields from the ferromagnetic layers, and that also interface roughness can play a role in the observed effects. In the case of the sharply switching (305)-oriented structures, we find that we can explain the data by taking such roughness into account explicitly. In (001)-oriented structures, we have shown that domain reorientation effects have a strong contribution. Moreover, the same description allows explanation of data taken on bilayers with either rough or smooth interfaces. The results may be a warning sign that magnetic field effects, although often not considered to play a role in this kind of structures, might be important after all.

2.5 Implications

In this Chapter we have proposed and shown that an effective field, composed of the field of the ferromagnetic layers and the applied external field, is the important factor determining the inverse superconducting spin effect switch in FSF structures. This conclusion is now being drawn by more groups as the origin of the inverse spin switch effect, although it is argued that the field from the ferromagnetic layer is not only composed of stray fields, but also includes exchange fields[40–42].

Recently it has been proposed that cuprate superconductor/halfmetallic ferromagnet interfaces can host Majorana fermions[43]. Andreev reflection at the SF

interface in the presence of spin-orbit coupling can induce p-wave pairing, resulting in the appearance of Majorana fermions[44,45]. Therefore the YBCO/LSMO system forms an alternative to the superconductor/topological insulator systems presented in the Chapters 4 to 7.

Bibliography

[1] L.R. Tagirov, Phys. Rev. Lett. **83**, 2058 (1999).

[2] A.I. Buzdin, A.V. Vedyayev, and N. V. Ryzhanova, Europhys. Lett. **48**, 686 (1999).

[3] P.G. De Gennes, Phys. Lett. **23**, 10 (1966).

[4] F. Giazotto, F. Taddei, F. Beltram, and R. Fazio, Phys. Rev. Lett. **97**, 087001 (2006).

[5] J.Y. Gu, C.Y. You, J.S. Jiang, J. Pearson, Y.B. Bazaliy, and S.D. Bader, Phys. Rev. Lett. **89**, 267001 (2002).

[6] A. Potenza and C.H. Marrows, Phys. Rev. B **71**, 180503 (2005).

[7] A.Y. Rusanov, S. Habraken, and J. Aarts, Phys. Rev. B **73**, 060505 (2006).

[8] I.C. Moraru, J.W.P. Pratt, and N.O. Birge, Phys. Rev. Lett. **96**, 037004 (2006).

[9] I.C. Moraru, J.W.P. Pratt, and N.O. Birge, Phys. Rev. B **74**, 220507 (2006).

[10] D. Stamopoulos, E. Mainos, and M. Pissas, Phys. Rev. B **75**, 014501 (2007).

[11] G.X. Miao, K.S. Yoon, T.S. Santos, and J.S. Moodera, Phys. Rev. Lett. **98**, 267001 (2007).

[12] R. Steiner and P. Ziemann, Phys. Rev. B **74**, 094504 (2006).

[13] D. Stamopoulos, E. Mainos, and M. Pissas, Phys. Rev. B **75**, 184504 (2007).

[14] D. Stamopoulos, E. Manios, and M. Pissas, Supercond. Sci. and Technol. **20**, 1205 (2007).

[15] G. Carapella, F. Russo, and G. Costabile, Phys. Rev. B **78**, 104529 (2008).

[16] J. H. Park, E. Vescovo, H. J. Kim, C. Kwon, R. Ramesh, and T. Venkatesan, Nature **392**, 794 (1998).

[17] V. Pena, Z. Sefrioui, D. Arias, C. Leon, J. Santamaria, J.L. Martinez, S.G.E. te Velthuis, and A. Hoffmann, Phys. Rev. Lett. **94**, 057002 (2005).

[18] N.M. Nemes,M. Garcia-Hernandez, S. G. E. te Velthuis, A. Hoffmann, C. Visani, J. Garcia-Barriocanal, V. Pena, D. Arias, Z. Sefrioui, C. Leon, and J. Santamaria, Phys. Rev. B **78**, 094515 (2008).

[19] C. Visani, V. Pena, J. Garcia-Barriocanal, D. Arias, Z. Sefrioui, C. Leon, J. Santamaria, N.M. Nemes, M. Garcia-Hernandez, J. L. Martinez, S. G. E. te Velthuis, and A. Hoffmann, Phys. Rev. B **75**, 054501 (2007).

[20] Y. Gim, A. W. Kleinsasser, and J. B. Barner, J. Appl. Phys. **90**, 4063 (2001).

[21] X. Deng, M. Joshi, R. Chakalova, M. S. Colclough, R. Palai, Y. Y. Tse, I. P. Jones, H. Huhtinen, and C. M. Muirhead, Phys. Rev. B **77**, 144528 (2008).

[22] Z. Yang, M. Lange, A. Volodin, R. Szymczak, and V. V. Moshchalkov, Nature Mat. **3**, 793 (2004).

[23] C. Bell, S. Tursucu, and J. Aarts, Phys. Rev. B **74**, 214520 (2006).

[24] S. Mandal, R. C. Budhani, J. He, and Y. Zhu, Phys. Rev. B **78**, 094502 (2008).

[25] W. A. M. Aarnink, E. Reuvekamp, M. A. J. Verhoeven, M. V. Pedyash, G. J. Gerritsma, A. van Silfhout, H. Rogalla, and T. W. Ryan, Appl. Phys. Lett. **61**, 607 (1992).

[26] G. Koster, B. L. Kropman, G. J. H. M. Rijnders, D. H. A. Blank, and H. Rogalla, Appl. Phys. Lett. **73**, 2920 (1998).

[27] M. Mathews, F. Postma, J. Lodder, R. Jansen, G. Rijnders, and D. Blank, Appl. Phys. Lett. **87**, 242507 (2005).

[28] Y. Suzuki, H. Y. Hwang, S. W. Cheong, and R. B. van Dover, Appl. Phys. Lett. **71**, 140 (1997).

[29] E. C. Stoner and E. P. Wohlfarth, Phil. Trans. Roy. Soc. A **240**, 599 (1948), [reprint in: IEEE Trans. Magn. **27**, 3475 (1991)].

[30] B. D. Schrag, A. Anguelouch, S. Ingvarsson, G. Xiao, Y. Lu, P. L. Trouilloud, A. Gupta, R. A. Wanner, W. J. Gallagher, P. M. Rice, and S. S. P. Parkin, Appl. Phys. Lett. **77**, 2373 (2000).

[31] Z. Radovic, L. Dobrosavljevic-Grujic, A. I. Buzdin, and J.R. Clem, Phys. Rev. B **38**, 2388 (1988).

[32] S. Soltan, J. Albrecht, and H.-U. Habermeier, Phys. Rev. B **70**, 144517 (2004).

[33] A. Singh, C. Surgers, M. Uhlarz, S. Singh, and H. von Lohneysen, Appl. Phys. A **89**, 593 (2007).

[34] F. Laviano, L. Gozzelino, E. Mezzetti, P. Przyslupski, A. Tsarev, and A. Wisniewski, Appl. Phys. Lett. **86**, 152501 (2005).

[35] F. Laviano, L. Gozzelino, R. Gerbaldo, G. Ghigo, E. Mezzetti, P. Przyslupski, A. Tsarou, and A. Wisniewski, Phys. Rev. B **76**, 214501 (2007).

[36] L. Gozzelino, F. Laviano, P. Przyslupski, A. Tsarou, A. Wisniewski, D. Botta, R. Gerbaldo, and G. Ghigo, Supercond. Sci. Technol. **19**, S50 (2006).

[37] C.Monton, F. de la Cruz, and J. Guimpel, Phys. Rev. B **75**, 064508 (2007).

[38] H.-Y.Wu, J. Ni, J.-W. Cai, Z.-H. Cheng, and Y. Sun, Phys. Rev. B **76**, 024416 (2007).

[39] C.Monton, F. de la Cruz, and J. Guimpel, Phys. Rev. B **77**, 104521 (2008).

[40] J. Salafranca, S. Okamoto, Phys. Rev. Lett. **105**, 256804 (2010).

[41] N.M. Nemes, C. Visani, Z. Sefrioui, C. Leon, J. Santamaria, M. Iglesias, F. Mompean, and M. Garcia-Hernandez, Phys. Rev. B **81**, 024512 (2010).

[42] Y. Liu, C. Visani, N.M. Nemes, M.R. Fitzsimmons, L.Y. Zhu, J. Tornos, M. Garcia-Hernandez, M. Zhernenkov, A. Hoffmann, C. Leon, J. Santamaria, and S.G.E. te Velthuis, Phys. Rev. Lett. **108**, 207205 (2012).

[43] S. Takei, B.M. Fregoso, V. Galitski, and S. Das Sarma, ArXiv:1206.3226v1 (2012).

[44] M. Duckheim and P.W. Brouwer, Phys. Rev. Lett. **83**, 054513 (2011).

[45] S.B. Chung, H.J. Zhang, X.L. Qi, S.C. Zhang, Phys. Rev. B **84**, 060510 (2011).

Chapter 3 Nonlocal Cooper pair Splitting in a *p*S*n* Junction

Abstract

Perfect Cooper pair splitting is proposed, based on crossed Andreev reflection (CAR) in a p-type semiconductor-superconductor-n-type semiconductor (pSn) junction. The ideal splitting is caused by the energy filtering that is enforced by the band structure of the electrodes. The pSn junction is modeled by the Bogoliubov-de Gennes equations and an extension of the Blonder-Tinkham-Klapwijk theory beyond the Andreev approximation. Despite a large momentum mismatch, the CAR current is predicted to be large. The proposed straightforward experimental design and the 100% degree of pureness of the nonlocal current open the way to pSn- structures as high quality sources of entanglement.

3.1 Introduction

Spatially separated entangled electron pairs arise in hybrid normal-metal - superconductor structures. Andreev reflection (AR) is the conversion of an electron into a hole at the interface between a normal-metal or semiconductor and a superconductor[1]. In nonlocal (or crossed) Andreev reflection (CAR) the conversion is over two electrodes maintaining the singlet state[2,3]. This makes CAR a promising source of locally separated entangled electrons and building block for solid state Bell inequality experiments, quantum computation and quantum teleportation[4–9].

The Bell inequality can only be violated when the CAR fraction is larger than $1/\sqrt{2}$ of the total current[10]. Despite intensive investigation, the CAR fraction is usually small due to competing processes[11–17]. Aside from local AR, tunneling of a particle from one lead to another can occur. Elastic cotunneling (EC) is to lowest order in tunneling amplitude equal in magnitude and opposite in sign to CAR, resulting in a vanishing nonlocal conductance[18]. Including higher order terms, which become important in more transparent junctions, unfortunately provides EC to be the dominant process[19].

Several proposals have been put forward to enhance the CAR current. Using ferromagnetic-halfmetals (F) as leads can result in dominant CAR in an antiparallel magnetization alignment[3], though spin entanglement is then questionable.

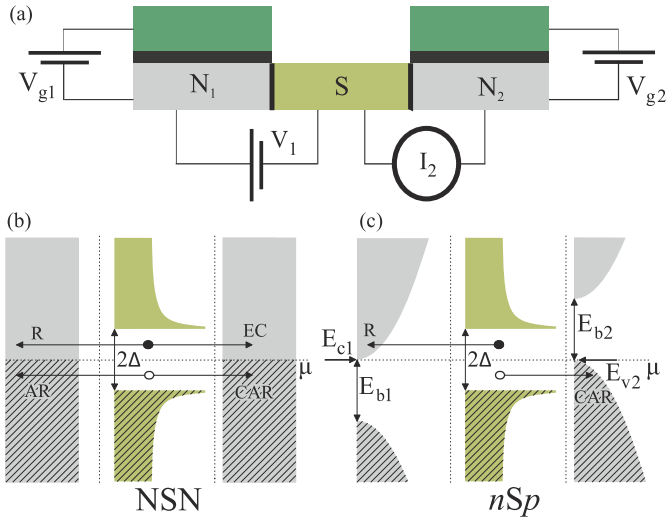

Figure 3.1: The Cooper pair beam splitter. **(a)** NSN structure with gates attached to the semiconductor. By applying gate-voltages, the semiconductor bands in each electrode can be tuned with respect to the Fermi energy. A bias voltage applied at the left NS interface results in a nonlocal conductance at the second interface. **(b)** In standard NSN structures an incident electron can result in normal reflection (R), AR, EC, and CAR. **(c)** In an *n*S*p* junction it is possible to have perfect nonlocal Cooper pair splitting.

Pure nonlocal Cooper pair splitting is predicted in a superconductor-topological insulator structure[20], but the fabrication will be challenging. Both the electromagnetic environment[21] and a change in the density of states (DOS) of a superconductor due to an ac bias[22] can result in dominant CAR, though the influences are expected to be small. A larger effect is predicted by Cayssol[23] in an *n*-type graphene-superconductor-*p*-type graphene junction. However, full cancellation of EC and AR is only at precise biasing to the Dirac point and at a small range of the energy spectrum so that the current is not completely carried by CAR. Optimization of CAR may also be realized by using the Coulomb interaction[4]. Recent experiments indicated great potential of using the energy to discriminate CAR[16,17], although the splitting efficiency is yet small.

Here, we propose a strategy for ideal 100% nonlocal Cooper pair splitting, with no contributions from AR and EC, in a relatively straightforward device. Making use of the energy difference between the incoming electron and the Andreev reflected hole, in combination with bandstructure imposed forbidden energies, enables the cancellation of both AR and EC individually, while still having a significant CAR probability. This idea is shown in Fig. 3.1. The asymmetry of the bandstructure allows only CAR to occur since particles due to EC and AR will end up in forbidden states in the band structure, the band alignment being tunable by proper gating.

3.1.1 Energy filtering with electrodes

A wide range of materials are suitable as electrodes. Examples are nanowires, where the bandgap can be tuned by the length of the wire, minigap semiconductors such as bilayer graphene, and narrow band semiconductors in general. Impurity bands can be used when there is significant density of states at an energy $\pm\Delta$ from the semiconducting bandgap, generally in the case of low doping concentrations. Energy bands or levels that arise from quantum confinement in general can be used, as long as gapped energy regions exist that prohibit AR and EC. The proposed type of energy filtering is not only of use as Andreev entangler, but can also serve as energy beam splitter in, for example, FSF devices. This opens up an alternative route towards Bell inequality experiments; the spin may be employed to split the Cooper pairs, since the energy can be utilized for the read out.

3.1.2 Extended BTK model

We model the NSN system by extending the classical Blonder-Tinkham-Klapwijk model[24] to three dimensions and by including the second interface. The BTK model has been used in modeling SNS and FSF structures where the dimension of the sandwiched layer is close to ξ[25,26]. In the present case of a pSn junction, the need to model in three dimensions stems from the large Fermi momentum mismatch between a semiconductor and a superconductor. Because of the conservation of momentum parallel to the interfaces, a critical angle between momentum and interface normal exists above which no transfer can take place. Each of the AR, CAR and EC probabilities is characterized by an energy and angle dependent effective barrier. Since excitation energies are comparable to or larger than the Fermi energy of the semiconductor in our system, we will go beyond the Andreev approximation that takes all momenta equal.

We describe the pSn structure shown in Fig. 3.1 with the time independent Bogoliubov-de Gennes equations given by

$$\begin{pmatrix} \hat{H}(\mathbf{r}) & \Delta(\mathbf{r}) \\ \Delta^*(\mathbf{r}) & -\hat{H}(\mathbf{r}) \end{pmatrix} \Psi(\mathbf{r}) = E\Psi(\mathbf{r}). \tag{3.1}$$

$\Psi(\mathbf{r}) = (u, v)^T$ is the wave function in Nambu (electron-hole) space. We assume that $\Delta(\mathbf{r}) = 0$ in the normal regions N_1 ($z < 0$) and N_2 ($z > d$), and $\Delta(\mathbf{r}) = \Delta_0$ in the superconducting region S ($0 < z < d$), d being the superconductor width. The use of these rigid boundary conditions is warranted by the large Fermi momentum mismatch across the interfaces, which effectively reduces the coupling between the layers. A specular barrier is included at the interfaces, resulting in $U(\mathbf{r}) = H_1\delta(z) + H_2\delta(d - z)$. Inside a region we assume an isotropic band structure. Incorporating the conserved momentum component parallel to the interfaces into the Hamiltonian allows us to simplify Eq. (3.1) to a 1D system with an effective 1D Hamiltonian, given by $\hat{H}(z) = -\frac{\partial}{\partial z}\frac{\hbar^2}{2m^*(z)}\frac{\partial}{\partial z} + U(z) - \mu^*$, where

$\mu^* = (\mu - E_p)\cos^2\theta_\pm \mp \sqrt{E^2-\Delta^2}\sin^2\theta_\pm$. The angle $\theta_\pm$ is the angle between the direction of the electron (+) or hole (-) and the normal of the interface and can be found through the Snell-Descartes law $\sin\theta_t = r_k \sin\theta_i$ where θ_i and θ_t are the respective incidence and transmission angle and r_k is the ratio of the incoming and transmitted moment. For large r_k, $\theta_t \approx 0$ and particles in the superconductor travel normal to the interface. μ is the chemical potential and E_p is the potential energy in each layer tuned by the gate voltages. Our ansatz for Ψ in the regions N_1, S, and N_2, then becomes

$$\Psi_{N_1} = \begin{pmatrix} e^{iq_1^+ z} + b\, e^{-iq_1^+ z} \\ a\, e^{iq_1^- z} \end{pmatrix}, \Psi_{N_2} = \begin{pmatrix} c\, e^{iq_2^+ z} \\ d\, e^{-iq_2^- z} \end{pmatrix},$$
$$\Psi_S = \psi^+ \begin{pmatrix} u_0 \\ v_0 \end{pmatrix} + \psi^- \begin{pmatrix} v_0 \\ u_0 \end{pmatrix}, \tag{3.2}$$

where $\psi^+ = \alpha\, e^{ik^+ z} + \chi\, e^{-ik^+ z}$, $\psi^- = \beta\, e^{-ik^- z} + \eta\, e^{ik^- z}$ and $u_0^2 = 1 - v_0^2 = \frac{1}{2}(1 + \frac{\sqrt{E^2-\Delta^2}}{E})$[24]. Using conservation of $k^{||}$ we find the moments in the z-direction in each layer given by $k^\pm = \cos\theta_\pm \sqrt{\frac{2m^*}{\hbar^2}\left(\mu - E_p \pm \sqrt{E^2-\Delta^2}\right)}$. This implies a critical angle given by $\theta_C(E) = \arcsin(r_k^{-1})$. In a *p*S*n* junction with $E_p \neq 0$ in the electrodes, CAR is enhanced since CAR has the lowest critical angle as compared to the other scatter processes[23].

The system can be solved by applying the boundary conditions $\Psi_{N_{1,2}}(0^-, d^+) = \Psi_S(0^+, d^-)$ together with $\frac{\hbar^2}{2m_S^*}\frac{\partial \Psi_S}{\partial z}(0^+, d^-) - \frac{\hbar^2}{2m_{N_{1,2}}^*}\frac{\partial \Psi_{N_{1,2}}}{\partial z}(0^-, d^+) = \pm H_{1,2}\Psi$. This extended BTK model reproduces results in NSN structures found previously by other models. The nonlocal conductance G_{NL} vanishes due to the cancellation of CAR by EC in the tunnel limit[18], while EC is dominant in transparent regimes[19], and the electrode separation distance dependence of G_{NL} is exponential. Charge imbalance is not taken into account in this model, but the CAR enhancement effects as described in this Letter also occur in the range $E < \Delta$ at temperatures $T \ll T_c$, where this effect is absent[27].

3.1.3 Implementing semiconductor bandgaps

In order to enhance the CAR current to 100%, p and n type semiconductors will be implemented now as the two electrodes. We investigate the generic example of a semiconductor possessing a band gap $E_b \gg \Delta$, one valence band and one conduction band, each with parabolic dispersion. Even scattering processes at energies within the forbidden semiconducting band gap have nonzero probabilities at the interfaces, influencing other processes, and thus need to be taken into account when solving the wave equations. Still, the wave function of these particles decay exponentially in the electrodes and do not contribute to the current by themselves, since we consider electrode lengths much larger than ξ.

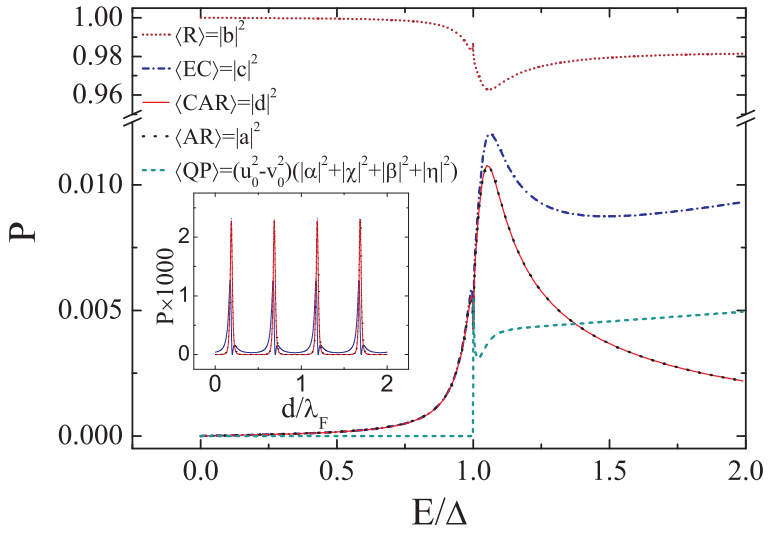

Figure 3.2: Energy dependence of the averaged reflection and transmission probabilities. $Z = 0$ and $E_{c1} = \mu = E_{v2} = 5.8 \times 10^4 \Delta$, resulting in an effective energy dependent barrier. Consequently, the probability $\langle CAR \rangle$ is significant and almost equal to $\langle EC \rangle$ for $E<\Delta$. Because of the small superconducting width $d = \frac{1}{2}\xi$, $\langle AR \rangle$ does not reach unity and $\langle R \rangle$ does not vanish at $E=\Delta$. The inset shows the dependence of the probabilities on the width of the superconductor at $E=\frac{1}{2}\Delta$; Fabry-Perot resonances occur on the Fermi wavelength scale.

3.2 Results

Figure 3.2 shows the numerically obtained probabilities for perpendicular incidence, zero bias, transparent interfaces (the BTK barrier strength $Z = \frac{H}{\hbar v_F} = 0$[24]) and in a regime of large momentum mismatch. The probabilities are given by the absolute squared values of the prefactors in ansatz Eq. (3.2). Normal reflection (R), EC, AR, and CAR probabilities are considered at the respective interfaces, while the quasiparticle (QP) states in the superconductor are taken far from the interface thereby vanishing at energies below Δ. In the regime of large momentum mismatch, the angle dependence below the critical angle and the bias and gating dependence of the probabilities follow $P(E) = P_0(E)|\frac{E-eV-E_{c,1}}{E}|\cos^2(\theta)$, where P_0 refers to the unbiased probability at perpendicular incidence. As an example, we consider Al as the superconductor, resulting in a large effective barrier originating from a large ratio $\mu/\Delta = 5.8 \times 10^4$. Despite the effective barrier, CAR is found to have a considerable magnitude for d being close to the Bardeen-Cooper-Schrieffer coherence length $\xi = \frac{\hbar v_{F,S}}{\pi\Delta}$. Averaging the probabilities by $\langle P \rangle = \int_{d-1/2\lambda_{F,S}}^{d+1/2\lambda_{F,S}} P(z)dz$ with $\lambda_{F,S}$ the Fermi wavelength in the superconductor is necessary in order to let Fabry-Perot resonances vanish, in practice washed out by roughness.

3.2.1 Nonlocal currents

The current density in the electrodes is obtained from

$$J_d^z = \frac{1}{V_d} \sum_{\mathbf{k},\sigma,\pm} \mathbf{J}_q(\mathbf{k},\pm)\hat{\mathbf{e}}_z f(\mathbf{k},\pm).$$

Here, d is the dimension and V_d the volume of the system, the sum $\pm$ is over electrons and holes, f is the nonequilibrium distribution and the charge current is defined by $\mathbf{J}_{q,e(h)} = \frac{e\hbar}{m}\mathrm{Im}\left[u^*(v^*)u(v)\right]$. From this it follows that the CAR and EC current are opposite in sign, since the respective group velocities in N_2, given in the ansatz Eq. (3.2), are opposite in sign. Finally, the current in an electrode becomes $I = \frac{A}{2\pi^3\hbar^2}\int dE f \int_0^{\frac{\pi}{2}} d\theta \cos\theta \sin\theta \sum_{\pm} |\mathbf{k}| m J_q^z$, where A is the cross-sectional area. The integration is over all energy modes that contribute to the tunneling, limited by the lowest DOS of the initial and final state for a certain process. Even nonideal *p*S*n* junctions with nonvanishing DOS in the bandgap or improper Fermi level aligning enhance CAR, since the DOS will be lowest for the AR and EC processes. The distribution functions are given by $f_1 = f_0(E - eV_{N1}) - f_0(E - eV_S)$ and $f_{2,e(h)} = f_0(E - eV_{N1}) - f_0(E - e\max[V_s; V_{N2}(-V_{N2})])$, with $f_0(E)$ the Fermi distribution function. Positive or negative biasing at the second electrode decreases the EC or CAR processes, respectively. Current flowing to the superconductor is defined positive, so AR and CAR are positive in sign and EC negative.

Figure 3.3 shows the IV characteristics for a *p*S*n* junction with fixed gate voltages, so that $E_{c1} + 0.6\Delta = \mu = E_{v2}$. At negative bias across the first interface, the first electrode has available states above and below μ whereas the second electrode has only states below μ. AR and EC are therefore possible, while CAR is prohibited. For positive bias voltages, direct electron transfer is no longer possible and the nonlocal current is carried by CAR only. AR is significantly reduced by the critical angle and limited DOS and totally vanishes above eV>0.6Δ, where available states for AR are absent. The device works as a perfect Cooper pair splitter for 0.6Δ<eV<Δ. Above the gap a quasiparticle current appears in the superconductor resulting in a lower splitting efficiency.

Maximizing the bias regime in which CAR = 100% can be achieved by tuning the gate voltage such that always $E_{c1} = \mu = E_{v2}$, irrespective of the bias voltage. This bias situation is shown in Fig. 3.4. For all positive bias voltages below Δ, CAR = 100%. AR and EC are forbidden due to the bandgap in the electrodes. The DOS for incoming electrons is equal to the DOS for outgoing holes and there is no critical angle lowering the CAR probability, since $E_P = 0$. Consequently, the nonlocal current is maximized to a relatively large value, being typically a few µA.

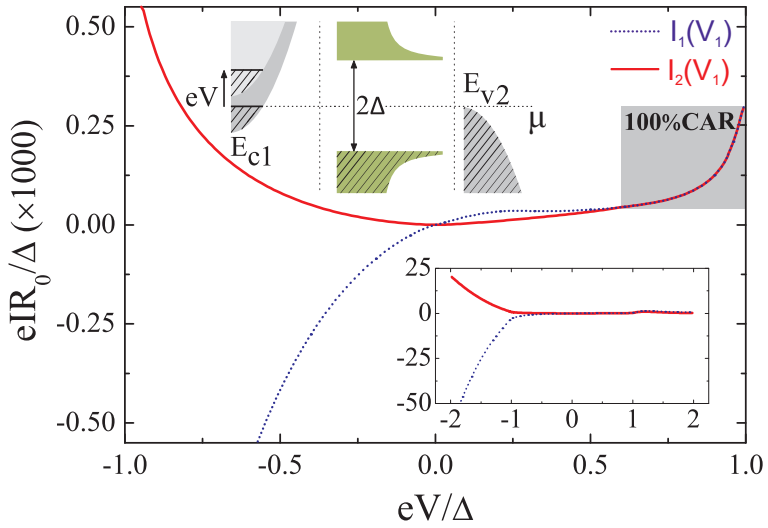

Figure 3.3: *IV* **characteristics for fixed gate voltages.** Local (I_1) and nonlocal (I_2) current dependence on the bias voltage (V_1) for a fixed gate voltage $eV_{g1} = 0.6\Delta$ (see upper inset). $E_{c1} + 0.6\Delta = \mu = E_{v2} = 5.8 \times 10^4\Delta$, $d = \frac{1}{2}\xi$ and $Z = 0$. The momentum mismatch results in an effective barrier. R_0 is the Sharvin resistance at $eV = \Delta$. Negative biasing ($eV < 0$) leads to a nonlocal current due to EC, whereas positive biasing ($eV > 0$) results in CAR. AR is possible up to 0.6Δ, so that in the range $0.6\Delta < eV < \Delta$ perfect Cooper pair splitting occurs. QP current appears at $eV > \Delta$ shown in the lower inset.

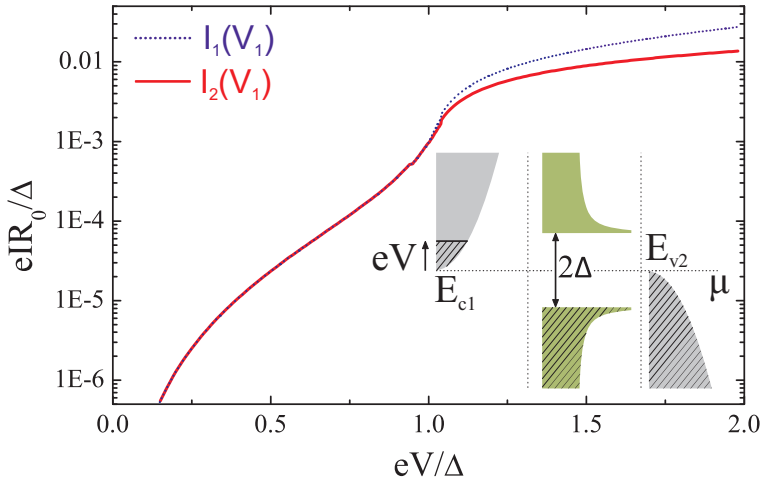

Figure 3.4: *IV* **characteristics with ideal gate tuning.** Local (I_1) and nonlocal (I_2) current dependence on the bias voltage (V_2) for ideal gating, $E_{c1} = \mu = E_{v2} = 5.8 \times 10^4 \Delta$ regardless of the bias voltage. $d = \frac{1}{2}\xi$ and $Z = 0$. The momentum mismatch results in an effective barrier. R_0 is the Sharvin resistance at $eV = \Delta$. For $eV < 0$ no process is possible, but in the range $0 < eV < \Delta$ only CAR is possible and we observe pure entangled current $I_1 = I_2$. QP current appears at $eV > \Delta$, lowering the CAR fraction.

3.3 Discussion

We now address the question which systems would be best suited. The discrimination between AR, EC, and CAR leading to 100% crossed Andreev reflection in a *p*S*n* junction is caused by: the forbidden band gap (which is our main effect leading to 100% CAR), the variation in density of states and the critical angle. The elasticity mandatory for these three effects is typically a less stringent condition than the superconductor width being comparable to ξ, necessary to have a significant nonlocal current. With current nanolithography methods and using Al as superconductor these requirements are easily fullfilled. For the semiconductors, InAs two-dimensional electron gases are ideal candidates, since no Schottky barrier is formed in contact to Al[28,29]. The effect of the critical angle may vanish in the diffusive limit, but perfect Cooper pair splitting due to the forbidden bandgap remains robust against disorder. Nb/InAs structures are therefore also suited. Even though $\xi_{Nb} < \xi_{Al}$, the larger superconducting gap of Nb simplifies the band alignment and increases the magnitude of the nonlocal current. Schottky barriers reduce the nonlocal current, but the splitting is found to remain ideal when using a nonzero barrier strength. Al/GaAs heterostructures are, therefore, suitable as well[30]. Finally, we mention that electronic gate controllable InAs nanowires have been contacted to Al with high interface transparency[31], making it an ideal system

for entanglement experiments where a reduced number of propagating modes are required.

In conclusion, we have proposed a $p\mathrm{S}n$ junction that can be used to prepare a pure Bell state by forward biasing and can act as a perfect Cooper pair splitter by reversed biasing, while having significant currents.

3.4 Experiments and theory based on energy filtering

The best known Cooper pair beam splitters are based on superconductor quantum dot structures [16,17]. The initial motivations for these devices are based on Coulomb interactions, lowering local Andreev reflection by repulsive interaction of two particles on the same dot. However, it turned out that the splitting efficiency in these devices were beyond the theoretical predictions. A careful analysis [32] of these systems showed that the main efficiency increase is due to energy filtering, beneficial for crossed Andreev reflection, as explained in this Chapter [33]. Utilizing quantum confinement, Coulomb interaction and spin orbit interaction to obtain sharp interfaces between bands and bandgaps increasing the energy filtering performance thereby providing good prospects for the realization of high quality Cooper pair beam splitters.

Interestingly, the pSn-junction is theoretically already been used in more complex devices. Using this energy filtering mechanism in $SNSNS$ systems, nonlocal quartets can be produced opening a new route towards entanglement generation [34].

Bibliography

[1] A.F. Andreev, Zh. Eksp. Teor. Fiz. **46**, 1823 (1964) [Sov. Phys. JETP **19**, 1228 (1964)].

[2] J.M. Byers and M.E. Flatté, Phys. Rev. Lett. **74**, 306 (1995).

[3] G. Deutscher and D. Feinberg, Appl. Phys. Lett. **76**, 487 (2000).

[4] P. Recher, E.V. Sukhorukov, and D. Loss, Phys. Rev. B **63**, 165314 (2001).

[5] G.B. Lesovik, T. Martin and G. Blatter, Eur. Phys. J B **24**, 287 (2001).

[6] N.M. Chtchelkatchev, G. Blatter, G.B. Lesovik, and T. Martin, Phys. Rev. B **66**, 161320(R) (2002).

[7] N. M. Chtchelkatchev, JETP Lett. **78**, 230 (2003) [Pis'ma Zh. Eksp. Teor. Fiz. **78**, 265 (2003)].

[8] K. V. Bayandin, G.B. Lesovik, and T. Martin, Phys. Rev. B **74**, 085326 (2006).

[9] S. Kawabata, J. Phys. Soc. Jap. **70**, 1210 (2001).

[10] O. Gühne and G. Tóth, Phys. Rep. **474**, 1 (2009).

[11] A. Brinkman and A.A. Golubov, Phys. Rev. B **74**, 214512 (2006).

[12] S. Russo, M. Kroug, T.M. Klapwijk, and A.F. Morpurgo, Phys. Rev. Lett. **95**, 027002 (2005).

[13] P. Cadden-Zimansky and V. Chandrasekhar, Phys. Rev. Lett. **97**, 237003 (2006).

[14] A. Kleine, A. Baumgartner, J. Trbovic, and C. Schönenberger, Europhys. Lett. **87**, 27011 (2009).

[15] D. Beckmann, H.B. Weber and H.v. Löhneysen, Phys. Rev. Lett. **93**, 197003 (2004).

[16] L. Hofstetter, S. Csonka, J. Nygård, and C. Schönenberger, Nature **461**, 960 (2009).

[17] L. G. Herrmann, F. Portier, P. Roche, A. Levy Yeyati, T. Kontos, and C. Strunk, Phys. Rev. Lett. **104**, 026801 (2010).

[18] G. Falci, D. Feinberg, and F.W.J. Hekking, Europhys. Lett. **54**, 255 (2001).

[19] M.S. Kalenkov and A.D. Zaikin, Phys. Rev. B **75**, 172503 (2007).

[20] J. Nilsson, A.R. Akhmerov and C.W.J. Beenakker, Phys. Rev. Lett. **101**, 120403 (2008).

[21] A. Levy Yeyati, F.S. Bergeret, A. Martín-Rodero, and T.M. Klapwijk, Nature Phys. **3**, 455 (2007).

[22] D.S. Golubev and A.D. Zaikin, Europhys. Lett. **86**, 37009 (2009).

[23] J. Cayssol, Phys. Rev. Lett. **100**, 147001 (2008).

[24] G.E. Blonder, M. Tinkham and T.M. Klapwijk, Phys. Rev. B **25**, 4515 (1982).

[25] U. Schüssler and R. Kümmel, Phys. Rev. B **47**, 2754 (1993).

[26] T. Yamashita, S. Takahashi and S. Maekawa, Phys. Rev. B **68**, 174504 (2003).

[27] C.J. Pethick and H. Smith, J. Phys. C: Solid State Phys. **13**, 6313 (1980).

[28] H. Takayanagi, T. Akazaki, and J. Nitta, Phys. Rev. Lett. **75**, 3533 (1995).

[29] T. Schäpers, J. Malindretos, K. Neurohr, S. Lachenmann, A. van der Hart, G. Crecelius, H. Hardtdegen, H. Lüth, and A.A. Golubov, Appl. Phys. Lett. **73**, 2348 (1998).

[30] R. Taboryski, T. Clausen, J. Bindslev Hansen, J.L. Skov, J. Kutchinsky, C.B. Sørensen, and P.E. Lindelof, Appl. Phys. Lett. **69**, 656 (1996).

[31] Y.J. Doh, J.A. van Dam, A.L. Roest, E.P.A.M. Bakkers, and L.P. Kouwenhoven, Science **309**, 272 (2005).

[32] P. Burset, W.J. Herrera, and A. Levy Yeyati, Phys. Rev. B. **84**, 115448 (2011).

[33] M. Veldhorst and A. Brinkman, Phys. Rev. Lett. **105**, 107002 (2010).

[34] A. Freyn, B. Doucot, D. Feinberg, and R. Mélin, Phys. Rev. Lett. **106**, 257005 (2011).

Chapter 4 Nonlocal spin entangled Andreev reflection, fractional charge and Majorana fermions in topological bilayer exciton condensate junctions

Abstract

We study Andreev reflection and Josephson superconductivity in topological bilayer exciton condensates. 100% spin entangled nonlocal currents with high amplitudes can arise in these systems, interesting for entanglement sources in quantum computation. Zero energy modes appear, signified by fractional charges flowing in opposite directions through the two different layers of the bilayer condensate. These modes can become Majorana fermions in magnetic fields, encoded over two separated layers, or by coupling the surfaces of a bilayer by a topological insulator, potentially leading to room temperature Majorana fermions.

4.1 Introduction

Recently, exciton condensation has been predicted in three dimensional topological insulators, which could potentially survive up to room temperature [1]. The topological bilayer exciton condensates (TECs) arises from the pairing of carriers in closely spaced top and bottom surfaces of a topological insulator (TI). The strong experimental progress in tuning the Fermi energy inside the bulk bandgap bears promise for the creation of these systems [2,3]. Motivated by the similarities between excitonic and superconducting condensates [4,5], we study Andreev reflection on and Josephson junctions consisting of TECs.

Nonlocal entangled electrons can be created via singlet superconductor Cooper pair splitting by means of crossed Andreev reflection [6–11]. However, the current is usually only for a small part entangled due to the competing processes of normal Andreev reflection and elastic cotunneling [8]. Proposals to optimize crossed Andreev reflection have focused on the electrodes contacting the superconductor. The fraction of entangled particles can be strongly increased by using ferromagnetic electrodes in an antiparallel magnetization [7], and could even reach 100% in

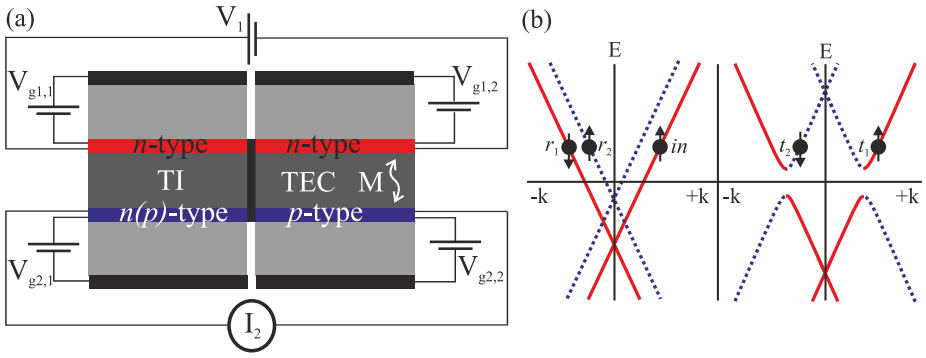

Figure 4.1: Topological bilayer exciton junction. **(a)** Gate tunable TI-TEC heterostructure. Exciton condensation results from the Coulomb interaction between the n and p-type layers. A voltage V_1 over the top surface states creates a nonlocal current I_2 through the bottom surface states. **(b)** Allowed transport processes in the device; the arrows denote the spin normal to the interface, $\hat{\mathbf{e}}_x$, and solid red (dotted blue) indicates the top (bottom) surface, respectively. An incoming top surface electron (in) can be reflected (r_1) and Andreev reflected (r_2) as an electron. Transmission occurs as electrons in an electron-like branch (t_1) and hole-like branch (t_2). Elastic cotunneling has a vanishing probability due to the large intrinsic TI bulk bandgap.

a p-type semiconductor - superconductor - n-type semiconductor junction[11], discussed in Chapter 3. Still, these proposals rely on very specific configurations and are always limited by the critical temperature of the superconductor.

A superconducting Josephson junction is predicted to host emergent Majorana fermions if the interlayer is made out of topological insulators[12]. The search for the Majorana fermion is of practical relevance as these particles might serve as decoherence immune qubits in quantum computation. Enlarging the possibilities to find this particle in alternative systems, is therefore of great importance.

In this Letter, we will show that a TEC can serve as an appealing alternative for superconducting systems. Andreev reflection on TECs is nonlocal, and has the potential to become a 100% ideal entanglement source. Topological protection results in high Andreev reflection amplitudes and the spin-momentum locking opens new ways to read out the entanglement quantities. TEC Josephson junctions exhibit zero modes with fractional charge flowing in opposite directions through both surfaces and the modes can become Majorana fermions by introducing magnetic fields or by coupling of the two surfaces.

4.2 Topological exciton condensation

When the two surfaces of a topological insulator material, which is insulating in the bulk with a finite bandgap[13,14], are sufficiently close, Coulomb interaction can induce exciton condensation[1], shown in Fig. 4.1. Electrical gates attached to the exciton condensate are used to tune the top (bottom) surface of the topological

insulator to be of $n(p)$-type, resulting in an attractive Coulomb interaction $\hat{M}$, that drives the system to exciton condensation.

The surface states of a topological insulator can be described by

$$\hat{H} + \mu_{T(B)}\hat{I} = +(-)v_{T(B)}\boldsymbol{\sigma}\cdot\hat{\mathbf{p}}. \tag{4.1}$$

Here, the momentum $\hat{\mathbf{p}} = -i\hbar\nabla$ of the topological insulator is coupled to the spin, and $\boldsymbol{\sigma} = (\sigma_x, \sigma_y)$ are the Pauli spin matrices. The Fermi velocity $v_{T(B)}$ represents the Dirac velocity in the top (T) and bottom (B) layer, and the $(+)$- is due to the different chiralities residing at the two sides. The Fermi energy $\mu_{T(B)} = \mu + E_{p,T(B)}$ is given by the intrinsic chemical potential μ and the potential energy E_p, tuned by the electrical gates. Since the top and bottom layers can be electrically gated individually, it is always possible to tune towards $\mu_T = \mu_B$. Now we include the Coulomb interaction $\hat{M}$, so that the Hamiltonian after mean field approximation is given by

$$\hat{H} + \mu\hat{I} = \begin{pmatrix} v_T\boldsymbol{\sigma}\cdot\hat{\mathbf{p}} - E_{p,T} & \hat{M} \\ \hat{M}^* & -v_B\boldsymbol{\sigma}\cdot\hat{\mathbf{p}} - E_{p,B} \end{pmatrix}. \tag{4.2}$$

The Bogoliubov-de Gennes equations in superconducting systems are in electron-hole space, while here the equations consider only electrons. The Coulomb interaction is found by minimization of the dephasing term, $e^{i\delta q L}$, where δq is the momentum difference between the electron and hole term. This dephasing results in an energy dependent phase coherence length $\xi = \frac{\hbar v_T v_B}{C_1 + C_2}$. The factor $C_1 = (v_T + v_B)E$ is the consequence of condensation of particles with energy E above and below the chemical potential, similar to the cause of the superconducting coherence length. The additional factor $C_2 = (v_T - v_B)\mu + (v_B - v_T\frac{E_{pB}}{E_{pT}})E_{pT}$ is due to differences in Fermi velocity and energy between the two layers. The resulting Coulomb interaction is diagonal in spin space given by $\hat{M} = m\hat{I}$, and the excitons are formed by opposite charge carriers with opposite spin. The presence of primarily singlet excitons, important for entanglement measurements, is automatically satisfied by the topological insulator spin-momentum locking. From now on we take the realistic assumption of equal v_D in the exciton bottom and top layer, thereby maximizing the condensation energy. In the case when both layers have equal electron densities, the characteristic phase coherence length is maximized and can be written as $\xi = \hbar v_D/|m|$ (similar to the superconducting coherence length by substituting $|m|$ by Δ).

The eigenvalues corresponding to this system are given by

$$\begin{aligned} E_{k\alpha s} = \; & -\mu - \tfrac{1}{2}(E_{p,B} + E_{p,T}) \\ & +\alpha\sqrt{\left[v|k| + \tfrac{1}{2}s(E_{p,B} - E_{p,T})\right]^2 + |m|^2}. \end{aligned} \tag{4.3}$$

Here, $\alpha, s = \pm 1$. We will focus on the regime $\frac{1}{2}(E_{p,B} + E_{p,T}) + \mu \to 0$, where the condensation energy is maximized. In that case the Hamiltonian is equivalent to a topological insulator with a superconducting proximity effect [16].

4.3 Andreev reflection on the TI-TEC interface

We attach the *pn* topological insulator with Coulomb interaction to normal topological insulators electrodes described by Eq. 4.1. This setup is shown in Fig. 4.1. As Seradjeh *et.al* [1] pointed out, the condensation energy $|m|$ will vanish for a small Fermi energy difference $E_{p,T} - E_{p,B}$ and a large mean Fermi energy potential $\mu + \frac{1}{2}(E_{p,T} + E_{p,B})$. Consequently, we can neglect the Coulomb interaction in the *nn* configuration. We also neglect the Coulomb interaction for TI in the *pn* configuration when using low electron densities and large density mismatches. In the rigid boundary approximation this results in the following ansatz

$$\begin{aligned}
\Psi_T &= \begin{pmatrix} 1 \\ e^{i\theta_T} \\ 0 \\ 0 \end{pmatrix} e^{i\mathbf{k}_T\mathbf{r}} + r_1 \begin{pmatrix} 1 \\ -e^{-i\theta_T} \\ 0 \\ 0 \end{pmatrix} e^{-i\mathbf{k}_T\mathbf{r}} \\
\Psi_B &= r_2 \begin{pmatrix} 0 \\ 0 \\ 1 \\ e^{i\beta\theta_B} \end{pmatrix} e^{i\beta\mathbf{k}_B\mathbf{r}} \\
\Psi_C &= t_1 \begin{pmatrix} ue^{i\frac{\phi}{2}} \\ ue^{i(\frac{\phi}{2}+\theta_{CT})} \\ ve^{-i\frac{\phi}{2}} \\ ve^{i(-\frac{\phi}{2}+\theta_{CT})} \end{pmatrix} e^{i\mathbf{k}_{CT}\mathbf{r}} + t_2 \begin{pmatrix} ve^{i\frac{\phi}{2}} \\ -ve^{i(\frac{\phi}{2}-\theta_{CB})} \\ ue^{-i\frac{\phi}{2}} \\ -ue^{-i(\frac{\phi}{2}+\theta_{CB})} \end{pmatrix} e^{-i\mathbf{k}_{CB}\mathbf{r}}
\end{aligned} \tag{4.4}$$

Where, $\Psi_{T(B)}$ is the wave function in the top (bottom) surface, and C refers to the TEC. An incoming electron can reflect as an electron in the same layer (r_1), while changing its spin, given by $\binom{1}{e^{i\theta}}$, with θ the angle normal to the interface. The phase ϕ is an overall condensate phase which will be needed in the next section when we couple different exciton condensates. The angle θ_i of a scatter trajectory i is related to the incoming angle by Snell's law $\sin(\theta_i) = r_k \sin(\theta_{in})$, $r_k = \frac{k_{in}}{k_i}$. Andreev reflection (r_2) as an electron occurs by scattering in the other layer with opposite perpendicular momentum and same group velocity, when both electrodes are n-type. Therefore, Andreev reflection is specular (retro) when both electrodes are of similar (opposite) type, in contrast to normal metal superconductor contacts. Parallel momentum is conserved, resulting in $\beta = +(-)$ for retro (specular) reflection due to the different chirality between the p and n configuration. Therefore the spin of the Andreev reflected electron is dependent on whether the reflection is retro or specular. In the excitonic system, tuning from specular to retro is easily achieved by tuning the gate voltages, while in normal metal - superconductor contacts specular reflection is predicted only for specific cases [17].

Transmission is possible as an electron in either an electron-like branch with probability (t_1), or in a hole-like branch with probability (t_2). While direct tunneling is not taken explicitly in the model, it can influence the results. However,

electron hole exchange in the exciton condensate leaves the interface (the current) unaffected, and direct tunneling decays very rapidly. The decay length e^{-kL}, with $k \propto \Delta_{TI}$, is on the order of a few nm in typical topological insulators, where the bulk bandgap Δ_{TI} >100 meV. In fact, this difference between direct tunneling and Andreev reflection solves one of the problems in optimizing crossed Andreev reflection, where elastic cotunneling usually dominates.

For general parameters, u and v are found through the Hamiltonian, Eq. 4.2, together with demanding $\sum_i |\Psi_i|^2 = 1$. For equal Dirac velocities and carrier densities in the excitonic layer, the coherence factors u and v are given by $u = \sqrt{\frac{1}{2} + \frac{1}{2}\frac{\sqrt{E^2-|m|^2}}{E}}$ and $v = \sqrt{1-u^2}$. We solve the system by requiring Ψ to be continuous across the interface. We integrate the probability distribution over angles θ_{in} from 0 to π, considering a step-like interface along the direction $\hat{\mathbf{e}}_x$ normal to the interface. Figure 4.2 shows the angle averaged scatter probabilities for $r_k = \frac{\mu_{TI}}{\mu_{TEC}} = 0.1$ with the electrodes in the *nn* (a) and *pn* (b) configuration, which is representative of the general result for a large chemical potential mismatch, since $\theta_{t1,t2} \to 0$ for $r_k \to 0$. When the electrodes are in the *nn* configuration, Andreev reflection is specular and peaks at zero energy, similar to what is predicted for graphene[17]. Backscattering is forbidden on the edge of a 2D topological insulator, but small angle scattering is possible on the 2D surface of a 3D topological insulator, leaving a nonzero electron reflection. Still, the obtained Andreev reflection r_2 is significant, and will increase for smaller mismatches. Effectively, the interface has a high transparency for all chemical potential mismatches.

The current density in the electrodes in the $\hat{\mathbf{e}}_x$-direction, perpendicular to the interface, is obtained from $J_{x,T(B)} = \frac{1}{A}\sum_{\mathbf{k}} \mathbf{J}_{q,T(B)}(\mathbf{k})\hat{\mathbf{e}}_x f_{T(B)}(\mathbf{k})$. Here, A is the effective width, and the nonequilibrium distribution $f_{T(B)} = f_0(E - eV_T(V_B)) - f_0(E - eV_{ex,T(B)})$, with $f_0(E)$ the Fermi distribution function. Only trajectories below the critical angle $\theta_c(E) = \arcsin r_k^{-1}$ contribute to the current. The charge current is defined by $\mathbf{J}_{q,T(B)} = ev_{T(B)}[\Re(\psi_\uparrow\psi_\downarrow^*)\hat{\mathbf{e}}_x + \Im(\psi_\uparrow\psi_\downarrow^*)\hat{\mathbf{e}}_y]$. Bias voltages in the range $|eV| < |m|$ result in vanishing quasiparticle current in the TEC, and direct tunneling is negligible in this system. Therefore, in this regime, perfect entangled currents flow through both surfaces in opposite directions, see the lower panels of Fig. 4.2. The currents are entangled in energy, momentum and spin and form a promising source for solid state Bell experiments, quantum computation and quantum teleportation.

4.4 TEC-TI-TEC Josephson junctions

Now, we will consider two TECs connected by a topological insulator, as shown in Fig. 4.3a. The ansatz of the wave functions of the Bogoliubov-de Gennes equations in the topological insulator is: $\psi = a\psi_T^+ + b\psi_B^+ + c\psi_T^- + d\psi_B^-$, where superscript $\pm$ denotes forward and backward traveling waves. The bound states for this system are solved by assuming ψ to be continuous across both the left (L) and right (R)

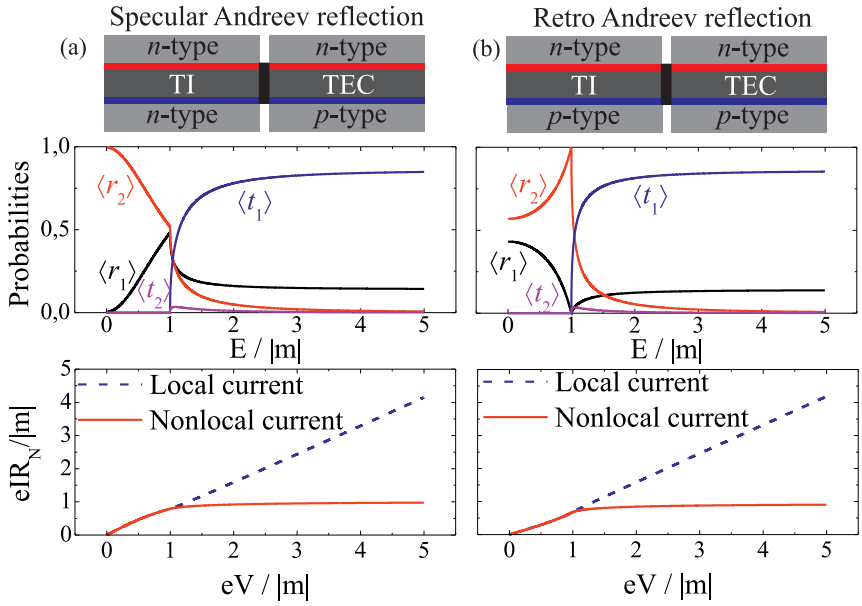

Figure 4.2: Tunneling coefficients and IV characteristics. The electrodes are in the nn **(a)** and pn **(b)** configuration with a mismatch $r_k = 0.1$. The Coulomb interaction in the electrode TI can be neglected. The top figures schematiccally describe the configuration. In the middle the probability distribution of the angle averaged scatter events are shown. Electrons with energy $E < M$ can only enter the exciton condensate by Andreev reflection, which is specular in the nn and retro in the pn configuration. The lower panels give the IV characteristics. The blue dashed line is the current through the same interface where the voltage is applied, the red solid line is the resulting current at the other interface. At $eV < |m|$ the current is perfectly entangled.

interfaces.

There are several ways to calculate the bound states; we follow the approach of Kulik[27]. The modes are calculated for energies $E < |m|$. The system is solved by connecting the left and right moving currents

$$\begin{aligned} c\psi_T^-(W,E) &= r_1^{T,R}(E)a\psi_T^+(W,E) + r_2^{B,R}(E)d\psi_B^-(W,E) \\ b\psi_B^+(W,E) &= r_2^{T,R}(E)a\psi_T^+(W,E) + r_1^{B,R}(E)d\psi_B^-(W,E) \\ a\psi_T^+(0,E) &= r_1^{T,L}(E)c\psi_T^-(0,E) + r_2^{B,L}(E)b\psi_B^+(0,E) \\ d\psi_B^-(0,E) &= r_2^{T,L}(E)c\psi_T^-(0,E) + r_1^{B,L}(E)b\psi_B^+(0,E). \end{aligned} \tag{4.5}$$

The coefficients r are determined by considering scattering at a single interface using the ansatz, Eq. (4). Figure 4.3b displays the boundstates for different incident angle θ_T. Scattering present at finite angles results in the opening of a gap. Unequal electron densities in the top and bottom layer shifts the gap from zero energy, resulting in a zero energy bound state for all angles, see Fig. 4.3c. This zero energy state appears at different ϕ for different incidence angle, and is not a Majorana fermion since $u^* \neq v$, since there is no electron hole symmetry between the top and bottom layer. The absence of backscattering for perpendicular incidence results in a zero energy state for any finite length. The bound state is a 4π periodic function for junction length $W \ll \xi$, $E_{T,B}(\phi) = \pm|m|\cos(\phi/2)$. From now on, we will consider this bound state.

The resulting current from perpendicular incidence is given by the derivative of the energy with respect to the phase: $I_{T,B} = \frac{\delta E_{T,B}}{\delta\phi} = \pm\frac{e}{2\hbar}|m|\sin(\phi/2)$. The relaxation to the lower energetic states resulting in $\sin(\phi)$ periodicity are determined by the competition between fermion parity and processes such as quasiparticle poisoning[23] and quantum phase slips[22]. TECs have also a degeneracy in layer, the electron and hole constituting the exciton can reside in the top and bottom layer or in the bottom and top layer, respectively. This degeneracy can cause relaxation but vanishes in the absence of direct tunneling. Therefore, in the absence of relaxation, currents quantized in the units of the fractional charge $e/2$ flow in opposite directions through both interfaces. Methods to detect the arising zero energy mode and the fractional charge are to measure ac and dc Josephson effects. Irradiating the device with microwaves will produce steps in the $I(V)$ characteristics at quantized voltages: $V = \frac{h}{q^*}f_{RF}$. In superconducting systems $q^* = 2e$, and this is reduced to $q^* = e$ with the appearance of Majorana fermions. In excitonic condensates $q^*_{T,B} = e$ and here it reduces to $q^*_{T,B} = \frac{e}{2}$ by the emergent zero energy mode. Recently, fluxoid quantization is predicted in bilayer exciton systems[24], quantized in $\Phi_0^* = \frac{h}{e}\gamma$, with γ the diamagnetic susceptibility. Here, the fractional charge $\frac{e}{2}$ would double the quantization resulting in $\Phi_0^* = 2\frac{h}{e}\gamma$, which can be osberved in SQUID devices[25], which will be discussed in Chapter 6.

The interesting question is if the zero energy mode is of Majorana fermion type. The Coulomb term $H_{\text{Coulomb}} = |m|[c^\dagger_{kT\uparrow}c_{-kB\downarrow} + c^\dagger_{-kT\downarrow}c_{kB\uparrow}] + h.c.$, with $c_i^\dagger$ the creation operator of a particle i. It is useful to change to a basis where spin is

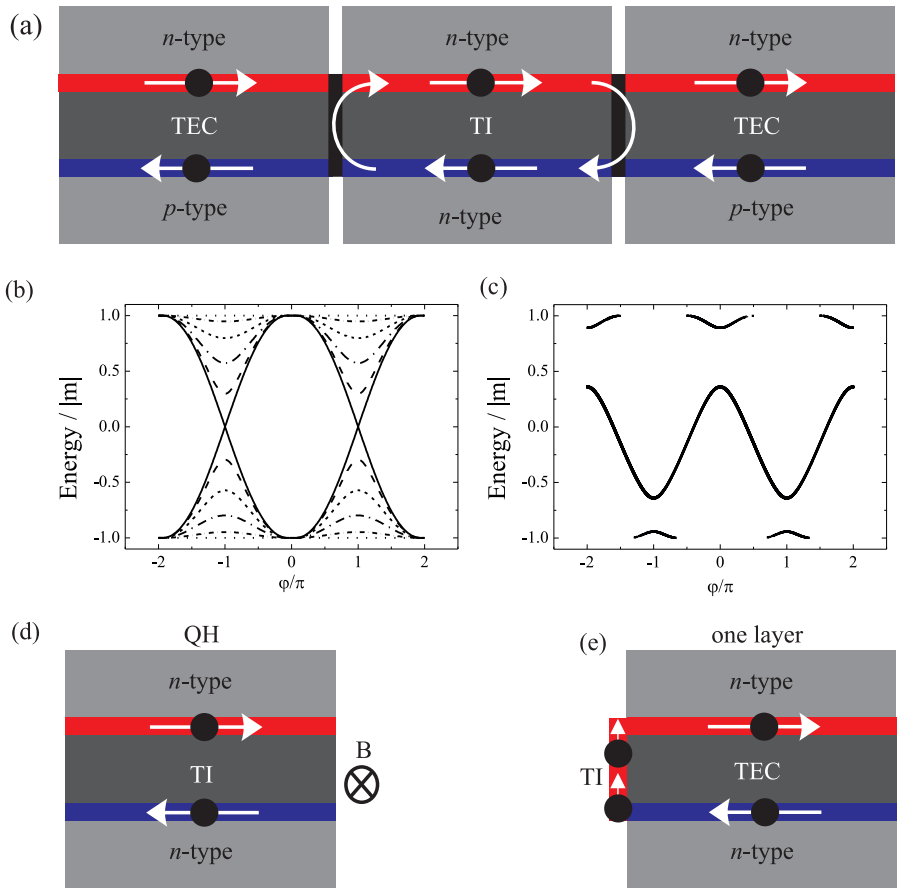

Figure 4.3: TEC Josephson junctions. The arrows indicate the direction of the momentum. **(a)** Device structure. **(b)** The boundstate for perpendicular incidence (solid line) is 4π periodic. Nonzero incidence angle results in the opening of a gap at finite length (here, $L = 0.1$ and $E_p = 50|m|$) and a momentum mismatch ($r_k = 0.1$), as shown for $\theta_T = 0.1$, 0.2, 0.3, 0.4 and 0.5π in dashed lines. **(c)** When the top and bottom TI layers have unequal Fermi densities, the gap shifts from zero energy, here $\frac{1}{2.6}E_{p,B} = E_{p,T} = 50|m|$, $W = 0.1$, $\theta_T = 0.2\pi$ and $r_k = 0.1$. The zero energy states become Majorana fermions by removing layer degeneracy, which occurs in the quantum Hall regime **(d)**, or by coupling the top and bottom layer **(e)**.

coupled to momentum $c_{k,1,\pm} = \frac{1}{\sqrt{2}}[c_{k,T\uparrow} \pm e^{-i\theta_k} c_{k,T\downarrow}]$ and $c_{k,2,\pm} = \frac{1}{\sqrt{2}}[c_{k,B\uparrow} \pm e^{-i\theta_k} c_{k,B\downarrow}]$. Cross terms consisting of both spin chiralities vanish due to the large energy difference between the different spin chiralities residing at the different sides of the Dirac cone. This energy difference is for the top (bottom) layer $2(\mu + E_{p,T(B)})$. Consequently, we can write $H_{\text{Coulomb}} = m(k)[c^\dagger_{k1+} c_{-k2+} - c^\dagger_{k1-} c_{-k2-}] + m^*(k)[c^\dagger_{-k1+} c_{k2+} - c^\dagger_{-k1-} c_{k2-}] + h.c.$, with a p-wave order parameter $m(k) = -\frac{1}{2}|m|e^{i\theta_k}$. The resulting Bogoliubov particles $\gamma = u c_{k1\pm} + v c^\dagger_{-k2\pm}$, are not Majorana since $[c_1, c_2]_- \neq 0$ because the operators work on different surfaces. The degeneracy of the surfaces, can be lifted in two ways, either by reducing it to one layer or by coupling the layers to the momentum (as is effectively done with the spin in a topological insulator).

Locking layer to momentum can be achieved by driving the system to the quantum Hall regime, shown in Fig. 4.3d. Applying a magnetic field creates a dispersion with all positive momentum states in the top layer and negative momentum states in the bottom layer, or vice versa. This regime is similar to a quantum Hall system, where Zeeman fields cause spin-splitted Landau levels, and the dispersionless bands results automatically in electron hole symmetry between the top and bottom layers even in the presence of different electron densities. In this regime, where current is flowing only perpendicular to the interface, we can change basis towards $c_{k1(2)\pm} = \frac{1}{\sqrt{2}}[c_{kT(B)\uparrow} \pm e^{-i\theta_k} c_{kB(T)\downarrow}]$, giving Bogoliubov particles: $\gamma = u c_{k1(2)\pm} + v c^\dagger_{-k1(2)\pm}$. These are unpaired Majorana fermions in the same reasoning as the Majorana fermions in superconductor - topological insulator junctions[12], but here the Majorana fermion is encoded over two surfaces. We note that bilayer exciton condensation is already actively studied in the quantum Hall regime[26].

Reducing the layer degeneracy is possible by coupling the top and bottom surfaces, shown in Fig. 4.3c. In that scenario the bound state is formed in a single layer, and a charge e flows between the two layers. An electron impinging on one surface results in Andreev reflection of a hole towards the opposite interface. For perpendicular incidence, this system has zero energy modes and a 4π periodic current phase relationship. The zero mode is an emergent Majorana fermion equivalent to the Majorana fermion in a superconductor - topological insulator - superconductor junctions[12], $\gamma = u c_k + v c^\dagger_{-k}$.

These Majorana fermions are localized to the interface and the decay length in the condensates is set by the excitonic coherence length ξ. Methods to detect the Majorana fermion can be based on the Majorana interferometers proposed for superconducting systems[28,29], where Majorana fermions also appear in two dimensional structures by the inclusion of ferromagnets. The realization of these devices depends on the quality of the topological insulator, the Fermi level positioned in the bulk bandgap is a prerequisite. Two dimensional topological insulators are already in the regime of very low bulk conductivity[30]. The strong effort to reduce bulk conduction in three dimensional topological insulators has already resulted

in high quality crystals[2,3], and in some systems the quantum Hall regime is already obtained[31]. Furthermore, a recent theoretical study predicted a critical condensation temperature up to 100K in the Bi_2Se_3 class of topological insulators[15]. This progress suggests that exciton condensation in topological insulators is within reach.

4.5 Conclusions

Inspired by the equivalence between a superconductor and a bilayer exciton condensate we have studied superconducting effects such as Andreev reflection and Josephson supercurrents in bilayer exciton systems. Topological bilayer exciton condensates offer new interesting opportunities such as the tunability of the individual layers and possible higher operation temperatures.

Bibliography

[1] B. Seradjeh, J.E. Moore, and M. Franz, Phys. Rev. Lett. **103**, 066402 (2009).

[2] Z.R. Ren, A.A. Taskin, S. Sasaki, K. Segawa, Y. Ando, Phys. Rev. B **84**, 165311 (2011).

[3] X. Jun, A.C. Petersen, D. Qu, Y.S. Hor, R.J. Cava, and N.P. Ong, Physica E **44**, 917 (2012).

[4] S.I. Shevchenko, Sov. J. Low Temp. Phys. **2**, 251 (1976).

[5] Y.E. Lozovik and A.V. Poushnov, Phys. Lett. A **228**, 399 (1997).

[6] J.M. Byers and M.E. Flatté, Phys. Rev. Lett. **74**, 306 (1995).

[7] G. Deutscher and D. Feinberg, Appl. Phys. Lett. **76**, 487 (2000).

[8] G. Falci, D. Feinberg, F.W.J. Hekking, Europhys. Lett. **54**, 255 (2001).

[9] L.G. Herrmann, F. Portier, P. Roche, A.L. Yeyati, T. Kontos, C. Strunk, Phys. Rev. Lett. **104**, 026801 (2010).

[10] L. Hofstetter, S. Csonka, J. Nygard, and C. Schönenberg, Nature **461**, 960 (2009).

[11] M. Veldhorst and A. Brinkman, Phys. Rev. Lett. **105**, 107002 (2010).

[12] L. Fu and C.L. Kane, Phys. Rev. Lett. **100**, 096407 (2008).

[13] B.A. Bernevig, T.L. Hughes, and S.C. Zhang, Science **314**, 1757 (2006).

[14] L. Fu, C.L. Kane, and E.J. Mele, Phys. Rev. Lett. **98**, 106803 (2007).

[15] Z. Wang, N. Hao, Z.G. Fu, P. Zhang, New J. Phys. **14**, 063010 (2012).

[16] Y. Tanaka, T. Yokoyama, and N. Nagaosa, Phys. Rev. Lett. **103**, 107002 (2009).

[17] C.W.J. Beenakker, Phys. Rev. Lett. **97**, 067007 (2006).

[18] D. Hsieh, D. Qian, L. Wray, Y. Xia, Y.S. Hor, R.J. Cava, and M.Z. Hasan, Nature **452**, 970 (2008).

[19] H. Zhang, C.X. Liu, X.L. Qi, X. Dai, Z. Fang, and S.C. Zhang, Nature Phys. **5**, 438 (2009).

[20] Y.L. Chen, J.G. Analytis, J.H. Chu, Z.K. Liu, S.K. Mo, X.L. Qi, H.J. Zhang, D.H. Lu, X. Dai, Z. Fang, S.C. Zhang, I.R. Fisher, Z. Hussain, and Z.X. Shen, Science **325**, 178 (2009).

[21] D. Hsieh, Y. Xia, D. Qian, L. Wray, J.H. Dil, F. Meier, J. Osterwalder, L. Patthey, J.G. Checkelsky, N.P. Ong, A.V. Fedorov, H. Lin, A. Bansil, D. Grauer, Y.S. Hor, R.J. Cava, and M.Z. Hasan, Nature **460**, 1101 (2008).

[22] B. van Heck, F. Hassler, A.R. Akhmerov, and C.W.J. Beenakker, Phys. Rev. B **84**, 180502 (2011).

[23] L. Fu and C.L. Kane, Phys. Rev. B **79**, 161408(R) (2009).

[24] L. Rademaker, J. Zaanen, and H. Hilgenkamp, Phys. Rev. B **83**, 012504 (2011).

[25] M. Veldhorst, C.G. Molenaar, C.J.M. Verwijs, H. Hilgenkamp, and A. Brinkman, Phys. Rev. B **86**, 024509 (2012).

[26] I.B. Spielman, J.P. Eisenstein, L.N. Pfeiffer, and K.W. West, Phys. Rev. Lett. **84**, 5808 (2000).

[27] I.O. Kulik, JETP **30**, 944 (1970).

[28] C.W.J. Beenakker, ArXiv:1112.1950v2 (2012).

[29] M.Z. Hasan and C.L. Kane, Rev. Mod. Phys, **82**, 3045 (2010).

[30] M. König, S. Wiedmann, C. Brüne, A. Roth, H. Buhmann, L.W. Molenkamp, X.L. Qi, and S.C. Zhang, Science **318**, 766 (2007).

[31] C. Brüne, C.X. Liu, E.G. Novik, E.M. Hankiewicz, H. Buhmann, Y.L. Chen, X.L. Qi, Z.X. Shen, S.C. Zhang, and L.W. Molenkamp, Phys. Rev. Lett. **106**, 126803 (2011).

Chapter 5 Josephson supercurrent through a topological insulator surface state

Abstract

The long-sought yet elusive Majorana fermion [1] is predicted to arise from a combination of a superconductor and a topological insulator [2–4]. An essential step in the hunt for this emergent particle is the unequivocal observation of supercurrent in a topological phase. Here, direct evidence for Josephson supercurrents in superconductor (Nb) - topological insulator (Bi_2Te_3) - superconductor e-beam fabricated junctions is provided by the observation of clear Shapiro steps under microwave irradiation, and a Fraunhofer-type dependence of the critical current on magnetic field. Shubnikov-de Haas oscillations in magnetic fields up to 30 T reveal a topologically non-trivial two-dimensional surface state. This surface state is attributed to mediate the ballistic Josephson current despite the fact that the normal state transport is dominated by diffusive bulk conductivity. The lateral Nb-Bi_2Te_3-Nb junctions hence provide prospects for the realization of devices supporting Majorana fermions [5].

5.1 Introduction

Topological insulators [6–16] are characterized by an insulating bulk with a finite band gap and conducting edge or surface states, where charge carriers are protected against backscattering. These states give rise to the quantum spin Hall effect [7] without an external magnetic field, where electrons with opposite spins have opposite momentum at a given edge. The surface energy spectrum of a three-dimensional topological insulator [8,10] is made up by an odd number of Dirac cones with the spin locked to the momentum. Almost simultaneous to the theoretical prediction of 3D topological insulator states in the bismuth compounds $Bi_{1-x}Sb_x$, Bi_2Se_3 and Bi_2Te_3 [6], angle-resolved photoelectron spectroscopy indeed revealed a linear dispersion and a helical structure of the Dirac cone at the surface of these compounds [9,12,13]. Soon after, the topological nature of the surface states was confirmed by transport studies such as Aharonov-Bohm oscillations in Bi_2Se_3 nanoribbons [14], Shubnikov-de-Haas oscillations in Bi_2Te_3 [17–19,21,22], scanning tunneling spectroscopy of the square-root magnetic field dependence of the Landau

level spacing[16] and interference effects resulting from impurity scattering[15]. Now the existence of the topological surface states has been established it is time to study the interaction with other materials. Efforts have been made to contact a topological insulator to a superconductor in the search for the Majorana fermion. First attempts[23,24] indicated the presence of a supercurrent through a topological insulator. In this Chapter we demonstrate that it is possible to induce a Josephson supercurrent in the surface state of the topological insulator Bi_2Te_3, as evidenced by the two hallmarks of the Josephson effect: a Fraunhofer-like magnetic field modulation of the critical current and the appearance of Shapiro steps upon microwave irradiation, resulting from the dc and ac Josephson effects, respectively.

5.2 Sample fabrication

We have fabricated polycrystalline Bi_2Te_3 samples with a common c-axis orientation using the Czochralski method as described elsewhere[25]. From these, flakes were produced by mechanical cleaving, proven to be a powerful tool for the fabrication of a few quintuple layer thin Bi_2Te_3 flakes[26]. Figure 5.1a shows an atomic force microscopy image of the surface of typical exfoliated Bi_2Te_3 flakes. We have performed experiments on large flakes with atomically flat terraces, extending over several micrometers. The Bi_2Te_3 quintuple layer step edges are clearly visible as shown in Fig. 5.1a. The exfoliated flakes have a thickness of 20 nm $-$ 2 µm, and sizes up to 50×50 µm^2. Van der Waals forces bind the flakes to the Si-substrate, enabling subsequent structuring. Sputter deposited Nb(200nm)/Pd(5nm) electrodes where defined by lift off techniques using optical photolithography with image reversal photoresist. The Pd layer prevents the Nb from oxidation and the thickness of the Nb being on the order of the flake thickness ensures a superconducting contact ($I_C > 30$ mA) between the Nb on the substrate and the flake. The Nb(70 nm) junctions where defined with lift off using e-beam and have a superconducting contact ($I_C > 30$ mA) with the Nb electrodes. To obtain transparent contacts, the Bi_2Te_3 surface is Ar sputter etched *in situ* prior to Nb deposition, while the Bi_2Te_3 in between the Nb forming the actual junction is unaffected due to the lift off technique. A scanning electron microscopy image of such a device is given in Fig. 5.1b.

5.3 High magnetic field measurements

To characterize the electronic properties of our devices and to track them down to the surface states of a topological insulator we have performed magnetotransport experiments on Bi_2Te_3 flakes in a Van der Pauw geometry in fields up to 30 T at the High Field Magnet Laboratory (Nijmegen) in a 33 T magnet. From the low field Hall coefficient $R_H = 7.5 \times 10^{-8}$ Ωm/T and the zero-field resistivity $\rho = 300$ µΩcm we deduce, using a one band model, a bulk conductivity channel with an n-type

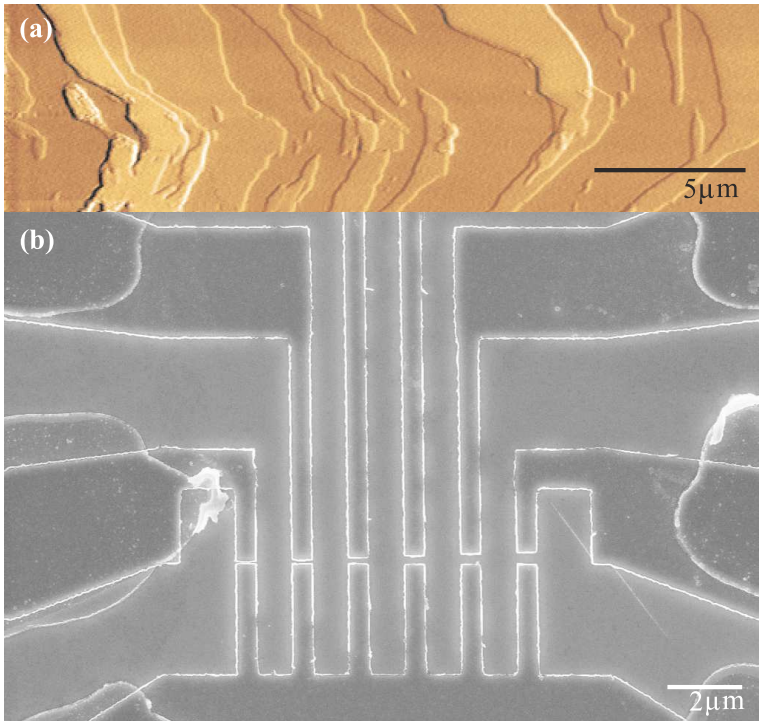

Figure 5.1: E-beam lithographically defined Nb electrodes on exfoliated Bi_2Te_3. (a) Atomic force microscopy image of an exfoliated Bi_2Te_3 surface. The step edges are 1.0 nm high, corresponding to the Bi_2Te_3 quintuple unit cell. These nanometer flat surfaces span an area up to 50×50 µm^2. **(b)** Scanning electron microscopy image of Nb-Bi_2Te_3-Nb Josephson junctions. The Nb superconductor strips are defined by e-beam lithography on a 200 nm thick exfoliated Bi_2Te_3 flake and connected to large Nb electrodes fabricated by photolithography. The junctions have a width of 500 nm and a length of (from left to right) 50, 100, 150, 200, 250 and 300 nm. A supercurrent has been identified at 1.6 K in all junctions up to 250 nm.

carrier concentration $n = 8.3 \times 10^{19}$ cm^{-3} and mobility μ=250 cm^2/Vs corresponding to an electron mean free path $l_e = 22$ nm for a parabolic band. This low mobility would not allow the observation of quantum oscillations since the necessary condition, $\mu B \gg 1$, is far from being fulfilled in the magnetic fields applied. As shown in Fig. 5.2a, we nevertheless observe clear Shubnikov-de Haas oscillations in the resistance implying another conduction channel with larger mobility. From the angle dependence of the position of the peaks we conclude that this additional channel is of two-dimensional nature, Fig. 5.2b.

In large magnetic fields the resistivity is not directly the inverse of the conductance, but follows from

$$\rho_{xx} = \frac{\sigma_{xx}}{\sigma_{xx}^2 + \sigma_{xy}^2}. \tag{5.1}$$

The oscillating part in σ_{xx} is smaller than the non-oscillating part in magnetic fields well below the quantum Hall regime. Furthermore, σ_{xx} is smaller than σ_{xy} by a factor $\mu B > 8$ in fields higher than 10 T, as will be shown below. Therefore, the longitudinal resistivity and conductance are in phase. This also leads to the interesting scenario that in the quantum Hall regime both the resistivity and the conductance can be zero at the same time. The oscillatory contribution to the resistance of a two-dimensional system in the regime when resistivity and conductance are in phase can than be written as [27]

$$R_{xx} \propto \frac{\lambda}{\sinh \lambda} e^{-\lambda_D} \cos\left(\frac{2\pi E_F}{\hbar\omega_c} + \pi + \varphi_B\right) \tag{5.2}$$

where, ω_c is the cyclotron frequency, E_F is the Fermi energy, $\lambda = 2\pi^2 k_B T/\hbar\omega_c$, $\lambda_D = 2\pi^2 k_B T_D/\hbar\omega_c$ with T_D the Dingle temperature, and φ_B is the Berry phase. When plotting the $1/B$-positions of the minima and maxima of R_{xx} (Fig. 5.2e) as a function of the Landau level index it already becomes clear that the corresponding $1/B$-positions do not extrapolate to $\varphi_B = 0$ as one would expect from an ordinary system, but is rather shifted by $\frac{1}{2}$ implying that $\varphi_B = \pi$, consistent with a half-filled zeroth Landau level that is present in a topological surface state [17–19,21,22,28], similar to graphene [29,30]. The conductance (and the resistivity which is in phase) has a maximum when the Fermi energy is in a Landau level and a minimum when it is in between two levels. Extrapolating the minimum should then intersect zero for a trivial system showing the absence of a zeroth order Landau level. In a topologically non-trivial system, all levels are shifted by π and the intersection is trough $-\frac{1}{2}$, which is clearly the case for the considered Bi_2Te_3 flakes. It is noted that, in principle, the conductivity and resistance can be out of phase while Shubnikov de Haas oscillations are present [20]. This can occur in a multiband system with a dominating conducting low mobillity band, together with a high mobillity band giving rise to the Shubnikov de Haas oscillations. If we project a multiband scenario on our system (two surfaces and one bulk), we find from the Hall coefficients a bulk mobillity of 1000 cm^2/Vs and bulk mean free paths

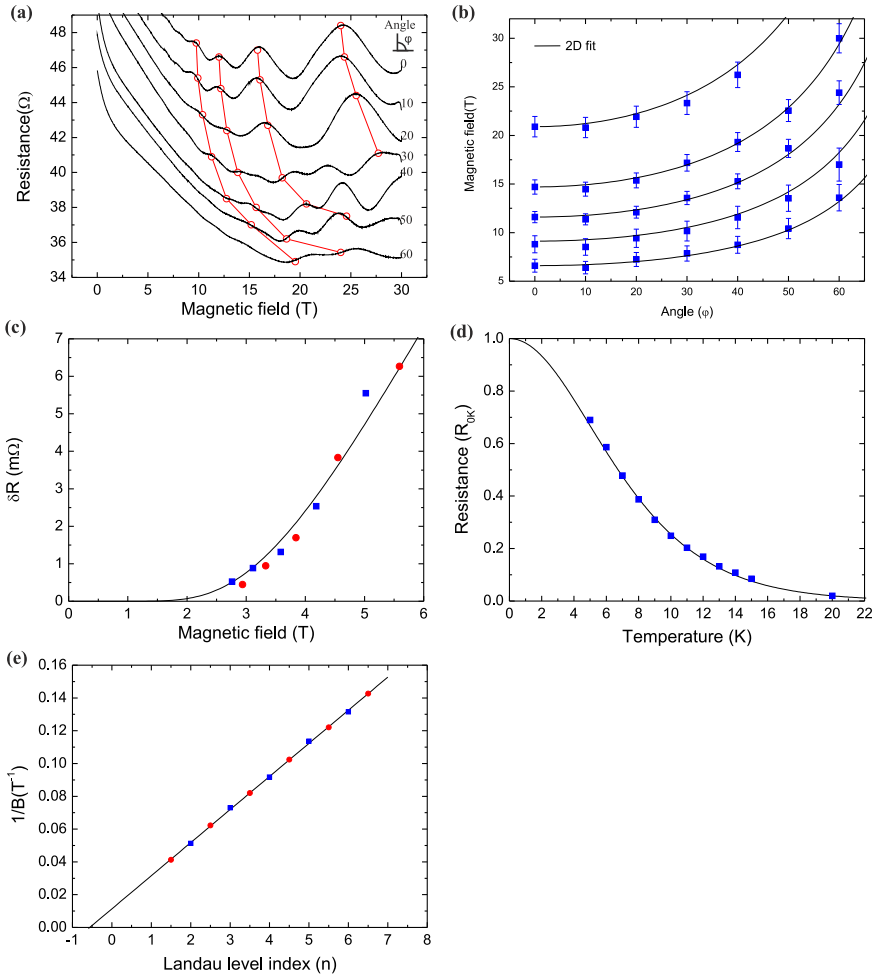

Figure 5.2: Magnetoresistance oscillations of the Bi_2Te_3 surface states. **(a)** Angle dependence of the Shubnikov-de Haas oscillations, at 4.2 K, (top to bottom: the angle between the magnetic field and the surface normal $\phi = 0°$ to 60° in steps of 10°) after linear background subtraction. The square markers represent the expected shift of the maxima in magnetic field for a two dimensional system, given by $B_\perp = B\cos(\phi)$, indicating that the oscillations arise from surface states. **b** The two dimensionality becomes evident from the angle dependence of the minima positions, obtained by taking the differential curve dR/dB. The error bars correspond to 25% of an oscillation. The data of **(c)** and **(d)** are obtained from the same sample in a different configuration, but different samples and geometries show the same results. **(c)** Oscillation amplitude dependence on the magnetic field (minima as squares and maxima as circles); linear backgrounds have been subtracted leaving the oscillating part. We deduce a Dingle temperature $T_D = 1.65$ K from fitting the increase in oscillation amplitude with increasing field. Only the magnetoresistance in small fields is considered, where the peak splitting is negligible. **(d)** Oscillation amplitude dependence on temperature; linear backgrounds have been subtracted. The effective mass $m^* = 0.16\ m_0$ is estimated by fitting the decrease of the magnetoresistance oscillations as function of temperature (peaks at least up to 9 T in both the conductance and resistance result in the same effective mass). **(e)** The $1/B$ values versus the Landau level index n intersect at $n = -0.5$, consistent with a half filled lowest Landau level as expected for a Dirac cone.

similar to the one band model, $l_e = 20 - 50$ nm depending on the effective mass. Using this mobillity we find that at least for fields higher than 10 T resistivity and conductivity are in phase, justifying the used method of assigning the Landau level positions. From the slope in Fig. 5.2d we infer the carrier concentration of the surface states of $n = 1.2 \times 10^{12}$ cm^{-2} per surface; an effective mass $m^* = 0.16\ m_0$ and a Dingle temperature of $T_D = 1.65$ K (corresponding to a mobility $\mu = 8300$ cm^2/Vs) follow from the temperature and field dependence of the Shubnikov-de Haas oscillations amplitudes (Figs. 5.2c and 5.2d). This results in a $v_F = 1.4 \times 10^5$ m/s with $l_e = 105$ nm.

In high magnetic fields two beating frequencies are present, as Xiong *et al.*[21] also observed in their study on the topological surface states of Bi_2Te_2Se. A double frequency has also been observed in the 3D topological insulator strained HgTe[28], where it was concluded to originate from the top and bottom topological surface states, with different carrier densities due to the difference in electrostatic environment (substrate and vacuum). As can be seen in Fig. 5.2a, the peak splitting becomes more pronounced with increasing parallel field, though it is already visible in the derivative of the magnetoresistance at smaller angles.

5.4 Nb-Bi_2Te_3-Nb Josephson supercurrent trough a topological insulator surface state

5.4.1 ac and dc Josephson effects

The superconducting Nb-Bi_2Te_3-Nb junctions, as depicted in Fig. 5.1b, show Shubnikov-de Haas oscillations at high magnetic fields with the same frequency, revealing the presence of topological surface states in these devices as well. The critical current of the Nb electrodes on top of the Bi_2Te_3 is larger than 30 mA for a strip of 500 nm width and 70 nm height. The junctions have a metallic temperature dependence, but upon cooling below 6.5 K, the resistance vanishes completely and a supercurrent is observed. Figure 5.3a shows a current-voltage characteristic at 1.6 K showing a clear supercurrent of $I_c = 18\ \mu$A. To test whether this is a true Josephson supercurrent we performed phase-sensitive experiments. Figure 5.3d and e shows the Fraunhofer pattern from the critical current dependence on the magnetic field due to the dc Josephson effect. Possible distinctions from the usual Fraunhofer pattern might result from extrinsic, geometrical effects like inhomogeneities, and the small ratio between the length and the width of the junction, changing the field dependence as predicted by[31]. Alternatively, unusual current phase relationships can cause deviations. The appearance of Majorana fermions results in a $\sin(\phi/2)$ current phase relationship. Inclusion of such terms yield doubled periodicities, and the presence of both terms cause smaller side lobes and non vanishing critical currents, as is interestingly the case in Fig 5.3d, and e. In Chapter 6 and 7, dc SQUIDs composed of these Josephson junctions are studied to discriminate between extrinsic and intrinsic effects. Due to the ac Josephson

effect, microwave irradiation should lead to Shapiro steps. Figure 5.3a shows the IV-curve upon 10.0 GHz microwave irradiation. Clear steps are observed at integer values of $V = h/2ef_{\mathrm{RF}} = 20.7$ µV. A colormap of the conductance dependence on the power and the current is shown in Fig. 5.3c, visualizing the evolution of the Shapiro steps. In Fig. 5.3b we have plotted the power dependence of the first three steps, following the expected Bessel function dependence.

5.4.2 Ballistic supercurrent through the surface state

Now that we have confirmed the Josephson nature of the devices, we can discuss in which band of the Bi_2Te_3 the proximity effect is induced. Figure 5.4 shows the temperature and length dependence of the critical current of the junctions. While the scaling with length can be described by diffusive as well as ballistic transport theory (see the section theoretical models for Josephson current below for more details), the temperature dependence of the junctions is clearly far from the diffusive limit and can only be fitted by the Eilenberger theory for ballistic junctions [32,33]. The bulk mean free path, $l_e = 22$ nm, is too small to explain the ballistic nature of the supercurrent in the junctions. However, the surface conduction band has a larger mean free path $l_e = 105$ nm. Noting that the mean free path obtained from Shubnikov-de Haas oscillations is usually an underestimate [34], we conclude that the ballistic Josephson supercurrent is carried by the topological surface states of Bi_2Te_3. As we discuss in more detail in the section theoretical models for Josephson current, the small I_cR_n product (reduced to about 2%) follows automaticaly from the large bulk shunt. The clean limit fit with $T_c = 6.5$ K gives a coherence length $\xi = \frac{\hbar v_F}{2\pi k_B T} = 75$ nm at 1.6 K, implying that $v_F = 1.0 \times 10^5$ m/s. This Fermi velocity is comparable to the value obtained from the magnetoresistance oscillations of the surface states (1.4×10^5 m/s).

5.5 Conclusions

The possibility of contacting many electrodes on the exfoliated Bi_2Te_3 flakes combined with the reproducibility as observed in the length dependence of the junctions creates an interesting basis for experimental investigations of the still increasing number of theoretical proposals on topological insulator - superconductor devices [2–4]. Interestingly, whereas bulk transport tends to obscure the observation of surface state transport in the normal state, the supercurrent is found to be carried mainly by the surface states. The realization of supercurrents through topological surface states is an important step towards the detection of Majorana fermions.

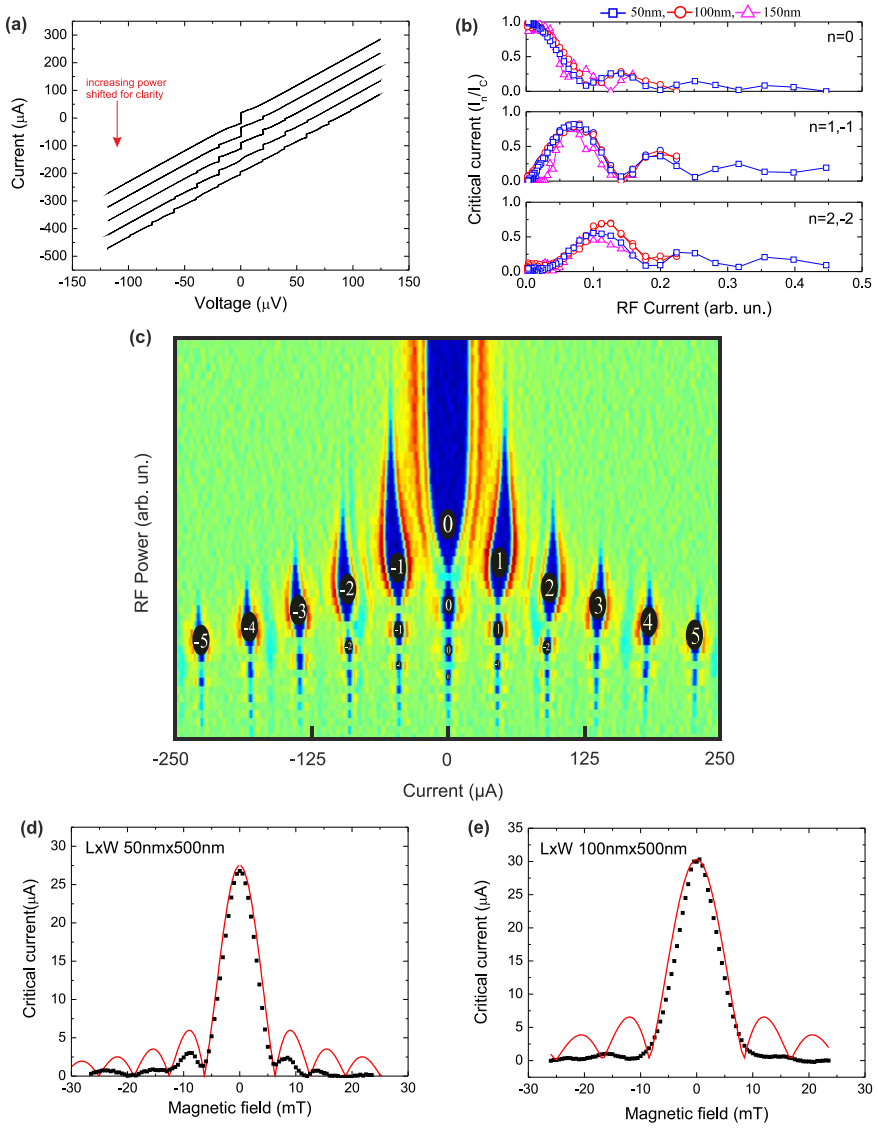

Figure 5.3: Josephson effects. **(a)** Current voltage characteristics of a Nb-Bi_2Te_3-Nb Josephson junction (length l=50 nm) on increased 10.0 Ghz RF irradiation power (curves are shifted for clarity). The temperature is 1.6 K. Clear Shapiro steps are observed at multiples of $V = \frac{h}{2e} f_{\mathrm{RF}} = 20.7$ μV. **(b)** Power dependence of the normalized critical current I_0 and the first two Shapiro steps I_n, with n=1,2. Shapiro steps are resolved in the junctions with length up to 150 nm. **(c)** Differential resistance, dV/dI, plotted on a color scale as a function of the bias current, I, and the microwave excitation power, P_{RF}. The numbers correspond to the nth order Shapiro step. **d** and **e**, Critical current dependence on the magnetic field fitted with $I_C = I_0 \left|\mathrm{sinc}\left(\frac{\pi\Phi}{\Phi_0}\right)\right|$, I_0 the critical current at zero field, Φ the flux and Φ_0 the flux quantum, for the 50nm junction, **(d)** and the 100nm junction, **(e)**. The temperature is 260 mK. Deviations from the standard Fraunhofer pattern are observed, opening an intriguing question whether this is the result of geometrical effects or unusual current phase relationships.

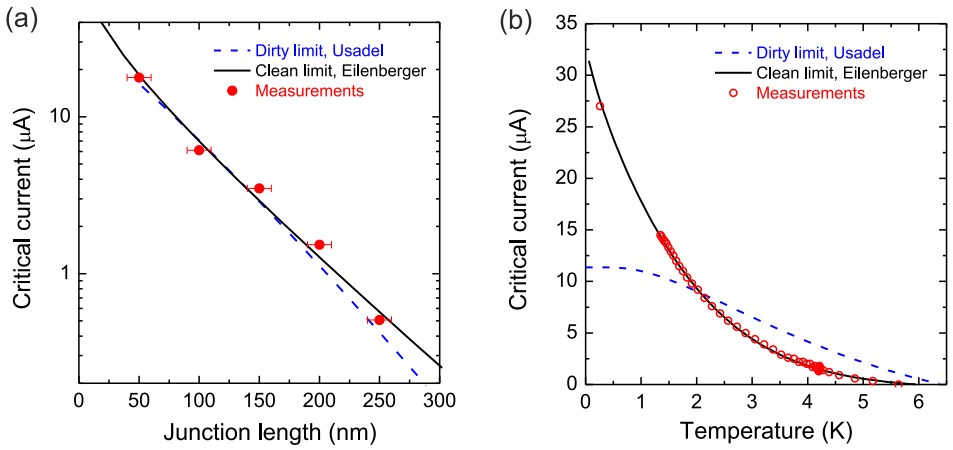

Figure 5.4: Temperature and length dependence of the critical current; demonstration of the ballistic nature of the junctions. **(a)** Scaling of the junction critical current with the electrode separation length at 1.6 K; error bars follow from ±10 nm e-beam resolution. **(b)** Temperature dependence of the critical current of the 50 nm junction. The measured data (red circles) can only be consistently fitted in both cases with Eilenberger theory for ballistic junctions (dashed black curves), while Usadel theory for diffusive junctions (dotted blue curves) cannot provide a good fit to the temperature dependence of the critical current. See the section theoretical models for Josephson current for details. The obtained clean limit coherence length $\xi = 75$ nm at 1.6 K.

5.6 Appendix: Theoretical models for Josephson current

Any hybrid structure containing superconductors can be described on the basis of the Gor'kov equations[35]. In practice, these equations are typically simplified by a quasi-classical approximation, which is justified as long as the Fermi-wavelength is much smaller than other length scales in the problem. For superconductor - normal metal - superconductor (SNS) Josephson junctions Eilenberger quasi-classical equations[36] are used when the elastic mean free path l_e is larger than the length L and the coherence length ξ. The electronic transport in this clean limit is ballistic across the N layer. In the dirty limit of $l_e \ll L, \xi$, transport is diffusive and the Usadel equations[37] are used. When the transparency between the S and N layers is not unity, additional insulating barriers (I) are typically included.

5.6.1 Eilenberger theory fit

The clean limit theory on the basis of the Gor'kov equations for short SINIS junctions with arbitrary barrier transparency D[32] was generalized[33,38] for arbitrary junction length on the basis of Eilenberger equations. The supercurrent density J

is found to be[33]

$$J = \frac{2}{\pi} e k_F^2 k_B T \sin\chi \sum_{\omega_n > 0} \int_0^1 \mu d\mu \frac{t_1(\mu) t_2(\mu)}{Q^{1/2}(\chi, \mu)}, \tag{5.3}$$

where $\mu = k_x/k_F$, $t_{1,2} = D_{1,2}/(2 - D_{1,2})$, and

$$\begin{aligned} Q = \quad & \Big[t_1 t_2 \cos\chi + \left(1 + (t_1 t_2 + 1) \frac{\omega_n^2}{\Delta^2}\right) \cosh\frac{2\omega_n L}{\mu\hbar v_F} + \\ & (t_1 + t_2) \frac{\omega_n \Omega_n}{\Delta^2} \sinh\frac{2\omega_n L}{\mu\hbar v_F}^2 - \left(1 - t_1^2\right)\left(1 - t_2^2\right) \frac{\Omega_n^4}{\Delta^4}, \end{aligned} \tag{5.4}$$

where the Matsubara frequency is given by $\omega_n = 2\pi k_B T(2n + 1)$, and $\Omega_n = \sqrt{\omega_n^2 + \Delta^2}$. Δ is the gap in the S electrodes, χ the phase difference across the junction, while v_F is the Fermi velocity of the normal metal interlayer. The integral runs over all trajectory directions and can be adjusted to actual junction geometries.

Eq. (5.3) was evaluated as function of junction length and fitted to the measured critical current density. Since the prefactors in Eq. (5.3) implicitly contain the normal state resistance, which is not known for our junctions due to the bulk shunt, we left the overall scale of J free in the fit. Subsequently, the best fit to the data at 1.6 K was obtained for $\xi = \frac{\hbar v_F}{2\pi k_B T} = 75$ nm. It was found numerically that the value of the barrier transparencies in the symmetric case had no influence on the fitting value for ξ.

The temperature dependence of the critical current was calculated using Eq. (5.3) and the obtained coherence length. The fit to the measured data is excellent, considering that only the overall scale of J was free in this case.

In fact, the overall scaling factor of the critical current in Eq. (1) can be estimated as well. The transparency of the interfaces between the topological insulator and the superconductor are important in this respect. The high transparency of our interfaces can be determined from the $I(V)$ characteristic. The excess current in the $I(V)$ characteristic is about 67 % of the critical current I_c. In the Blonder-Tinkham-Klapwijk model[41], this gives a barrier strength of about $Z = 0.6$. For these high transparencies, at the lowest temperatures and for the 50 nm junction, Eq. (1) provides an $I_c R_N$ product of the order of 1-2 mV. However the 3D bulk shunt will strongly reduce this value by decreasing R_n. From the Shubnikov de Haas oscillations we can estimate the surface to bulk resistance ratio. The surface resistance can be found through $R_{SDH} = R_c R_t R_d$. With $R_t R_D = 0.77$ at 17.6 T and an oscillation amplitude $R_{SDH} = 1.8\Omega$ we can estimate the nonoscillating contribution $R_c = 2.3\Omega$. This is approximately 2 % of the total resistance (126Ω) at 17.6 T; the surface resistance contributes about 2 % to the total resistance. Thus, the estimated surface resistance of the superconducting Josephson junctions are approximately 29 Ω, which together with $I_c = 32$ µA (the critical current for the 50nm junction extrapolated to 0 K) results in $I_c R_N = 1$ mV, agreeing with the Eilenberger model. This agreement between model and measurements underlines the conclusion that supercurrent is flowing through the ballistic channels of the

topological surfaces states, shunted by a normal state bulk conduction. Small quantitative differences in prefactors can be expected when including the TI in the junction model, such as an observed prefactor of 2 in Ref. [42].

5.6.2 Usadel theory fit

The Usadel equation [37] for the S and N layers in a diffusive SNS junction can be written as

$$\Phi_{S,N} = \Delta_{S,N} + \xi_{S,N}^2 \frac{\pi k_B T_c}{\omega_n G_{S,N}} \frac{d}{dx}\left(G_{S,N}^2 \frac{d}{dx}\Phi_{S,N}\right), \tag{5.5}$$

where Φ is defined in terms of the normal Green's function G and the anomalous Green's function F by $\Phi G = \omega_n F$. The normalization condition $FF^* + G^2 = 1$ then gives

$$G_{S,N} = \frac{\omega_n}{\sqrt{\omega_n^2 + \Phi_{S,N}\Phi_{S,N}^*}} \tag{5.6}$$

The coherence length is given by $\xi = \sqrt{\frac{\hbar D}{2\pi k_B T}}$ where $D = v_F l_e/3$ is the diffusion constant.

The pair potentials $\Delta_{S,N}$ are given by

$$\Delta_{S,N} \ln\frac{T}{T_{cS,N}} + 2\pi k_B T \sum_{\omega_n>0} \frac{\Delta_{S,N} - \Phi_{S,N} G_{S,N}}{\omega_n} = 0 \tag{5.7}$$

In the dirty limit, Zaitsev's effective boundary conditions for quasi-classical Green's functions were simplified by Kupriyanov and Lukichev [40]. When Φ and G are found using these boundary conditions, finally the supercurrent density can be obtained from

$$J = \frac{2\pi k_B T}{e\rho_N} \mathrm{Im} \sum_{\omega_n>0} \frac{G_N^2}{\omega_n^2} \Phi_N \frac{d}{dx}\Phi_N, \tag{5.8}$$

where ρ_N is the N layer resistivity.

For junctions with arbitrary length and arbitrary barrier transparency, no analytical expressions exist for the Green's functions. Therefore a numerical code was used to fit the data. In the effective boundary conditions [40], two parameters play a role, $\gamma = \frac{\rho_S \xi_S}{\rho_N \xi_N}$ and $\gamma_B = \frac{2l_e}{3\xi_N}\left\langle\frac{1-D}{D}\right\rangle$, where the average of the transparencies takes place over all trajectory angles. For Nb as S electrode and Bi_2Te_3 as N interlayer, $\gamma \ll 1$ because of the lower resistivity ρ of Nb as compared to Bi_2Te_3. The junctions transparency is not known a priori, but from the voltage drop over a barrier in the normal state, as well as the large amount of excess current (more than 50% of the critical current) in the current-voltage characteristics of the superconducting state, a conservative estimate gives $D \gtrsim 0.5$, which implies $\gamma_B \lesssim 1$. Within this parameter range (or even outside the range) no consistent fit could be made to the data. Figure 6a shows the fit to the temperature dependence of the critical current for $\gamma = 0.1$, $\gamma_B = 1$ and $\xi(T_c) = \sqrt{\frac{\hbar D}{2\pi k_B T_c}} = 21$ nm, the latter value as obtained from fitting the length dependence of the junction.

Bibliography

[1] E. Majorana Nuovo Cimento **14**, 171 (1937).

[2] L. Fu, C.L. Kane, and E.J. Mele, Phys. Rev. Lett. **100**, 096407 (2008).

[3] J. Nilsson, A.R. Akhmerov, and C.W.J. Beenakker, Phys. Rev. Lett. **101**, 120403 (2008).

[4] Y. Tanaka, T. Yokoyama, and N. Nagaosa, Phys. Rev. Lett. **103**, 107002 (2009).

[5] M.Z. Hasan and C.L. Kane, Rev. Mod. Phys. **82**, 3045 (2010).

[6] B.A. Bernevig, T.L. Hughes, and S.C. Zhang, Science **314**, 1757-1761 (2006).

[7] M. König, S. Wiedmann, C. Brüne, A. Roth, H. Buhmann, L.W. Molenkamp, X.L. Qi, and S.C. Zhang, Science **318**, 766 (2007).

[8] L. Fu, C.L. Kane, and E.J. Mele, Phys. Rev. Lett. **98**, 106803 (2007).

[9] D. Hsieh, D. Qian, L. Wray, Y. Xia, Y.S. Hor, R.J. Cava, and M.Z. Hasan, Nature **452**, 970 (2008).

[10] H. Zhang, C.X. Liu, X.L. Qi, X. Dai, Z. Fang, and S.C. Zhang, Nature Phys. **5**, 438 (2009).

[11] X.L. Qi, L. Rundong, J. Zang, and S.C. Zhang, Science **323**, 1184 (2009).

[12] Y.L. Chen, J.G. Analytis, J.H. Chu, Z.K. Liu, S.K. Mo, X.L. Qi, H.J. Zhang, D.H. Lu, X. Dai, Z. Fang, S.C. Zhang, I.R. Fisher, Z. Hussain, and Z.X. Shen, Science **325**, 178 (2009).

[13] D. Hsieh, Y. Xia, D. Qian, L. Wray, J.H. Dil, F. Meier, J. Osterwalder, L. Patthey, J.G. Checkelsky, N.P. Ong, A.V. Fedorov, H. Lin, A. Bansil, D. Grauer, Y.S. Hor, R.J. Cava, and M.Z. Hasan, Nature **460**, 1101 (2008).

[14] H. Peng, K. Lai, D. Kong, S. Meister, Y. Chen, X.L. Qi, S.C. Zhang, Z.X. Shen, and Y. Cui, Nature Mat. **9**, 225 (2010).

[15] T. Zhang, P. Cheng, X. Chen, J.F. Jia, X. Ma, K. He, L. Wang, H. Zhang, X. Dai, Z. Fang, X. Xie, and Q.K. Xue, Phys. Rev. Lett. **103**, 266803 (2009).

[16] P. Cheng, C. Song, T. Zhang, Y. Zhang, Y. Wang, J.F. Jia, J. Wang, Y. Wang, B.F. Zhu, X. Chen, X. Ma, K. He, L. Wang, X. Dai, Z. Fang, X. Xie, X.L. Qi, C.X. Liu, S.C. Zhang, and Q.K. Xue, Phys. Rev. Lett. **105**, 076801 (2010).

[17] D.X. Qu, Y.S. Hor, J. Xiong, R.J. Cava, and N.P. Ong, Science **329**, 821 (2010).

[18] F. Xiu, L. He, Y. Wang, L. Cheng, L.T. Chang, M. Lang, G. Huang, X. Kou, Y. Zhou, X. Jiang, Z. Chen, J. Zou, A. Shailos, and K.L. Wang, Nature Nano. **6**, 216 (2011).

[19] J.G. Analytis, R.D. McDonald, S.C. Riggs, J.H. Chu, G.S. Boebinger, and I.R. Fisher, Nature Phys. **6**, 960 (2010).

[20] J. Xiong, Y. Luo, Y.H. Khoo, S. Jia, R.J. Cava, and N.P. Ong, Phys. Rev. B **86**, 045314 (2012).

[21] J. Xiong, A.C. Petersen, D. Qu, R.J. Cava, and N.P. Ong, Physica E **44**, 914 (2012).

[22] A.A. Taskin, Z. Ren, S. Sasaki, K. Segawa, and Y. Ando, Y., Phys. Rev. Lett. **107**, 016801 (2011).

[23] D. Zhang, J. Wang, A.M. DaSilva, J.S. Lee, H.R. Gutierrez, M.H.W. Chan, J. Jain, N. Samarth, Phys. Rev. B **84**, 165120 (2011).

[24] B. Sacépé, J.B. Oostinga, J. Li, A. Ubaldini, N.J.G. Couto, E. Giannini, and A.F. Morpurgo, Nature Comm. **2**, 575 (2011).

[25] A.H. Li, M. Shahbazi, S.H. Zhou, G.X. Wang, C. Zhang, P. Jood, G. Peleckis, Y. Du. Z.X. Cheng, X.L. Wang, and Y.K. Kuo, Thin Sol. Films **518**, 57 (2010).

[26] D. Teweldebrhan, V. Goyal, M. Rahman, and A.A. Balandin, Appl. Phys. Lett. **96**, 053107 (2010).

[27] I.M. Lifshitz and A.M. Kosevich, Sov. Phys. JETP **2**, 636 (1956).

[28] C. Brüne *et al.* C.X. Liu, E.G. Novik, E.M. Hankiewicz, H. Buhmann, Y.L. Chen, X.L. Qi, Z.X. Shen, S.C. Zhang, and L.W. Molenkamp, Phys. Rev. Lett. **106**, 126803 (2011).

[29] K.S. Novoselov, A.K. Geim, S.V. Morozov, D. Jiang, M.I. Katsnelson, I.V. Grigorieva, S.V. Dubonos, and A.A. Firsov, Nature **438**, 197 (2005).

[30] Y. Zhang, Y.W. Tan, H.L. Stormer, and P. Kim, Nature **438**, 201 (2005).

[31] V. Barzykin and A.M. Zagoskin, Superlat. and Microstruct. **25**, 797 (1999).

[32] A. Brinkman and A.A. Golubov, Phys. Rev. B **61**, 11297 (2000).

[33] A.V. Galaktionov and A.D. Zaikin, Phys. Rev. B **65**, 184507 (2002).

[34] T. Dietl, J. Phys. Colloques **39**, 1081 (1978).

[35] L.P. Gor'kov, Zh. Eksp. Teor. Fiz. **34**, 735 (1958) [Sov. Phys. JETP **7**, 505 (1958)].

[36] G. Eilenberger, Z. Phys. **214**, 195 (1968).

[37] K.D. Usadel, Phys. Rev. Lett. **25**, 507 (1970).

[38] F.S. Bergeret, A.F. Volkov, and K.B. Efetov, Phys. Rev. B **64**, 134506 (2001).

[39] A.V. Zaitsev, Zh. Eksp. Teor. Fiz. **86**, 1742 (1984) [Sov. Phys. JETP **59**, 1015 (1984)]

[40] M. Yu. Kupriyanov and V.F. Lukichev, Zh. Eksp. Teor. Fiz. **94**, 139 (1988) [Sov. Phys. JETP **67**, 1163 (1988)]

[41] G.E. Blonder, M. Tinkham, and T.M. Klapwijk, T.M., Phys. Rev. B **25**, 4515 (1982).

[42] D.M. Badiane, M. Houzet, and J.S. Meyer, Phys. Rev. Lett. **107**, 177002 (2011).

Chapter 6 Optimizing the Majorana character of SQUIDs with topologically non-trivial barriers

Abstract

We have modeled SQUIDs with topologically non-trivial superconducting junctions and performed an optimization study on the Majorana fermion detection. We find that the SQUID parameters β_L, and β_C can be used to increase the ratio of Majorana tunneling to standard Cooper pair tunneling by more than two orders of magnitude. Most importantly, we show that dc SQUIDs including topologically trivial components can still host strong signatures of the Majorana fermion. This paves the way towards the experimental verification of the theoretically predicted Majorana fermion.

6.1 Introduction

Superconducting junctions with topologically non-trivial barriers are predicted to host Majorana bound states[1,2]. Non-trivial states include the edge or surface of the recently discovered topological insulators[3–12] and semiconducting nanowires in the presence of Rashba spin orbit coupling and a Zeeman field[13,14]. Candidates with high potential for the detection and manipulation of the Majorana fermion[15] are superconducting quantum interference devices (SQUIDs)[16,17]. The appearance of Majorana bound states in superconducting junctions enables tunneling of quasiparticles with charge e across the junction, which doubles the Josephson periodicity, $I_c = I_0 \sin(\phi/2)$[1]. The doubled periodicity is predicted to lead to the absence of odd integer Shapiro steps in individual junctions, and a SQUID modulation period of $2\Phi_0$ instead of the usual Φ_0 periodicity, with $\Phi_0 = \frac{h}{2e}$ the magnetic flux quantum in superconductivity[16–18].

Experimental efforts have been made to contact superconductors to topologically non-trivial states, which resulted in gate tunable supercurrents and the observation of dc and ac Josephson effects[19–21]; see also Chapter 5 of this thesis. Josephson effects have been observed, and SQUIDs have been reported[22], which will be discussed in Chapter 7. The first signatures of a Majorana fermion, characterized by a zero bias conductance peak, have been observed in superconductor -

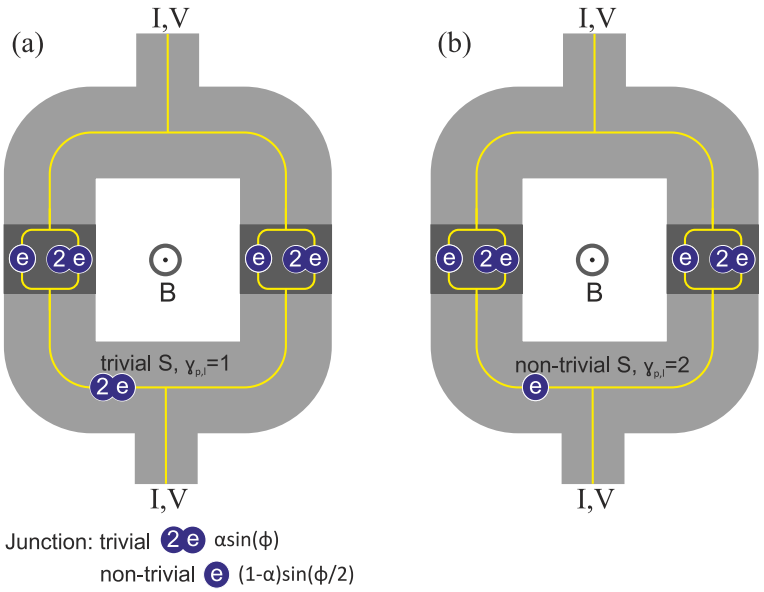

Figure 6.1: Schematic representation of the considered dc SQUID. The considered dc SQUID is composed of a superconducting ring interrupted by two Josephson junctions. Charge transport through the Josephson junction is characterized by standard Cooper pair tunneling ($\sin(\phi)$) and single electron tunneling by virtue of the Majorana fermion ($\sin(\phi/2)$). The relative contribution of these two processes is determined by the factor α. We analyze two scenarios, in **(a)** the superconductor is macroscopic and is in the trivial state, $\gamma_{pl} = 1$ and in (b) the superconductor is in the topologically non-trivial state, $\gamma_{pl} = 2$. Doubled periodicity is only observed when there is a topologically non-trivial state in the entire ring, as in **(b)**. However, the unusual current phase relation changes the dc SQUID characteristics even when the ring is not entirely topologically non-trivial.

semiconducting nanowire junctions[23]. Nonetheless, so far only Φ_0 periodic dependences have been observed. Relaxation to equilibrium states[16,18], quantum phase slips[17], high electron densities, and the large bulk shunt present in contacts with topological insulators so far, may reduce the $2\Phi_0$ periodicity.

A key question therefore is how to optimize the Majorana character. In this Chapter, we study extrinsic parameters that can be controlled to optimize the $\sin(\phi/2)$ signal from the Majorana fermion in dc SQUIDs composed of junctions containing both $\sin(\phi)$ and $\sin(\phi/2)$ components in different proportions. Our main observation is that the SQUID parameters β_L and β_C are important parameters altering the periodicity. Furthermore, a superconducting interferometer will have the periodicity of the component with the smallest periodicity. Nonetheless, even in dc SQUIDs with topologically trivial components the Majorana character strongly influences the dc SQUID characteristics. This study is also of relevance for dc SQUIDs composed of junctions with higher order periodicities, occurring in SNS and SFS systems[24].

6.2 Model

In the next session we introduce fluxoid quantization in superconducting rings composed of topologically trivial and non-trivial parts. Then we will use the fluxoid quantization to determine the critical current in the SQUID under applied magnetic fields and derive the voltage state assuming that the junctions can be described with the resistively and capacitively shunted junction model.

6.2.1 Fluxoid quantization in topologically (non)-trivial rings

The fluxoid quantization in a superconducting loop Γ leads to $\gamma_{pl}\Phi_0$ periodicity, with γ_{pl} related to the charge carrier $q = \frac{2e}{\gamma_{pl}}$ in the loop. In macroscopic systems, $\gamma_{pl} = 1$, but for mesoscopic systems on the order of the superconducting coherence length ξ[25,26] and systems including Majorana fermions, γ_{pl} can be either 1 or 2 depending on parity conservation[27]. Integrating the phase of a superconducting loop containing N Josephson junctions results in:

$$\oint \frac{\phi}{\gamma_{pl}} \cdot d\mathbf{l} = -\frac{2\pi}{\gamma_{pl}\Phi_0} \int_{\Gamma'} \Lambda \mathbf{J}_s \cdot d\mathbf{l} - \frac{2\pi}{\gamma_{pl}\Phi_0} \oint \mathbf{A} \cdot d\mathbf{l} - \sum_{i=1}^{N} \frac{\phi_i}{\gamma_{pj}}$$

Here, Γ' denotes the contour of the superconducting ring with the Josephson junctions excluded, and Λ is a normalization constant for the current. The phase-drop over junction i is given by $\frac{\phi_i}{\gamma_{pj}}$, with γ_{pj} connected to the charge carrier $q = \frac{2e}{\gamma_{pj}}$ in the junction. We will consider scenarios where the superconductor is either trivial $\gamma_{pl} = 1$ or topologically non-trivial $\gamma_{pl} = 2$. Also we will consider the junctions to be trivial $\gamma_{pj} = 1$, topologically non-trivial $\gamma_{pj} = 2$ or that both charge carrier types are present in the junctions. When the junctions are topologically non-trivial, but the superconductor is macroscopic, quantum phase slips can occur in the superconductor so that γ_{pl} can be different from γ_{pj}. Contour integration over the magnetic vector potential $\mathbf{A}$ results in the total flux Φ. Then, in the limit $\mathbf{J}_s = 0$, assuming thick superconducting leads, fluxoid quantization reduces to: $\frac{1}{2\pi}\sum_{i=1}^{N} \frac{\phi_i}{\gamma_{pj}} + \frac{\Phi}{\gamma_{pl}\Phi_0} = n$. The flux Φ is the sum of the external flux and the self-flux induced by current flowing through the ring.

Now we will consider the case of a ring containing two junctions, as depicted in Fig. 7.1. We consider the dc SQUID to be symmetric, except for the current phase relationship of the individual junctions. Inclusion of asymmetry (e.g. inductance, critical current or capacitance asymmetry) is easily included. However, inclusion will only lead to asymmetrical SQUID characteristics, and will not change the periodicity. The total flux of the considered system is given by $\Phi = \Phi_e + LI_c\chi_1 - LI_c\chi_2$. Here, Φ_e is the externally applied flux, L the inductance of a single arm and I_c the critical current of the individual junctions 1 and 2, $I_c = I_{c1} = I_{c2}$. The factors $\chi_{1,2}$ denote the current dependence on the phase difference of the individual junctions, which we limit to $\chi\chi_0^{-1} = \alpha\sin(\phi) + (1-\alpha)\sin(\phi/2)$, with $\alpha \in [0,1]$ the relative

amplitude and χ_0 a normalization factor to have $\max(\chi) = 1$. The $\sin(\phi)$ component is the standard Josephson relation, and SNS-junctions are well described by this sinusoidal relation, but it can include higher order components due to n Cooper pairs tunneling[24], described by $I_s(\phi) = \sum_{n=1}^{\infty} I_c^n \sin(n\phi_n)$. Our simplification includes the lowest frequency, which is enough for our conclusions. The $\sin(\phi/2)$ component is due to single electron tunneling by virtue of the Majorana fermion resulting in the 4π current phase relationship periodicity.

6.2.2 SQUID characteristics in the superconducting and voltage state

The critical current for an applied external field is obtained by finding the solution of the fluxoid quantization equation with the maximal critical current. The junctions in the voltage state are modeled with the resistively and capacitively shunted junction (RCSJ) model, assuming an ideal Josephson junction shunted by a resistor R and a capacitor C: $I = C\frac{dV}{dt} + I_c\chi_{1,2} + \frac{V}{R}$. The voltage is related to the time derivative of the phase by $V = \frac{\Phi_0}{2\pi}\frac{d\phi}{dt}$, the same for a topologically trivial and non-trivial ring since we have written the phase as $\frac{\phi}{\gamma_{pj1,2}}$. The RCSJ model leads to the expression $\frac{d^2\phi}{dt^2} + \frac{1}{RC}\frac{d\phi}{dt} + w_p^2(\chi_{1,2} - \frac{I}{I_c}) = 0$, with the plasma frequency $w_p = \sqrt{\frac{2\pi}{\Phi_0}\frac{I_c}{C}}$. The SQUID parameters are defined as

$$\begin{aligned} \beta_L &= \frac{2\pi L I_c}{\Phi_0}, \\ \beta_C &= \frac{2\pi}{\Phi_0} I_c R^2 C. \end{aligned}$$

Applying the fluxoid quantization equation, the voltage state can be described by the two differential equations which we have solved numerically

$$\beta_C \frac{d^2\phi_{2,1}}{dt^2} + \frac{d\phi_{2,1}}{dt} + \chi_{2,1} - \frac{1}{2}\frac{I}{I_c} \pm \beta_L^{-1}(\phi_2 - \phi_1 - 2\pi\frac{\Phi_e}{\Phi_0}) = 0.$$

6.3 Results

In this section we show the SQUID characteristics. We will start analyzing a dc SQUID composed of a topologically trivial ring, and two non-trivial junctions. In this regime there is no doubled fluxoid quantization, however the unusual current phase relationship causes a deviation from standard SQUID characteristics. After that, we will consider the SQUID in the entirely non-trivial regime, where doubled periodicity is observed due to the appearance of the Majorana fermion. Finally, we move to the voltage state and consider both cases in this regime.

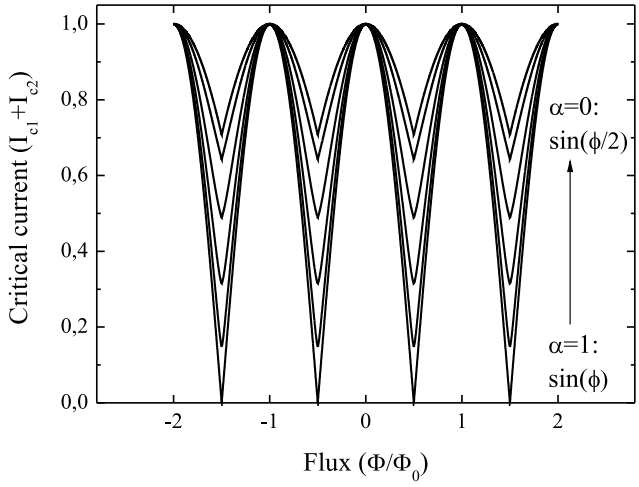

Figure 6.2: IΦ characteristics of a dc SQUID composed of a topologically trivial superconducting ring and non-trivial junctions. The current phase relationship of the junctions is shown for $\alpha \sin(\phi) + (1-\alpha)\sin(\phi/2)$ in steps $\delta\alpha = 0.2$, $\beta_L = 0$. The increase of the $\sin(\phi/2)$ component causes a decrease of the oscillation amplitude without introducing a $2\Phi_0$ component.

6.3.1 dc SQUIDs composed of trivial and non-trivial elements

The considered dc SQUID is composed of a topologically trivial ring, and two non-trivial junctions, as shown in Fig. 7.1a. Figure 7.2 shows the critical current dependence of the dc SQUID. In this figure, the non-trivial junctions develop their current phase relationship from pure $\sin(\phi)$ to pure $\sin(\phi/2)$ in steps $\delta\alpha = 0.2$. Note that all graphs are calculated for $\beta_L = 0$, a situation which for standard SQUIDs leads to a complete critical current modulation. The $2\Phi_0$ periodicity due to the $\sin(\phi/2)$ component, tends to be completely obscured by the trivial superconducting ring. Quantum phase slips cause the usual Φ_0 periodicity, equivalent to what is calculated by Heck *et al.*[28] when one of the junctions is topologically trivial. When $\chi_1 = \sin(\phi/2)$ and $\chi_2 = \sin(\phi)$ we obtain the result of Fig. 7.2 for α approximately 0.7, shifted by an additional $\frac{1}{4}\Phi_0$. Instead of $2\Phi_0$ periodicity, the $\sin(\phi/2)$ component influences the modulation depth of the SQUID. There is no appearance of asymmetry as is the case for asymmetric SQUIDs, with different critical currents of the individual junctions[29]. The decrease in modulation depth by increasing the $\sin(\phi/2)$ component looks similar to increasing β_L in standard SQUIDs. However, this is a parameter that can be controlled externally, and a large β_L results in more triangular oscillations. If one junction is topologically trivial, the same effect occurs, combined with a phase shift due to asymmetry between the junctions. Therefore, even in rings including topologically trivial components, a $\sin(\phi/2)$ current phase relationship can be detected, although the effect is more subtle than a $2\Phi_0$ periodicity.

6.3.2 Topologically non-trivial SQUIDs

In the case when the ring is completely topologically non-trivial, corresponding to Fig. 7.1b, $2\Phi_0$ periodicity is to be observed. In the limiting case $\beta_L = 0$ and $I = I_c \sin(\phi/2)$, the critical current dependence on field can be written as $I = 2I_c|\cos(\pi\frac{\Phi}{2\Phi_0})|$, resulting in the $2\Phi_0$ periodicity. If both $\sin(\phi)$ and $\sin(\phi/2)$ components are present in the junctions, both periodicities are observed, as shown in Fig. 7.3a for equal ratios in the junctions. Interestingly, increasing β_L results in a larger $2\Phi_0$ component and a reduced Φ_0 component. In Fig. 7.3b the ratio dependence on β_L is shown, where the ratio is defined using the frequency amplitude after Fourier transformation. The screening parameter β_L is composed of the critical current of the junctions, and the inductance of the ring determined by geometrical factors, but is also dependent on the charge carrier in the ring. Since Majorana tunneling is with charge e instead of $2e$ as is the case for Cooper pair transport, the effective screening is reduced by a factor 2. By optimizing β_L using the tunable inductance of the ring, it is therefore possible to dramatically increase the $2\Phi_0$ component relative to the standard Φ_0-periodic component, ideal for the observation of the Majorana fermion.

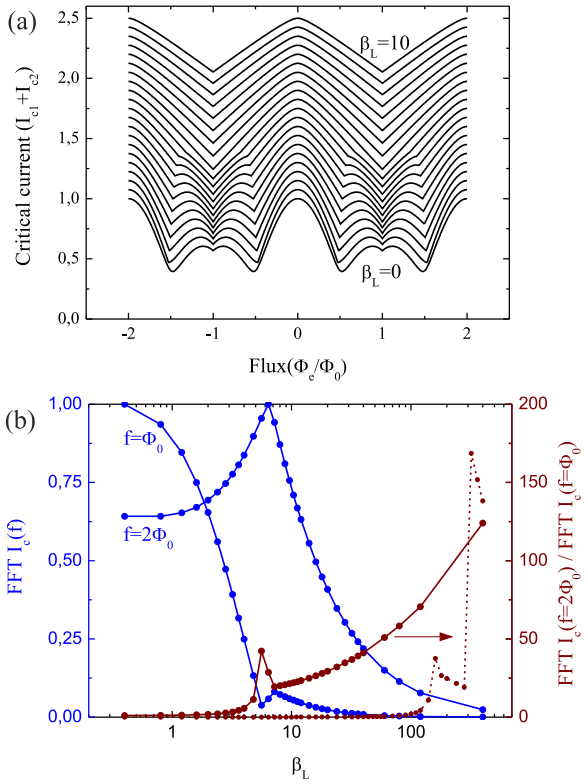

Figure 6.3: IΦ characteristics of a dc SQUID composed of a topologically non-trivial superconducting ring and non-trivial junctions. (a) dc SQUID oscillations for two symmetric junctions with equal amplitude $\sin(\phi)$ and $\sin(\phi/2)$ components, $\alpha = 0.5$. Increasing β_L (in steps $\delta\beta_L = 0.5$, and shifted for clarity) promotes the $2\Phi_0$ period, since the effective screening is smaller for Majorana tunneling than Cooper pair tunneling. **(b)** (blue) FFT amplitude of the two components as function of β_L. (red) Evolution of the FFT amplitude ratio as a function of β_L. The dashed lines represent the ratio when the junctions have only 5% $\sin(\phi/2)$ component contribution. The $2\Phi_0$ component can be more than 2 orders of magnitude larger than the Φ_0 component.

6.3.3 The voltage state

When the SQUID is operated in the voltage mode, both Φ_0 and $2\Phi_0$ periodicity can be observed, even if the ring includes trivial components. The relative amplitude depends on the voltage, controlled by the bias current. Figure 7.6a shows the IV characteristics for a dc SQUID with either pure $\sin(\phi)$ or $\sin(\phi/2)$ components. The current modulation for high voltages is inverted with respect to the modulation for small voltages. This is the result of the nonlinear interaction of the ac Josephson current with the resonant circuit formed by the loop inductance L and the junction capacitance C. This resonance voltage is given by $V_{res} = \gamma_{pj}\sqrt{\frac{2}{\beta_C\beta_L}}I_cR$. As a result, the $\sin(\phi)$ and $\sin(\phi/2)$ components cause oscillations with different frequency as a function of voltage, see Fig. 7.6b. Consequently, the relative amplitude of the 2 and 4π periodicity of the $V(\phi)$ characteristics, shown in Fig. 6.5 for $\beta_C = 1$, and $\beta_L = 1$ depend on the resonance voltages $V_{res,\phi}$ and $V_{res,\phi/2}$, which is controlled by the bias current. The resonance voltage is independent of the loop parity, but for $\gamma_{pl} = 1$ the oscillation amplitude is reduced by quantum phase slips. This is similar to the cause of the incomplete critical current modulation shown in Fig. 7.2.

The damping of the current modulation with increasing bias voltage is characterized by $\zeta = \sqrt{\frac{2\beta_C}{\beta_L}}$, independent on the current phase periodicity, and SQUIDs with $\sin(\phi/2)$ component junctions have therefore a smaller current modulation where the modulation is inverted, compared to standard SQUIDs. Choosing a large β_L will decrease the damping term and increase the amplitude of the voltage resonances. A small β_C will reduce the damping term but increase the resonance voltage.

6.4 Applications to topologically non-trivial systems

We now discuss the implications of our proposals. The possible realization of a new emergent particle in condensed matter physics together with the potential for quantum computation, boosted the search for superconducting systems hosting the Majorana fermion. Superconductor - semiconductor structures in the presence of strong spin orbit coupling and Zeeman fields are currently quite successful and signatures of Majorana fermions have been observed characterized by zero bias conductance peaks[23]. In superconductor - topological insulator junctions, Josephson supercurrents have also been observed[19–21,30]. In the case of topological insulator systems, bulk shunting likely introduces $\sin(\phi)$ terms in the current phase relation. Quantum phase slips[17] and quasiparticle poisoning[16] will be relevant for all proposals, relaxing the system to $\sin(\phi)$ periodicity. Therefore, increasing the $\sin(\phi/2)$ component is important for all these proposals.

The parameter β_L is easily tunable. This SQUID parameter depends on the

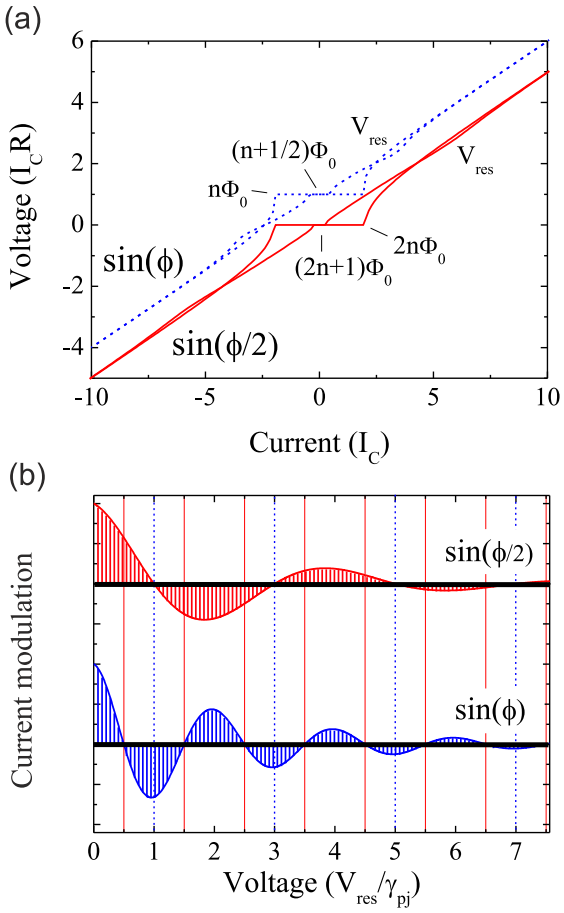

Figure 6.4: *IV* **characteristics of a topologically non-trivial dc SQUID. (a)** dc SQUID *IV* characteristics for junctions with $\sin(\phi)$ and $\sin(\phi/2)$ current phase relationships; $\beta_C = 1, \beta_L$=1. The $\sin(\phi/2)$ (solid line) component doubles the resonance voltage V_{res} (dashed line) with respect to the standard SQUID. The *IV* characteristic of the standard SQUID is shifted for clarity. **(b)** Damping and resonance in the SQUID. The $\sin(\phi/2)$ component oscillates with half the frequency, so that the $\sin(\phi)$ and $\sin(\phi/2)$ components have their minima and maxima at different voltages (solid red are maxima for the $\sin(\phi/2)$ component and dashed blue maxima for the $\sin(\phi)$ component.

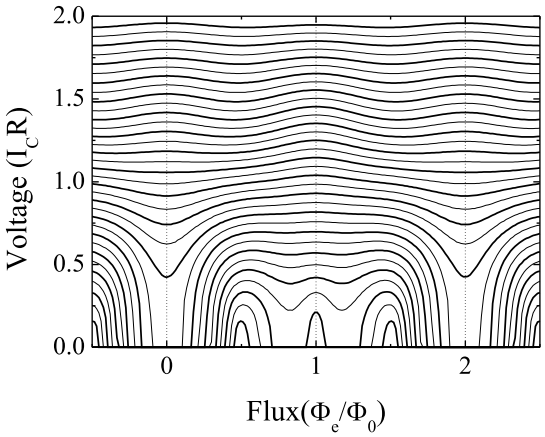

Figure 6.5: Topologically non-trivial dc SQUID in the voltage mode. $V\phi$ characteristics of a dc SQUID with equal $\sin(\phi)$ and $\sin(\phi/2)$ components in the junctions, and $\beta_C = 1, \beta_L = 1$. The SQUID shows both Φ_0 and $2\Phi_0$ periodicity, depending on the voltage close to $V_{res,\phi}$ or $V_{res,\phi/2}$, which is controlled by the bias current.

inductance, determined by the SQUID geometry, and is independent on the individual junctions. The parameter β_C is a junction parameter and therefore more difficult to tune. However, varying the length and width of the junctions and controlling the interface transparency tune β_C. Since SQUID fabrication is the most straightforward step after realizing Josephson junctions we expect that our proposal is particularly timely.

6.5 Conclusions

In conclusion, we have studied dc SQUIDs containing two topologically non-trivial barriers. The $2\Phi_0$ periodicity stemming from the Majorana fermion can only be detected in non-trivial dc SQUIDs. However, even loops containing topologically trivial elements are influenced by the presence of junctions with $\sin(\phi/2)$ components. This is observed both in the critical current modulation by flux and the resonance voltage. The SQUID parameters can be used to increase the relative component; increasing β_L is found to largely increase the component with the largest periodicity. The $V(\phi)$ relation is altered when both components are present, and both components can be maximized at different bias currents, determined by the resonance voltage. In recently fabricated S-TI-S junctions, β_C is usually low due to bulk shunting. This increases the resonance voltage to a regime where the

damping is higher, which complicated observing a clear difference between Φ_0 and $2\Phi_0$ periodicities. Decreasing this bulk shunt would therefore simplify the $2\Phi_0$ periodicity observation. Nonetheless, the strong effect of β_L; large β_L increases the $2\Phi_0$ component over 100 times, allows the detection of the Majorana fermion, under the right intrinsic circumstances (e.g. no relaxation to equilibrium), in dc SQUIDs composed of present day S-TI-S junctions. This result is also of relevance to devices where the Majorana character is induced via other means, such as in semiconducting nanowires with strong Rashba spin orbit coupling. Tuning β_L in combination with ac measurements to prevent relaxation paves the way to the observation of exotic properties of the Majorana fermion.

Bibliography

[1] L. Fu and C.L. Kane Phys. Rev. Lett. **100**, 096407 (2008).

[2] Y. Tanaka, T. Yokoyama, and N. Nagaosa, Phys. Rev. Lett. **103**, 107002 (2009).

[3] B.A, Bernevig, T.L. Hughes, and S.C. Zhang Science **314**, 1757 (2006).

[4] L. Fu, C.L. Kane, and E.J. Mele Phys. Rev. Lett. **98**, 106803 (2007).

[5] D. Hsieh, D. Qian, L. Wray, Y. Xia, Y.S. Hor, R.J. Cava, and M.Z. Hasan, Nature **452**, 970 (2008).

[6] H. Zhang, C.X. Liu, X.L. Qi, X. Dai, Z. Fang, and S.C. Zhang, Nature Phys. **5**, 438 (2009).

[7] X.L. Qi, L. Rundong, J. Zang, and S.C. Zhang, Science **323**, 1184 (2009).

[8] Y.L. Chen, J.G. Analytis, J.H. Chu, Z.K. Liu, S.K. Mo, X.L. Qi, H.J. Zhang, D.H. Lu, X. Dai, Z. Fang, S.C. Zhang, I.R. Fisher, Z. Hussain, and Z.X. Shen, Science **325**, 178 (2009).

[9] D. Hsieh, Y. Xia, D. Qian, L. Wray, J.H. Dil, F. Meier, J. Osterwalder, L. Patthey, J.G. Checkelsky, N.P. Ong, A.V. Fedorov, H. Lin, A. Bansil, D. Grauer, Y.S. Hor, R.J. Cava, and M.Z. Hasan, Nature **460**, 1101 (2008).

[10] H. Peng, K. Lai, D. Kong, S. Meister, Y. Chen, X.L. Qi, S.C. Zhang, Z.X. Shen, and Y. Cui, Nature Mat. **9**, 225 (2010).

[11] T. Zhang, P. Cheng, X. Chen, J.F. Jia, X. Ma, K. He, L. Wang, H. Zhang, X. Dai, Z. Fang, X. Xie, and Q.K. Xue, Phys. Rev. Lett. **103**, 266803 (2009).

[12] P. Cheng, C. Song, T. Zhang, Y. Zhang, Y. Wang, J.F. Jia, J. Wang, Y. Wang, B.F. Zhu, X. Chen, X. Ma, K. He, L. Wang, X. Dai, Z. Fang, X. Xie, X.L. Qi, C.X. Liu, S.C. Zhang, and Q.K. Xue, Phys. Rev. Lett. **105**, 076801 (2010).

[13] J.D. Sau, R.M. Lutchyn, S. Tewari, S. Das Sarma, Phys. Rev. Lett. **104**, 040502 (2010).

[14] J. Alicea, Phys. Rev. B **81**, 125318 (2010).

[15] E. Majorana, Nuovo Cimento **14**, 171 (1937).

[16] L. Fu and C.L. Kane, Phys. Rev. B **79**, 161408(R) (2009).

[17] C.W.J. Beenakker, Arxiv:1112.1950v2 (2012).

[18] D.M. Badiane, M. Houzet and J.S. Meyer, Phys. Rev. Lett **107**, 177002 (2011).

[19] D. Zhang, J. Wang, A.M. DaSilva, J.S. Lee, H.R. Gutierrez, M.H.W. Chan, J. Jain, and N. Samarth, Phys. Rev. B **84**, 165120 (2011).

[20] B. Sacépé, J.B. Oostinga, J.L. Li, A. Ubaldini, N.J.G. Couto, E. Giannini, and A.F. Morpurgo, Nature Comm. **2**, 575 (2011).

[21] M. Veldhorst, M. Snelder, M. Hoek, T. Gang, X.L. Wang, V.K. Guduru, U. Zeitler, W.G. v.d.Wiel, A.A. Golubov, H. Hilgenkamp, and A. Brinkman, Nature Mat. **11**, 417 (2012).

[22] M. Veldhorst, C.G. Molenaar, X.L. Wang, H. Hilgenkamp, and A. Brinkman, Appl. Phys. Lett. **100**, 072602 (2012).

[23] V. Mourik, K. Zuo, S.M. Frolov, S.R. Plissard, E.P.A.M. Bakkers, and L.P. Kouwenhoven, Science **336**, 1003 (2012).

[24] A.A. Golubov, M.Y. Kupriyanov, and E. Il'ichev, Rev. Mod. Phys. **76**, 411 (2004).

[25] K. Kang, Eur. Phys. Lett. **51**, 2 (2000).

[26] F. Loder, A.P. Kampf, and T. Kopp, Phys. Rev. B **78**, 174526 (2008).

[27] L. Fu, Phys. Rev. Lett. **104**, 056402 (2010).

[28] B. van Heck, F. Hassler, A.R. Akhmerov, and C.W.J. Beenakker, Phys. Rev. B **84**, 180502(R) (2011).

[29] C.D. Tesche and J.C Clarke, J. Low. Temp. Phys. **29**, 301 (1977).

[30] F. Qu, F. Yang, J. Shen, Y. Ding, J. Chen, Z. Ji, G. Liu, J. Fan, X. Jing, C. Yang, and L. Lu, Sci. Rep. **2**, 339.

Chapter 7 Experimental realization of SQUIDs with topological insulator junctions

Abstract

We demonstrate topological insulator (Bi_2Te_3) dc SQUIDs, based on superconducting Nb leads coupled to nano-fabricated Nb-Bi_2Te_3-Nb Josephson junctions. The high reproducibility and controllability of the fabrication process allows the creation of dc SQUIDs with parameters that are in agreement with design values. Clear critical current modulation of both the junctions and the SQUID with applied magnetic fields have been observed. We show that the SQUIDs have a periodicity in the voltage-flux characteristic of Φ_0, of relevance to the ongoing pursuit of realizing interferometers for the detection of Majorana fermions in superconductor - topological insulator structures.

7.1 Introduction

A three-dimensional topological insulator is an insulator in the bulk, but has conducting surface states that can be described by means of a Dirac cone in which the spin is locked to the electron momentum [1–10]. Electrons with opposite spin have opposite momenta, which suppresses backscattering, rendering these materials interesting for low power electronic devices. Combining the helical Dirac fermions with a superconductor [11–13] may lead to the artificial creation of the elusive Majorana fermion [14]. In the search for the Majorana fermion, efforts have been made to contact a topological insulator (TI) to a superconductor (S). Supercurrents in S-TI-S junctions have been reported [15–17]. The combined evidence for a ballistic Josephson supercurrent and the presence of topological surface states, show that topological Josephson junctions can be made, despite the presence of a conductivity shunt through the bulk of the TI crystal [17], Chapter 5.

In this Chapter, we demonstrate dc SQUIDs consisting of Josephson junctions with topological insulator surface states as barrier layer. These interference devices potentially serve as a basis to detect the Majorana fermion. Majorana bound states may appear in the vortex of a topological superconductor and at S-TI interfaces [11,13]. In the latter, time reversal symmetry in the topological insulator needs to be broken, for example by incorporating a magnetic insulator layer or by applying an external magnetic field. Intriguing devices are proposed to identify the

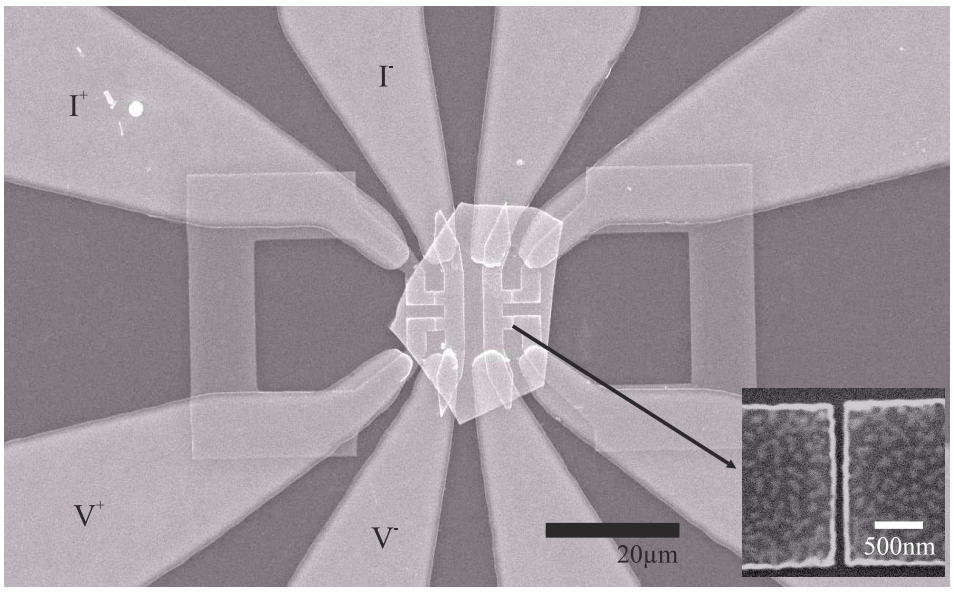

Figure 7.1: Image of the dc SQUID device. Scanning Electron Microscopy image of dc SQUIDs with topological insulator nano junctions. Two SQUIDs with junctions having a separation length $l = 120$ nm are designed on an exfoliated Bi_2Te_3 (200 nm height) flake. The two Nb arms are differently sized resulting in an asymmetric SQUID. Nb is sputter deposited and defined by e-beam lithography. Inset shows a Josephson junction.

appearance of this exotic particle[11–13,18]. Since the Majorana fermion is charge neutral and is a zero energy state, most proposals rely upon quantum interference devices. For example, a current-phase relationship with a 4π periodicity[11] might result from the interplay between the Majorana fermion and a superconductor, as also discussed in Chapter 6. We therefore study the current-phase relationship of the topological dc SQUID.

7.2 Fabrication of dc SQUIDs

Figure 7.1 shows two superconductor Nb - topological insulator Bi_2Te_3 dc SQUIDs fabricated on one Bi_2Te_3 flake. We have fabricated polycrystalline Bi_2Te_3 samples with a common c-axis orientation using the Czochralski method as described elsewhere[19]. Using mechanical exfoliation, Bi_2Te_3 flakes ranging in thickness from 30 nm to 1 µm are transferred to a Si substrate. The Bi_2Te_3 flakes are smooth on the nm scale over areas of several μm^2. Figure 7.2 shows an Atomic Force Microscopy image of the surface of a typical Bi_2Te_3 flake, revealing the 1.0 nm quintuple unit cell layers of Bi_2Te_3. After exfoliation, a superconducting ($T_C = 9$ K) Nb-layer (200 nm) is sputter deposited with a 5 nm Pd layer deposited *in situ* on top to protect the Nb against oxidation. Electrodes are defined by optical photolithography.

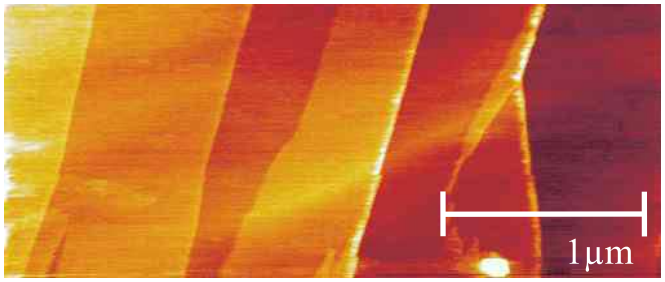

Figure 7.2: Bi_2Te_3 surface image. Atomic force microscopy image of an exfoliated Bi_2Te_3 surface. The step edges are 1.0 nm high, corresponding to the Bi_2Te_3 quintuple unit cell. These nanometer flat surfaces span an area up to 50 × 50 µm^2.

The Nb on top of the Bi_2Te_3 flake makes a strong superconducting contact with the Nb on the substrate. Finally, nanojunctions are defined by lift-off e-beam lithography and sputter deposition of Nb. The substrate is slightly conducting (ρ =5Ωcm) at room temperature to increase the resolution of e-beam lithography, but is completely insulating at low temperatures. Prior to deposition, *in situ* Ar-ion etching is performed in order to make transparent contacts. It is found that Ar etching roughens the Bi_2Te_3 surface, probably by preferential etching, but 2 minutes etching with a substrate bias voltage of 50 V leaves a Bi_2Te_3 surface with 1-2 nm roughness and a transparent contact. Throughout the fabrication process the Bi_2Te_3 surface in between the Nb leads has only been covered by resist, leaving the surface of the junction barrier layer unaffected from Ar-ion etching and deposition steps. Two separate electrodes connected by Nb over the Bi_2Te_3 flake, for example the positive current and voltage leads, have a superconducting contact with a critical current exceeding 30 mA, ensuring a large supercurrent through all layers.

We have designed two SQUIDs on one Bi_2Te_3 flake (200 nm height), see Fig. 7.1. The nanojunctions are 2 µm wide and have a length l = 120 nm. The inductance ratio between the two arms is about λ = 0.2. In a square washer approximation[20] the total effective area of the SQUID is 920 µm^2, and the estimated inductance 46 pH. Both SQUIDs showed similar behavior, but in the rest of the paper we focus on the left SQUID of Fig. 1.

7.3 Josephson supercurrent through a dc SQUID

Below 6 K, the superconducting proximity effect induces a Josephson supercurrent through the junctions and at 1.4 K the dc SQUID has a critical current of 30 µA, as shown in figure 7.3. This results in a 2D critical current per width of the junction of 7.5 A/m, which is within 10 % of the individually measured critical current density of junctions on different flakes; see Chapter 5 for the characterization of

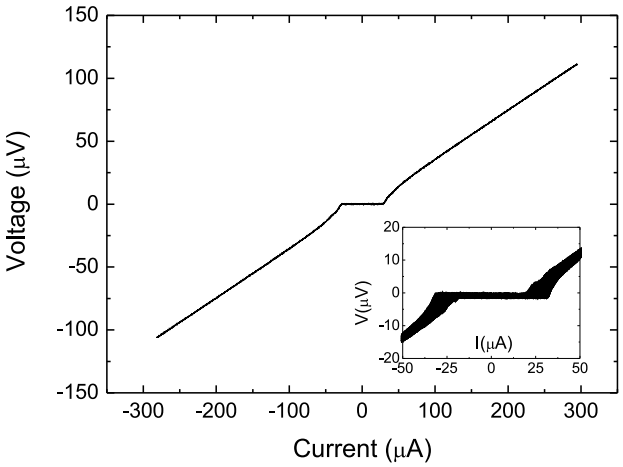

Figure 7.3: IV-characteristics. IV-curve of the topological dc SQUID with a typical critical current of 30 μA. The junctions are 2 μm wide and have an electrode separation of 120 nm. The intrinsic bulk shunt has reduced the $I_C R_N$ product to 10 μV. Inset shows the IV-curve under magnetic field modulation.

individual junctions. The SQUID had a critical current constant within 10 % over three cooldowns running over several weeks. Due to shunting of the junctions results we find a relative low $I_C R_N = 10$ μV. Ballistic junctions with $\xi_T \approx 80$ nm, $T_C = 6$ K and $l = 120$ nm, have an estimated $I_C R_N \approx 130 - 260$ μV, but the shunt due to the bulk conductance reduces the characteristic voltage to a few percent of the expected value[17], consistent with the observed 10 μV. In order to obtain higher $I_C R_N$ values, electrical gating or chemical substitution, e.g. Bi_2Se_2Te[21], could be used. The current-voltage characteristics are intrinsically non-hysteretic because of the low capacitance of the lateral geometry of the junctions and the high transparency of the interfaces.

7.4 SQUID modulation characteristics

Applying an external magnetic field causes oscillations of the superconducting critical currents due to interference of the two arms, shown in Fig. 7.6. This modulation of I_C unequivocally demonstrates the correct operation of the Nb-Bi_2Te_3 SQUID. The voltage modulation is strongest at a bias of approximately 40 μA, which corresponds to a current close to the critical current of the SQUID. The critical current modulation is $\sim 35\%$ of the total critical current. Using a simple model based on a sinusoidal current-phase relation of the junctions, and taking inductance and possible asymmetries into account, we can fit the field dependence with high accuracy. The asymmetrical inductance causes an asymmetry in the SQUID current-phase relationship, see Fig. 7.6. We also observe a shift in the current-phase relationship when increasing the bias current. The two arms of the

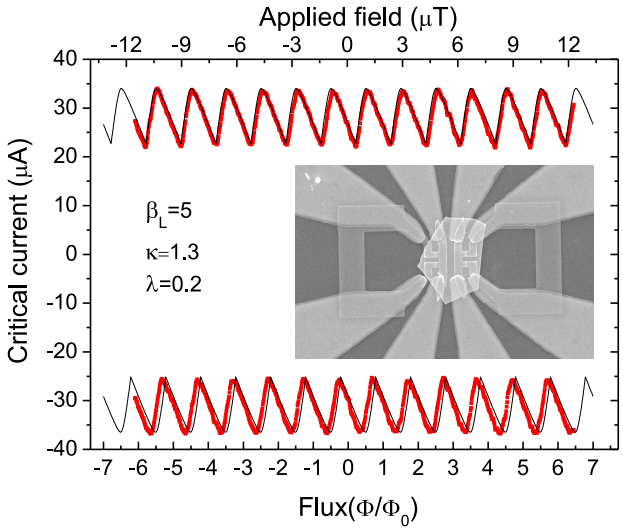

Figure 7.4: $I\Phi$-modulation. Dc SQUID critical current modulation on applied magnetic field. The critical current of the SQUID can be fitted (thin line) by a model that accounts for the asymmetry of the design with fitting parameters, $\beta_L = 5$, the critical current ration $\kappa = 1.3$, and inductance ratio $\lambda = 0.2$.

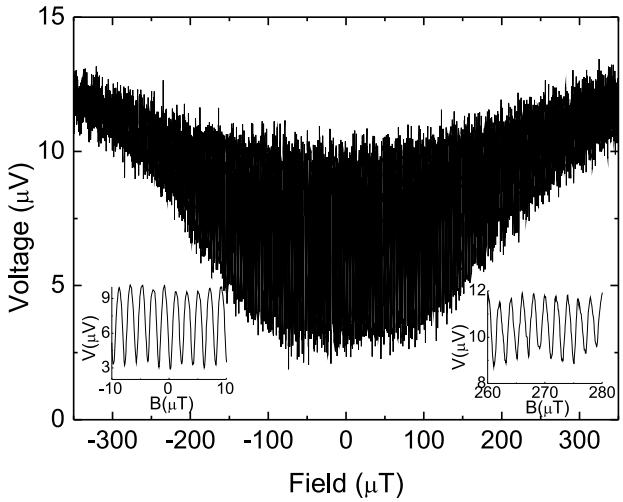

Figure 7.5: SQUID and individual junction modulation. Voltage modulation of the dc SQUID. The critical current of the individual junctions is suppressed at 350 μT (Fraunhofer pattern). SQUID oscillations are still observable. Inset shows the SQUID oscillations at small fields (left) and large fields (right).

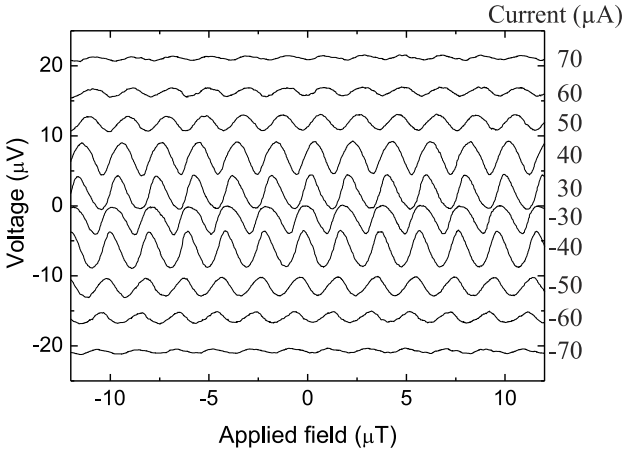

Figure 7.6: The voltage state. Voltage modulation of the dc SQUID. The $V - \phi$ relationship reveals an asymmetric response as well as a shift for increasing bias currents. The solid lines represent equicurrents for ± 30-70 μA.

SQUID have different inductances and critical currents, which results in a growing field threading the SQUID for increasing current. The SQUID inductance $L = \frac{\Phi_0}{2\pi}\frac{\beta_L}{I_c} = 55$ pH combined with the inductance asymmetry $\lambda = 0.2$ give inductances $L_1 = 9$ pH and $L_2 = 46$ pH. At a bias current of 90 μA, a current ratio through both arms of 1.1 is estimated using the critical current differences and assuming an equal normal state resistance. This results in a shift of 0.74 Φ_0, comparable to the observed shift of 0.75 Φ_0. At the optimum bias, the sensitivity of the SQUID is 15 μV/Φ_0. In the limit β_L (= 5) $\gg 1$, the sensitivity of a SQUID can be estimated by R/L[22] which yields 12 μV/Φ_0.

As expected, the SQUID modulation frequency is much larger than that of the individual junctions, see Fig. 7.6. A SQUID oscillation corresponds to 1.9 μT, while the critical current of the junctions is suppressed at 350 μT. This corresponds to about 180 SQUID oscillations in a junction oscillation, which is slightly lower than expected by comparing the enclosed areas. However, for the enclosed area of a junction, the Josephson penetration depth and flux focusing has to be included, which increases the junction effective area[17].

7.5 Trivial Φ_0 periodicity

Since the supercurrent is carried by topological surface states[17] we can study the current-phase relationship of topological junctions by means of our dc SQUID. In a dc SQUID with topological insulator surface states as interlayers, the phase difference over the junctions due to a given field is equal to a standard SQUID.

However, the presence of Majorana fermions can cause a $I_C = I_0 \sin(\phi/2)$ junction current-phase relation, resulting in a 4π periodic dependence of the junctions[11]. To test the periodicity of the SQUID, the magnetic field from the coil is calibrated with a Hall sensor and the effective area of the SQUID, 920 μm^2, is estimated using the square washer approximation[20]. A 2π periodic dependence within 7 % accuracy is calculated, enough to exclude 4π periodicity. The absence of a 4π periodic dependence might be due to relaxation to equilibrium states, as was predicted theoretically[23,24].

In Chapter 6 we discussed dc SQUIDs composed of junctions consisting of both non-trivial $\sin(\phi/2)$ and trivial $\sin(\phi)$ components. The superconducting ring is a macroscopic superconductor and is expected to reduce the system to ϕ_0 periodicity due to e.g. quantum phase slips[25] and quasiparticle poisoning[23]. Still, the $\sin(\phi/2)$ component can alter the results, as shown in Chapter 6. The appearance of such a term reduces the total critical current modulation. The maximal critical current modulation of a dc SQUID composed of junctions with a pure $\sin(\phi/2)$ current phase relationship (obtained when $\beta_L = 0$) is still 4% smaller than the critical current modulation observed in Fig. 7.6, excluding this possibility. Furthermore, the inclusion of $\sin(\phi/2)$ components changes the shape of the modulation, and from this we can conclude that the $\sin(\phi/2)$ term contributes less than 30% of the total critical current. Possible ways to test whether small $\sin(\phi/2)$ components are present is changing the SQUID geometry to tune β_L, and to measure faster, with time scales comparable to the relaxation time, which is on the order of Δ[23,24].

7.6 Conclusions

In conclusion, we have demonstrated Nb-Bi_2Te_3 SQUIDs. As shown previously[17], the supercurrent is carried by the topological surface states, thereby allowing the study of the current-phase relationship of superconductor- topological insulator structures. From the $V - \phi$ characteristics we deduced a 2π periodic current-phase relationship. The high reproducibility allows the study of the noise properties of these devices in future experiments and to eventually include magnetic insulators in order to break time reversal symmetry to create Majorana bound states.

Bibliography

[1] B.A, Bernevig, T.L. Hughes, and S.C. Zhang, Science **314**, 1757 (2006).

[2] L. Fu, C.L. Kane, and E.J. Mele, Phys. Rev. Lett. **98**, 106803 (2007).

[3] D. Hsieh, D. Qian, L. Wray, Y. Xia, Y.S. Hor, R.J. Cava, and M.Z. Hasan, Nature **452**, 970 (2008).

[4] H. Zhang, C.X. Liu, X.L. Qi, X. Dai, Z. Fang, and S.C. Zhang, Nature Phys. **5**, 438 (2009).

[5] X.L. Qi, L. Rundong, J. Zang, and S.C. Zhang, Science **323**, 1184 (2009).

[6] Y.L. Chen, J.G. Analytis, J.H. Chu, Z.K. Liu, S.K. Mo, X.L. Qi, H.J. Zhang, D.H. Lu, X. Dai, Z. Fang, S.C. Zhang, I.R. Fisher, Z. Hussain, and Z.X. Shen, Science **325**, 178 (2009).

[7] D. Hsieh, Y. Xia, D. Qian, L. Wray, J.H. Dil, F. Meier, J. Osterwalder, L. Patthey, J.G. Checkelsky, N.P. Ong, A.V. Fedorov, H. Lin, A. Bansil, D. Grauer, Y.S. Hor, R.J. Cava, and M.Z. Hasan, Nature **460**, 1101 (2008).

[8] H. Peng, K. Lai, D. Kong, S. Meister, Y. Chen, X.L. Qi, S.C. Zhang, Z.X. Shen, and Y. Cui, Nature Mat. **9**, 225 (2010).

[9] T. Zhang, P. Cheng, X. Chen, J.F. Jia, X. Ma, K. He, L. Wang, H. Zhang, X. Dai, Z. Fang, X. Xie, and Q.K. Xue, Phys. Rev. Lett. **103**, 266803 (2009).

[10] P. Cheng, C. Song, T. Zhang, Y. Zhang, Y. Wang, J.F. Jia, J. Wang, Y. Wang, B.F. Zhu, X. Chen, X. Ma, K. He, L. Wang, X. Dai, Z. Fang, X. Xie, X.L. Qi, C.X. Liu, S.C. Zhang, and Q.K. Xue, Phys. Rev. Lett. **105**, 076801 (2010).

[11] L. Fu, C.L. Kane, and E.J. Mele, Phys. Rev. Lett. **100**, 096407 (2008).

[12] J. Nilsson, A.R. Akhmerov, and C.W.J. Beenakker, Phys. Rev. Lett. **101**, 120403 (2008).

[13] Y. Tanaka, T. Yokoyama, and N. Nagaosa, Phys. Rev. Lett. **103**, 107002 (2009).

[14] E. Majorana, Nuovo Cimento **14**, 171 (1937).

[15] D. Zhang, J. Wang, A.M. DaSilva, J.S. Lee, H.R. Gutierrez, M.H.W. Chan, J. Jain, and N. Samarth, Phys. Rev. B **84**, 165120 (2011).

[16] B. Sacépé, J.B. Oostinga, J.L. Li, A. Ubaldini, N.J.G. Couto, E. Giannini, and A.F. Morpurgo, Nature Comm. **2**, 575 (2011).

[17] M. Veldhorst, M. Snelder, M. Hoek, T. Gang, X.L. Wang, V.K. Guduru, U. Zeitler, W.G. v.d.Wiel, A.A. Golubov, H. Hilgenkamp, and A. Brinkman, Nature Mat. **11**, 417 (2012).

[18] C.W.J. Beenakker, Arxiv:1112.1950v2 (2012).

[19] A.H. Li, M. Shahbazi, S.H. Zhou, G.X. Wang, C. Zhang, P. Jood, G. Peleckis, Y. Du, Z.X. Cheng, X.L. Wang, and Y.K. Kuo, Thin Sol. Films. **518**, 57 (2010).

[20] M.B. Ketchen, W.J. Gallagher, A.W. Kleinsasser, S. Murphy and J.R. Clem, SQUID 85-Superconducting Quantum Interference Devices and their Applications (Berlin: de Gruyter) p865 (1985).

[21] S. Jia, H. Ji, E. Climent-Pascual, M.K. Fuccillo, M.E. Charles, J. Xiong, N.P. Ong, and R.J. Cava, Phys. Rev. B **84**, 235206 (2011).

[22] C.D. Tesche and J. Clarke, Low Temp. Phys. **29**, 301 (1977).

[23] L. Fu and C.L. Kane, Phys. Rev. B **79**, 161408(R) (2009).

[24] D.M. Badiane, M. Houzet and J.S. Meyer, Phys. Rev. Lett. **107**, 177002 (2011).

[25] B. van Heck, F. Hassler, A.R. Akhmerov, and C.W.J. Beenakker, Phys. Rev. B **84**, 180502(R) (2011).

Summary

This thesis is devoted to the study of superconducting and topological hybrids. Superconducting charge transport is mediated by Cooper pairs, which can be used to generate spatially separated nonlocal entangled particles by coupling two spatially separated normal electrodes to a superconductor. Superconducting charge transport can also extend to non-superconducting materials via the proximity effect. When two closely separated superconductors are connected by another material, a Josephson supercurrent can flow between the superconductors. Unconventional superconductivity can arise at the interface by designing the right interlayers. Of particular importance are the magnetic properties of the interlayer. When the interlayer is ferromagnetic, a p-wave order parameter can be induced. However, at the same time the ferromagnetic interlayer can have a proximity effect on the superconductor via magnetic exchange and stray fields. p-wave superconductivity can also be realized by using topological insulators as interlayer, ultimately leading to the observation of a new emergent particle: the Majorana fermion.

In Chapter 2 of this thesis, hybrid systems consisting of a superconductor sandwiched between two ferromagnetic layers are studied. Experimentally, it is found that charge transport in these systems is dependent on the relative magnetization alignments of the ferromagnetic layers leading to resistance hysteresis by sweeping the magnetic field. When the device is composed of the high-T_C superconductor $YBa_2Cu_3O_{7-\delta}$ (YBCO) and the half-metallic ferromagnet $La_{0.67}Sr_{0.33}MnO_3$ (LSMO) a so-called 'inverse superconducting spin switch effect' occurs. The origin of this effect is found in the stray fields produced by the ferromagnetic layers. The resistance is dependent on the total field in the superconductor, determined by the external magnetic field and the two ferromagnetic layers. The magnetic field in the superconductor stemming from the ferromagnetic layers is opposite in direction to the magnetization direction of the ferromagnetic layers. Consequently, a parallel alignment of the magnetization direction of the ferromagnetic layers relative to the external field results in lower resistance than for an antiparallel alignment. The magnitude of the stray field is dependent on the homogeneity and roughness as found by comparing the smoother bottom interface to the top interface in these devices. Next to implications for 'superconducting spin switch effects', stray fields are important to consider in other systems composed of superconductor - ferromagnetic layers.

In Chapter 3, crossed Andreev reflection is theoretically studied. Via this process, Cooper pairs in a superconductor can be split into individual electrons by coupling two electrodes to the superconductor. This process called crossed Andreev reflection can be used to generate nonlocal spin entangled electrons. It is found that this process can be optimized resulting in currents composed of solely entangled electrons. In systems composed of normal electrodes, splitting in the same lead, Andreev reflection, and electron tunneling between the leads, elastic cotunneling, obscures crossed Andreev reflection. These mechanisms vanish in p-type semiconductor - superconductor - n-type semiconductor junctions due to energy filtering, leaving only crossed Andreev reflection. A natural barrier arises in these devices due to momentum mismatches, resulting in significant crossed Andreev reflection. The right electrodes may be realized using semiconductor bands, quantum confinement, Coulomb interaction and spin orbit interaction.

In Chapter 4, topological bilayer exciton condensates are theoretically studied. Exciton condensation has many similarities to superconducting condensation due to charge and direction reversal symmetry between electrons and holes. It is found that Andreev reflection on exciton bilayers results in currents composed of nonlocal entangled particles, with no contribution of local Andreev reflection and vanishing direct tunneling. Topological exciton condensates warrant spin singlet splitting and yield high Andreev reflection probabilities. Josephson junctions of topological exciton condensates exhibit zero modes and fractional charges quantized in $e/2$, which can be turned into Majorana fermions under applied magnetic fields or by coupling the top and bottom of a bilayer exciton condensate.

In Chapter 5,6 and 7, superconductor-topological insulator systems are studied experimentally and numerically. Superconducting Josephson junctions with topological insulator interlayers have been realized. Mechanical exfoliation on topological insulator bismuth telluride (Bi_2Te_3) crystals are shown to be a powerful method to obtain flakes with atomically flat terraces. In the normal state, magnetoresistance measurements on Bi_2Te_3 flakes show Shubnikov de Haas oscillations originating from two dimensional bands, as concluded from angle dependent measurements. The topological origin of these bands shift the field positions of the Landau levels due to the presence of a π Berry phase. Superconducting Josephson junctions are fabricated by contacting e-beam defined superconducting niobium (Nb) leads to the topological insulator flakes. A Josephson supercurrent has been observed through the topological insulator up to a length of 250 nm. The two hallmarks of Josephson superconductivity are observed: a Fraunhofer magnetic field dependence and Shapiro steps under microwave irradiation due to the dc and ac Josephson effect, respectively. The ballistic nature deduced from the temperature dependence evidences that the supercurrent is carried by the topological surface state. The Fraunhofer magnetic field dependence suggests an unusual current phase relation, although geometrical effects cannot be excluded. Superconducting quantum interference devices (SQUIDs) have been fabricated to further study the current phase relationship. Standard fluxoid quantization has been observed. High electron densities and relaxation mechanisms as quantum phase slips, quasiparticle

poisoning and bulk shunting drive the system to standard Cooper pair transport instead of single electron transport mediated by Majorana fermions. A numerical study on these SQUIDs elucidates that even in the presence of relaxation, signatures of the unusual $\sin(\phi/2)$ current phase relationships can be present. However, from fitting the experimental SQUIDs it is concluded that the $\sin(\phi/2)$ component is at least smaller than 30% of the total current. Nonetheless, these reproducable devices make a new platform to search for new phenomena including Majorana fermions. An interesting opportunity is to move towards gate tunable nanostructures, where quantized supercurrents appear with $\sin(\phi/2)$ current phase relationships due to absence of backscattering in one dimensional structures, elucidating the appearance of Majorana fermions.

In the introduction we posed the question: "As conventional hybrids have already led to very important phenomena, what to expect when interfacing exotic materials?". Interface physics in condensed matter physics has led in 1948 to the discovery of the transistor. The for that time highly unconventional transistor characteristics sparked the semiconductor revolution that changed our daily lives. Today, the unconventional effects include the realization of controllable spatially separated entangled particles and the emergence of Majorana fermions.

Samenvatting

Dit proefschrift is gewijd aan de studie van supergeleidende en topologische hybride systemen. Supergeleidend ladingstransport wordt bewerkstelligd door Cooperparen, die gebruikt kunnen worden om ruimtelijk gescheiden niet-lokale verstrengelde deeltjes te genereren door twee normale elektrodes op kleine afstand van elkaar aan een supergeleider te koppelen. Supergeleidend ladingstransport kan ook plaats vinden in niet supergeleidende materialen via het nabijheidseffect. Een Josephson superstroom kan lopen door twee supergeleiders die op kleine afstand gescheiden zijn door een dun laagje van een ander materiaal. Nieuwe vormen van supergeleiding kunnen ontstaan op het grensvlak van het supergeleidende en niet-supergeleidende materiaal bij de juiste keuze van de materialen. Als het tussenliggende niet-supergeleidende materiaal ferromagnetisch is kan een p-wave ordeparameter geïnduceerd worden. Echter, tegelijkertijd kan de ferromagnetische laag ook een nabijheidseffect op de supergeleider hebben via magnetische interactie en strooivelden. p-wave supergeleiding kan ook gerealiseerd worden door middel van het gebruik van topologische isolatoren als tussenlaag, wat uiteindelijk zou kunnen leiden tot de ontdekking van een nieuw verschijnsel: het Majorana fermion.

In hoofdstuk 2 van dit proefschrift zijn hybride systemen bestaande uit een supergeleidende laag omsloten door twee ferromagnetische lagen bestudeerd. Er is experimenteel gevonden dat in zulke systemen ladingstransport afhankelijk is van de relatieve magnetische oriëntatie van de ferromagnetische lagen. Deze afhankelijkheid zorgt voor het ontstaan van een magnetische weerstandshysterese. Als het systeem uit de hoge T_c supergeleider $YBa_2Cu_3O_{7-\delta}$ (YBCO) en de halfmetallische ferromagneet $La_{0.67}Sr_{0.33}MnO_3$ (LSMO) bestaat, ontstaat een zogenoemde 'inverse supergeleidende spinschakelaar'. Er is gevonden dat de oorzaak van het effect de magnetische strooivelden opgewekt door de ferromagnetische lagen zijn. De weerstand is afhankelijk van het totale magnetisch veld in de supergeleider, dat bepaald wordt door het externe magneetveld en het veld afkomstig van de twee ferromagnetische lagen. Het magnetisch veld in de supergeleider afkomstig van de ferromagnetische lagen heeft een richting tegenovergesteld aan de magnetisatierichting van de ferromagneten. Als gevolg daarvan is de weerstand bij een parallelle uitlijning van de magnetisatierichting van de ferromagnetische lagen relatief ten opzichte van het externe magneetveld lager dan bij een antiparallelle uitlijning. Er

is gevonden, na vergelijking van de gladdere onderste ferromagnetische laag met de ruwere bovenste ferromagnetische laag, dat de amplitude van het magnetisch strooiveld bepaald wordt door de homogeniteit en ruwheid van de lagen. Naast implicaties voor de 'inverse supergeleidende spinschakelaar' zijn strooivelden ook belangrijk om mee te nemen in andere structuren die bestaan uit supergeleidende en ferromagnetische lagen.

In hoofdstuk 3 is gekruiste Andreev reflectie theoretisch bestudeerd. Door middel van dit proces kunnen de individuele elektronen die samen Cooperparen vormen uit elkaar gehaald worden door twee elektrodes te koppelen aan een supergeleider. Dit gekruiste Andreev reflectie proces kan gebruikt worden om op afstand gescheiden niet-lokale en spin-verstrengelde elektronen te genereren. Er is gevonden dat dit proces geoptimaliseerd kan worden tot de limiet van stromen die alleen uit verstrengelde elektronen bestaan. In systemen waarbij de elektrodes normale metalen zijn, wordt gekruiste Andreev reflectie gemaskeerd door het splitsen van de elektronen in een enkele elektrode, Andreev reflectie, en elektrontunneling tussen de elektrodes, elastische cotunneling. Energiefiltering in een p-type halfgeleider - supergeleider - n-type halfgeleider configuratie zorgt er voor dat alleen gekruiste Andreev reflectie overblijft. Een intrinsieke barrière ontstaat door het impulsverschil van de elektrodes en de supergeleider wat zorgt voor een significante gekruiste Andreev reflectie-amplitude. Mogelijkheden tot de realisatie van deze elektrodes omvatten halfgeleiders, kwantum opsluiting, Coulomb interactie en spin-orbit interactie.

In hoofdstuk 4 zijn excitoncondensaten theoretisch bestudeerd. Excitoncondensatie heeft door de ladings- en richtingsomkeersymmetrie van elektronen en gaten vele overeenkomsten met supergeleidende condensatie. Er is gevonden dat Andreev reflectie aan exciton bilagen resulteert in stromen die bestaan uit niet-lokale verstrengelde deeltjes, en dat bijdrages van lokale Andreev reflectie en directe elektrontunneling verwaarloosbaar zijn. Topologische excitoncondensaten zorgen voor spin singlet opsplitsing met een hoge Andreev reflectiekans. Josephson juncties gemaakt van topologische exciton condensaten herbergen niveaus met energie nul en fractionele ladingen gekwantiseerd als $e/2$, die in Majorana fermionen vervormd kunnen worden door middel van het aanbieden van magnetische velden en het koppelen van de lagen van een topologische bilaag excitoncondensaat.

In hoofdstuk 5, 6 en 7 zijn supergeleider-topologische isolator systemen experimenteel en numeriek bestudeerd. Supergeleidende Josephson juncties met topologische isolator tussenlagen zijn gerealiseerd. Mechanische exfoliatie aan kristallen van de topologische isolator bismut-telluride (Bi_2Te_3) is een krachtige methode voor het verkrijgen van schilfers met terrassen die op atomaire schaal vlak zijn. Magnetoweerstandmetingen aan deze Bi_2Te_3 schilfers in de normale toestand laten Shubnikov de Haas oscillaties zien, die veroorzaakt worden door tweedimensionale banden, zoals volgt uit hoekafhankelijke metingen. De aanwezigheid van een Berry's fase van π, karakteristiek voor een topologisch niet-triviale toestand, zorgt voor een verschuiving van de Landau levels in het magnetisch veld. Supergeleidende Josephson juncties zijn gefabriceerd door middel van structurering via

elektronenstraallithografie van supergeleidend niobium (Nb) op schilfers van de topologische isolator. Een Josephson superstroom is geobserveerd door de topologische isolator over een afstand tot 250 nm. De twee kenmerken van Josephson supergeleiding zijn gemeten: een Fraunhofer magnetisch veldafhankelijkheid en Shapiro stappen als gevolg van microgolfbestraling, vanwege respectievelijk het *dc* en *ac* Josephson effect. Het ballistische karakter van de juncties is afgeleid uit de temperatuurafhankelijkheid en bewijst dat de superstroom gedragen wordt door de topologische oppervlaktetoestanden. De Fraunhofer magnetisch veldafhankelijkheid is uitnodigend om te verklaren met een bijzondere stroom fase relatie, maar andere effecten door bijvoorbeeld het ballistische karakter en extrinsieke geometrische effecten kunnen niet uitgesloten worden. Supergeleidende kwantum interferentie devices (SQUIDs) zijn gefabriceerd om de stroom fase relatie beter te kunnen bestuderen. Standaard flux kwantisatie is gemeten. Hoge elektrondichtheden en relaxatiemechanismes zoals kwantum fase slips, quasideeltjes vervuiling en bulk kortsluitingen zijn verklaringen die zorgen voor standaard Cooperparen transport in plaats van individuele elektrontransport gedragen door Majorana fermionen. Een numerieke studie aan deze SQUIDs brengt aan het licht dat zelfs in de aanwezigheid van relaxatie, aanwijzingen van de ongewone $\sin(\phi/2)$ stroom-fase relatie aanwezig kunnen zijn. Uit het fitten van de experimentele SQUID-data kan geconcludeerd worden dat de $\sin(\phi/2)$ component in ieder geval kleiner is dan 30% van de totale stroom. Echter, de reproduceerbaarheid van deze SQUIDs vormt een nieuw platform voor de speurtocht naar nieuwe verschijnselen, waaronder Majorana fermionen. Een interessante weg is het maken van elektrische veldeffect nanostructuren. Daarmee kunnen gekwantiseerde superstromen gerealiseerd worden met een $\sin(\phi/2)$ stroom-fase relatie als gevolg van de afwezigheid van botsingen in eendimensionale structuren. Deze experimenten kunnen dan de aanwezigheid van Majorana fermionen aantonen.

In de inleiding hebben we de vraag gesteld: “Als conventionele hybride systemen al voor zeer belangrijke verschijnselen hebben gezorgd, wat kunnen we dan verwachten bij het koppelen van exotische materialen?”. Grensvlakfysica heeft in 1948 in de vaste stoffysica geleid tot de ontdekking van de transistor. De toen zeer ongewone transistorkarakteristieken stonden aan de basis van de halfgeleiderrevolutie die ons dagelijkse leven zo veranderd heeft. Nu zijn de onconventionele effecten de realisatie van controleerbare gescheiden verstrengelde deeltjes en Majorana fermionen.

Dankwoord

In de afgelopen jaren heb ik met plezier aan dit proefschrift gewerkt. Zowel het plezier als de resultaten zouden er niet geweest zijn zonder de hulp die ik van anderen heb gekregen. Graag wil ik hen bedanken.

Alexander, bedankt dat je mijn promotor wilde zijn. Al vanaf mijn stageopdracht tijdens de studie ben je een grote motivator en inspirator geweest. Je altijd positieve insteek heeft voor een bijzonder goede begeleiding gezorgd. Hans, bedankt voor al je hulp. Je immer bijzonder snelle reacties op mail, op welk tijdstip dan ook, tijdens vakanties of midden in de nacht, hebben bij mij altijd enorme bewondering gewekt. Alexander en Hans, ik had mij geen beter team van promotors kunnen wensen. Jullie vormen een enorme bron van kennis en creativiteit.

Graag wil ik Jan Aarts bedanken voor de fijne samenwerking, die in korte tijd tot twee gezamenlijke publicaties heeft geleid, waaronder het werk van Shahbaz. Ik herinner mij de mooie discussies die openlijk gevoerd konden worden.

Verder wil ik Uli Zeitler en Jan Kees Maan bedanken voor de mogelijkheid om hoge veldmetingen uit te voeren in het 'High Field Magnet Laboratory' in Nijmegen. Samen met Veerendra heeft meteen de eerste meting geleid tot een publicatie in Nature, in de 'materials sectie'. Bedankt, ook voor jullie hulp in de analyse van de Shubnikov de Haas oscillaties.

Wilfred van der Wiel, bedankt voor alle tijd die ik op de Heliox mocht doorbrengen, zelfs na mijn experimenten om uit te testen hoe honderd liter helium in zo kort mogelijke tijd verdampt kan worden. Tian, ik wil je bedanken voor alle hulp die je hierbij hebt gegeven. De Helioxmetingen stonden aan de basis van de ontdekking van supergeleidende topologische isolator Josephson juncties.

Xiaolin Wang, thank you for supplying the bismuth-telluride crystals. These crystals are on the basis of already three publications. I will remember your positive outlook on where to publish our results.

Frank en Dick wil ik bedanken voor de hulp in het lab. Frank, bedankt dat ik de frustraties over het 'oude' elektronenstraallithografiesysteem heb mogen delen. Dick, ook bedankt voor alle discussies over mijn complexe fabricagestappen.

Sasha wil ik graag bedanken voor de zowel theoretische als experimentele discussies; ik heb veel van je geleerd over supergeleidende juncties. Sybolt bedankt voor de hulp bij de XRD-metingen op devices voor experimenten aan de 'supergeleidende spin-witch schakelaar'. Cor, bedankt voor de hulp tijdens de experimen-

ten bij de badcryostaat en bij het uitvoeren van de SQUID-simulaties. Maarten, het zal je waarschijnlijk niet opvallen, maar ik heb veel van je schrijfstijl geleerd. Ans en Inke wil ik graag bedanken voor alle administratieve ondersteuning, die ondanks mijn alles-op-het-laatste-moment-mentaliteit toch altijd vlekkeloos verliep.

Ik heb met veel plezier geleerd van de begeleiding bij de afstudeeronderzoeken van Michelle, Steven, Marcel, Diederik, Sander, Marieke en Hidde. Marcel, samen met jou is de TT van Twente ontstaan, en is de basis gelegd voor het 'TopoTukker'-team door de creatieve manier van fabricage die begon met het schrapen aan bismut-telluride kristallen door middel van een scalpeermesje, maar vervolgens via de 'scotch-tape method' heeft geleid tot uiterst gladde en dunne schilfers. Marieke, jij bent hier verder op doorgegaan en dat heeft tot mooie resultaten geleid. Door je lef en vermogen om zowel de experimentele als theoretische kant verder op te gaan ben ik overtuigd dat dit tot meer mooie resultaten zal leiden tijdens je promotieonderzoek.

Kamergenoten Kees, Aleksandar, Marcel, Bernard, Marieke en Denise wil ik bedanken voor de leuke tijd en alle mooie discussies, al dan niet wetenschappelijk. Kees en Aleksandar, ik kan me geen moment herinneren dat het niet gezellig was op onze kamer. Marieke en Denise, ik ben benieuwd of jullie ook zonder mijn hulp de plantjes in leven kunnen houden. Joost, bedankt voor de mooie tijd, zelfs de BHV-cursus werd met jou nog leuk. Ook denk ik aan de 'heldhaftige' momenten tijdens de beklimming van de Zugspitze. Jaap, Jeroen, Johannes, Martin, Reinder, Joost, Peter, Sander Wenderich, Francesco, Obaidul en alle andere promovendi en postdocs van voorheen LT en later ICE wil ik graag bedanken.

Graag wil ik iedereen van het zaalvoetbalteam, waaronder Maarten, Hans Boschker, Ruud, Mark, Peter en Brian, hartelijk bedanken voor de nodige ontspanning. Daarnaast wil ik ook het hele voetbalteam van PW3 graag bedanken.

Verder wil ik al mijn oud-huisgenoten bedanken voor de mooie tijd, in het bijzonder Almer en Desi. Ik heb niets dan goede herinneringen en ik ben er trots op dat jullie mijn paranimfen willen zijn.

Mijn familie wil ik hartelijk danken voor alle steun en ontspanning die zij mij voor en tijdens mijn promotieonderzoek hebben geboden. Arno, Paul en Hiske, Pa en Ma, heel erg bedankt daarvoor. Ook wil ik mijn schoonfamilie hartelijk danken, Herzlichen Dank en sjoekran gazielan.

Als laatste wil ik Sara bedanken. Ik ben er trots op dit jaar te mogen promoveren, maar het mooiste was dat jij 'Ja' zei. SaMen gaan we een heel nieuw avontuur aan in Sydney en ik kijk uit naar al het moois dat wij samen gaan beleven.

Enschede, Augustus 2012

Publications

K. Chen, M. Veldhorst, C.H. Lee, D.R. Lamborn, R. DeFrain, J.M. Redwing, Q. Li, and X.X.Xi, Properties of MgB_2 films grown at various temperatures by hybrid physical-chemical vapour deposition, Superconductor Science and Technology **21** 095015 (2008).

M. van Zalk, M. Veldhorst, A. Brinkman, J. Aarts, and H. Hilgenkamp, In search for the superconducting spin-switch: magnetization induced resistance switching effects in LaSrMnO/YBCO bi- and trilayers. Physical Review B **79**, 134509 (2009).

M. Veldhorst and A. Brinkman, Nonlocal Cooper pair splitting in a pSn junction, Physical Review Letters **105**, 107002 (2010).

M.S. Anwar, M. Veldhorst, A. Brinkman, and J. Aarts, Long range supercurrents in ferromagnetic CrO_2 using a multilayer contact structure, Applied Physics Letters **100**, 052602 (2012).

M. Veldhorst, M. Snelder, M. Hoek, T. Gang, X.L. Wang, V.K. Guduru, U. Zeitler, W.G. van der Wiel, A.A. Golubov, H. Hilgenkamp, and A. Brinkman, Josephson supercurrent through a topological insulator surface state, Nature Materials **11**, 417-421 (2012).

M. Veldhorst, C.G. Molenaar, X.L. Wang, H. Hilgenkamp, A. Brinkman, Experimental realization of SQUIDs with topological insulator junctions, Applied Physics Letters **100**, 072602 (2012).

M. Veldhorst, C.G. Molenaar, C.J.M. Verwijs, H. Hilgenkamp, and A. Brinkman, Optimizing the Majorana character of SQUIDs with topologically non-trivial barriers, Physical Review B **86**, 024509 (2012).

M. Veldhorst, M. Hoek, M. Snelder, H. Hilgenkamp, A.A. Golubov, and A. Brinkman, Nonlocal spin entangled Andreev reflection, fractional charge and Majorana fermions in topological bilayer exciton junctions, submitted for publication.

Stellingen

behorende bij het proefschrift

Superconducting and Topological Hybrids,
Reducing Degrees of Freedom towards the Limit

Menno Veldhorst

1. Door het dubbelzinnige gebruik van het woord gaten lijkt een perpetuum mobile realiseerbaar in een halfgeleider *pn*-junctie.

2. Energiefiltering is een krachtige methode om gekruiste Andreev reflectie te optimaliseren.
(hoofdstuk 3)

3. Ook supergeleidende ringen met standaard magnetische flux kwantisatie kunnen verdubbelde stroom-fase relaties van individuele juncties aan het licht brengen.
(hoofdstuk 6)

4. Het is beter voor zowel de lezer als de schrijver wanneer afstudeerverslagen gereduceerd worden tot 10% van het huidige aantal pagina's.

5. In educatieve zin is het positief als men met de kennis van nu anders zou hebben gehandeld.

6. Op het gevoel af gaan is belangrijk in de exacte wetenschap; ook in die gevallen waar het de verkeerde kant op blijkt te wijzen.

7. In een succesvolle experimentele wetenschappelijke carrière wordt men veelal opgeleid tot de ideale onderzoeker die te duur is om onderzoek te doen.

8. Men zou het met spraakmakende stellingen oneens moeten zijn.

Propositions

accompanying the thesis

Superconducting and Topological Hybrids,
Reducing Degrees of Freedom towards the Limit

Menno Veldhorst

1. Perpetual motion seems possible in semiconductor *pn*-junctions by the ambiguous use of the word holes.

2. Energy filtering is a powerful method to optimize crossed Andreev reflection.
(chapter 3)

3. Even superconducting rings with standard fluxoid quantization can exhibit signatures of junctions with doubled current-phase relationships.
(chapter 6)

4. It is beneficial for both the reader and the writer when graduate theses are reduced to 10% of the current amount of pages.

5. From an educational point of view it is positive when one would have acted differently with today's knowledge.

6. Using one's intuition is important in exact sciences; also when it turns out to point in the wrong direction.

7. In a successful experimental scientific career one is often educated towards the ideal researcher who is too expensive to perform research.

8. One should disagree with notable propositions.